Nucleon axial and pseudoscalar isovector form factors from lattice QCD

Dissertation zur Erlangung des Doktorgrades der Naturwissenschaften (Dr. rer. nat.) der Fakultät für Physik der Universität Regensburg

vorgelegt von

Thomas Wurm

aus

Regensburg

im Jahr 2020

Promotionsgesuch eingereicht am: 25.11.2020
Die Arbeit wurde angeleitet von: Prof. Dr. Andreas Schäfer

Abstract

The axial structure of the nucleon, in particular the iso-vector axial and (induced) pseudoscalar form factors, can be analyzed from first principles using Monte Carlo techniques in lattice QCD. Effective field theory predicts that pseudoscalar form factors are dominated by a pion pole, which originates from an exchange of a virtual pion. While experiments show agreement with this expectation, previous lattice results have violated it. We show that this discrepency can be traced back to excited state contaminations in the three-point correlation function.

To this end we use effective field theory to gain insight into the structure of nucleon pion excited state contributions, which enables us to disentangle the ground state contribution reliably. The extracted form factors then satisfy the pion pole dominance assumption as well as the constraints due to the partial conservation of the axial current up to expected discretization effects. Using a large landscape of ensembles, mostly generated within the CLS-effort, we examine the parametrization dependance and take all relevant limits. We find good agreement both with experiment and with predictions from chiral perturbation theory.

Contents

1. Introduction

The standard model is the successful theory of elementary particle physics and describes three of the four fundamental interactions, namely the electromagnetic, weak, and strong interactions. Among its successes are the predictions of the $W^{\pm}$ and Z bosons and the discovery of the Higgs at the Large Hadron Collider at Cern [1]. The standard model, however, fails to include the fourth fundamental interaction, i.e., gravity, and is therefore sometimes considered incomplete. Additionally dark matter and dark energy, which account for $\sim 95\%$ of the mass of the universe [2], are also not included in the standard model.

In order to find beyond the standard model physics we first need a detailed understanding of current physics from first principle, in particular, the strong interaction part of the standard model, which is called Quantum Chromodynamics or QCD. While perturbative methods work well, e.g., for Quantum Electrodynamics, they are rather problematic for QCD, due to the fact that the strong coupling g is of $\mathcal{O}(1)$ and expansions in orders of g are non- or only slowly convergent. Therefore we are in need of a non-perturbative method and, in this thesis, we chose lattice QCD.

In lattice QCD one regularizes the QCD path integral using Euclidean space-time lattices, which remove both infrared and ultraviolet divergences. Observables can then be estimated through Monte Carlo simulations of the regularized path integral. However, in lattice QCD, one encounters a variety of systematics:

- discretization effects, due to the finite lattice spacing a, require a controlled continuum limit, i.e., $a \to 0$.
- finite volume effects, for example L^3 for the spatial volume, where L is the extent in one spatial dimension, require the infinite volume limit, i.e., $L \to \infty$.
- unphysical quark masses, which are implicitly set in the input parameters, usually need to be extrapolated to the point where the pseudoscalar meson masses have their physical values.

Additionally, correlation functions that are calculated in lattice QCD suffer from excited state contaminations, requiring a careful treatment and analysis.

Numerous studies of the nucleon have been carried out in lattice QCD, see e.g., refs. [3–37], albeit the treatment of the aforementioned systematics still remains challenging. One example for this is the axial coupling g_A, which can be measured with high precision from neutron β decay (e.g., $n \to p\bar{\nu}_e e^-$), see refs. [38–41]. For a long time g_A served as a benchmark test for lattice QCD since earlier lattice determinations tended to underestimate it by ~10%, see for example [10, 14].

As previously published in ref. [42], at finite momentum transfer Q^2, the axial form factor $G_A(Q^2)$ (where $G_A(0) \equiv g_A$) and the induced pseudoscalar form factor $G_P(Q^2)$ are less precisely known. They enter the description of exclusive pion electroproduction [43–46] (e.g., $e^- p \to \pi^- p \nu$), (quasi-)elastic neutrino-nucleon scattering [47–50], radiative muon capture [51–53], and ordinary muon capture [54–57]. Via weak muon capture in muonic hydrogen a combination of the Dirac, Pauli, axial, and induced pseudoscalar form factors can be measured, constraining the latter at the muon capture point [53, 56–59]. The direct determination of the induced pseudoscalar coupling in refs. [56, 57] shows that, at small momentum transfer, the induced pseudoscalar form factor is indeed well approximated by a pion pole dominance (PPD) ansatz. Additionally, chiral perturbation theory (ChPT) can yield valuable low energy theorems [46, 60–63] (motivating, e.g., the above mentioned PPD ansatz).

The goal of this thesis is to extract axial and (induced-) pseudoscalar isovector currents including a treatment of the systematics mentioned above. To this end, the thesis is structured as follows:

In chapter 2 we describe some of the methods that are used when simulating Quantum Chromodynamics (QCD) on the lattice. First we introduce the continuum action and decompose it into a fermionic and a gluonic part. We then define the path integral, perform the Wick rotation to imaginary time, and choose Euclidean space-time lattices as regularizations. Afterwards, we take a more detailed look at some fermionic and gluonic lattice actions, including the actions applied within the CLS effort. We briefly outline the Monte Carlo simulations and conclude the chapter with a discussion of open boundary conditions, which circumvent critical slowing down at fine lattice spacings.

In chapter 3 we detail how the analysis of the ensembles is performed. We start with outlining the scale setting methods, before we discuss the propagators and their smearing techniques. Then we define our operators, the two- and three-point correlation functions, as well as the employed ratio. We conclude the chapter with remarks on the renormalization.

Chapter 4 is dedicated to the effective field theory calculations which we use to isolate most of the excited states contaminations. To this end we discuss the contributing diagrams and define the employed Feynman rules. After the evaluations of the diagrams we conclude the chapter with the final results for the spectral decompositions of two- and three-point functions.

In chapter 5 we discuss the fitting analysis which was performed on a large set of CLS ensembles. We compare the results with predictions from effective field theory, reinvestigate subtracted currents [34], and check a special case for finite final momentum. We conclude the chapter with comments on the obtained excited state energies.

Chapter 6 focuses on the form factors and their extrapolations to the physical limit,

i.e., zero lattice spacing, infinite volume, and physical masses. We define the ratios for the violations of the the pion pole dominance (PPD) assumption and the partial conservation axial current (PCAC). In order to perform the extrapolation we calculate the constraints, which follow from PCAC, for both the dipole parametrization and the z-expansion. We list the final extrapolation formulas and directly compare our findings to other lattice determinations, as well as results obtained from both experiment and baryon chiral perturbation theory.

We summarize our work and give an outlook in chapter 7.

Note that chapters 4, 5, and 6, appendices B and C, and sections 3.9 and 3.10 as well as parts of chapters 1 and 7 have been previously published in [42].

2. QCD on the lattice

This chapter loosely follows ref. [64].

2.1. Continuum theory

Quantum chromodynamics (QCD) is the theory of the strong interaction in particle physics. It is a quantum field theory with the underlying $SU(3)$ color gauge group, which is non-Abelian. It describes the interaction of massive spin 1/2 fermions called quarks and massless spin 1 gauge bosons called gluons.

There are six types, usually referred to as flavor f, of quarks called up, down, charm, strange, top, and bottom. They are represented by Dirac-spinor fields $\psi_\alpha^{f,c}(x)$, that depend on the space-time coordinate x, where $\alpha \in \{1,2,3,4\}$ is the spinor index and $c \in \{1,2,3\}$ is the color index. Quarks can only appear in color-neutral bound-states, which is a phenomenon called confinement. In the following we will suppress the color and spinor indices.

The special unitary group $SU(3)$, or more precisely its Lie algebra, has 3^2-1 independent generators t^a ($a \in \{1,2,\ldots,8\}$). The eight corresponding massless gluons are represented by the vector fields $A_\mu^a(x)$. In perturbative QCD one additionally introduces the so-called Faddeev-Popov ghost fields, to account for unphysical degrees of freedom. Since we are only interested in gauge invariant observable we will not discuss gauge fixing here and refer the interested reader to [64].

With the information given above we can now construct the QCD action. For free quarks the action is given by

$$\mathcal{S}_{\text{free}}\Big[\psi,\overline{\psi}\Big] = \int d^4x \sum_f \overline{\psi}^f(x)\Big(i\not{\partial} - m_f\Big)\psi^f(x), \tag{2.1}$$

with the Dirac adjoint $\overline{\psi}^f(x) = \psi^f(x)^\dagger\gamma_0$, the Feynman slash notation $\not{\partial} \equiv \gamma_\mu\partial^\mu$, and the quark masses m_f. Similarly to quantum electrodynamics (QED), this action is not invariant under local gauge transformations, i.e.

$$\psi^f(x) \quad\longrightarrow\quad \psi'^f(x) = \Omega(x)\,\psi^f(x), \tag{2.2a}$$

$$\overline{\psi}^f(x) \quad\longrightarrow\quad \overline{\psi}'^f(x) = \overline{\psi}^f(x)\,\Omega(x)^\dagger, \tag{2.2b}$$

where (in QCD) $\Omega(x)$ is an $SU(3)$-valued function, compared to the scalar $U(1)$ function in QED. Since $\Omega(x)$ are $SU(3)$ matrices they fulfill $\Omega(x)^\dagger = \Omega(x)^{-1}$. Like in QED, gauge invariance is achieved by implementing the covariant derivative

$$D_\mu(x) = \partial_\mu + igA_\mu, \tag{2.3}$$

where $A_\mu = \sum_a t^a A_\mu^a(x)$ and g is the strong coupling constant. Inserting (2.2) into (2.1) and replacing ∂_μ with the r.h.s. of eq. (2.3) yields

$$\partial_\mu + igA_\mu(x) \quad \longrightarrow \quad \partial_\mu + \Omega(x)^\dagger\big(\partial_\mu\Omega(x)\big) + i\Omega(x)^\dagger A'_\mu(x)\Omega(x). \tag{2.4}$$

Thus the gluon field has to transform as

$$A_\mu(x) \quad \longrightarrow \quad A'_\mu(x) = \Omega(x)A_\mu(x)\Omega(x)^\dagger + \frac{i}{g}\big(\partial_\mu\Omega(x)\big)\Omega(x)^\dagger. \tag{2.5}$$

The gluon kinematic term can be calculated (again similar to QED) using the field strength tensor which can be defined using the covariant derivative:

$$F_{\mu\nu}(x) = -i\big[D_\mu(x), D_\nu(x)\big] = \partial_\mu A_\nu(x) - \partial_\nu A_\mu(x) + ig\big[A_\mu(x), A_\nu(x)\big], \tag{2.6}$$

where $[,]$ is the commutator. In contrast to QED, $\big[A_\mu(x), A_\nu(x)\big]$ does not vanish. This results in 3-gluon and 4-gluon vertices (gluon self-interactions), and ultimately color confinement itself.

The final result for the continuum action is therefore

$$\mathcal{S}\big[\psi, \overline{\psi}, A_\mu\big] = \mathcal{S}_\mathrm{F}\big[\psi, \overline{\psi}, A_\mu\big] + \mathcal{S}_\mathrm{G}\big[A_\mu\big] \tag{2.7}$$

with the fermionic and gluonic actions

$$\mathcal{S}_\mathrm{F}\big[\psi, \overline{\psi}, A_\mu\big] = \int d^4x \ \sum_f \ \overline{\psi}^f(x)\left(i\not{D}(x) - m_f\right)\psi^f(x), \tag{2.8a}$$

$$\mathcal{S}_\mathrm{G}\big[A_\mu\big] = \int d^4x \ -\frac{1}{4}\mathrm{Tr}\Big\{F_{\mu\nu}(x)F^{\mu\nu}(x)\Big\}. \tag{2.8b}$$

2.2. Path integral

Using the action defined in the previous section, we can express expectation values of operators and operator products in terms of path integrals. For example, the expectation value of two operators $\mathcal{O}_1$ and $\mathcal{O}_2$ at times t and 0, respectively, can be written as

$$\langle 0|\mathcal{O}_1(t)\mathcal{O}_2(0)|0\rangle = \frac{1}{\mathcal{Z}}\int D[\overline{\psi}, \psi]D[A_\mu] \ \mathcal{O}_1\big[\psi, \overline{\psi}, A_\mu\big]\mathcal{O}_2\big[\psi, \overline{\psi}, A_\mu\big]e^{i\mathcal{S}[\psi, \overline{\psi}, A_\mu]}, \tag{2.9}$$

where on the r.h.s. the operators $\mathcal{O}_1$ and $\mathcal{O}_2$ are expressed in terms of the fields ψ, $\overline{\psi}$ and A_μ. $\mathcal{Z}$ is the partition function, i.e.,

$$\mathcal{Z} = \int D[\overline{\psi}, \psi]D[A_\mu] \ e^{i\mathcal{S}[\psi, \overline{\psi}, A_\mu]}, \tag{2.10}$$

and $D[\overline{\psi}, \psi]$ and $D[A_\mu]$ are integral measures that are products of all fermion and gauge field measures. Inserting a complete set of states, the l.h.s. of (2.9) can also be written in terms of a sum of exponentials. We will come back to this in sections 3.5 and 3.8.

In Minkowski space-time the action enters eq. (2.9) as $i\mathcal{S}$. This, however, is difficult to interpret as a probability when we want to simulate QCD on a lattice. The cure for this problem is to perform a Wick rotation, i.e., rotating to imaginary time

$$t \quad \longrightarrow \quad it. \tag{2.11}$$

For a collection of relevant conventions see for example appendix C in ref. [65]. Effectively this yields

$$i\mathcal{S}\Big[\psi, \overline{\psi}, A_\mu\Big] \quad \longrightarrow \quad -\mathcal{S}_E\Big[\psi, \overline{\psi}, A_\mu\Big] \tag{2.12}$$

in eqs. (2.9) and (2.10), where $\mathcal{S}_E$ is the Euclidean action. We will derive suitable real Euclidean lattice actions in later sections. From this point on we will drop the subscript E and only use Euclidean conventions, with the exception of chapter 4 where for effective field theory calculations Minkowski conventions are employed.

We regularize the r.h.s. of eq. (2.9) employing 4-dimensional space-time lattices

$$\Lambda = \{n \mid n_1, n_2, n_3 \in \{0, 1, \ldots, N_s\}, n_4 \in \{0, 1, \ldots, N_t\}\}, \qquad x = an, \tag{2.13}$$

with the number of spatial points N_s and the number of temporal points N_t. The finite lattice spacing a serves as an infrared cutoff, whereas the finite spatial and temporal extents, $L = aN_s$ and $T = aN_t$, respectively, serve as ultraviolet cutoffs.

2.3. Fermionic action

In this section we will develop discretized versions of the fermionic QCD action starting from eq. (2.1). We introduce the gauge links and name the main problem of the naive fermion action. Then we describe the solution proposed by Wilson, which will lead to the Wilson fermion action.

2.3.1. Gauge links and the naive fermion action

In order to discretize eq. (2.1) we replace the integral with a finite sum over all lattices sites (cf. eq. (2.13)) and the derivative with its symmetric discretized form. This results in

$$\mathcal{S}_{\text{free}}\Big[\psi, \overline{\psi}\Big] = a^4 \sum_{n \in \Lambda} \sum_f \overline{\psi}^f(n) \left(\sum_\mu \gamma_\mu \frac{\psi^f(n + \hat{\mu}) - \psi^f(n - \hat{\mu})}{2a} + m_f \psi^f(n) \right). \tag{2.14}$$

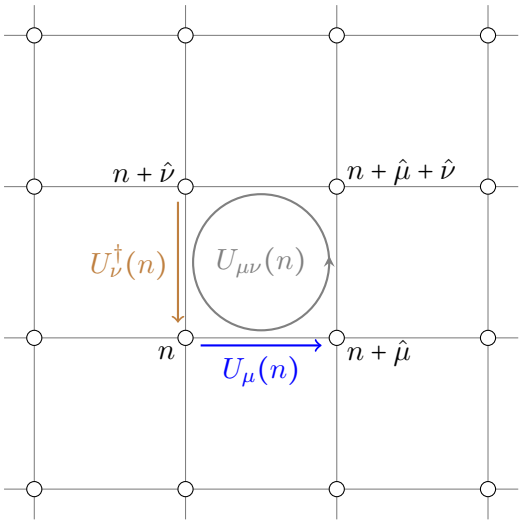

Figure 1: Pictorial representation of the lattice. Gauge links connecting n to $n + \hat{\mu}$ and $n + \hat{\nu}$ to n are depicted in blue and brown, respectively. A plaquette starting at n with the directions μ and ν is displayed in gray.

Like above in the continuum, this action lacks gauge invariance. On the lattice this is fixed by introducing the so-called gauge links $U_\mu(n)$ which connect the point n with $n + \hat{\mu}$ (cf. fig. 1). They are elements of $SU(3)$ and have to transform as

$$U_\mu(n) \quad \longrightarrow \quad U'_\mu(n) = \Omega(n) U_\mu(n) \Omega(n + \hat{\mu})^\dagger. \tag{2.15}$$

For convenience one also defines $U_{-\mu}(n) = U_\mu(n - \hat{\mu})^\dagger$ and $\gamma_{-\mu} = -\gamma_\mu$. Collecting everything, the naive fermion action is given as

$$\mathcal{S}_{\mathrm{F}}^{\mathrm{naive}}\Big[\psi, \overline{\psi}, U\Big] = a^4 \sum_{n \in \Lambda} \sum_f \overline{\psi}^f(n) \left(\sum_{\mu=\pm 1}^{\pm 4} \gamma_\mu \frac{U_\mu(n) \psi^f(n + \hat{\mu})}{2a} + m_f \psi^f(n) \right). \tag{2.16}$$

However, this action suffers from the doubler problem, i.e., the corresponding propagator has additional poles with the same mass m_f at the edges of the first Brillouin zone. This problem is visible, for example, when calculating the free propagator, i.e., $U_\mu = 1$, and performing the Fourier transformation to momentum space. For a more detailed explanation we refer the reader to [64] and only discuss Wilson's solution in the next section.

2.3.2. Wilson fermion action

As a solution to the fermion doubling problem Wilson suggested to add the term[1]

$$-\frac{1}{2}a^3 \sum_{n\in\Lambda}\sum_{f} \overline{\psi}^f(n)\left(\sum_{\mu=\pm1}^{\pm4} U_\mu(n)\psi^f(n+\hat{\mu})\right) + 4a^3 \sum_{n\in\Lambda}\sum_{f} \overline{\psi}^f(n)\psi^f(n), \tag{2.17}$$

which is the discretized and gauge invariant version of

$$\frac{a}{2}\int d^4x \sum_{f} \overline{\psi}^f(x)\,\partial^\mu\partial_\mu\,\psi^f(x), \tag{2.18}$$

i.e., it vanishes in the continuum limit. For the physical pole this term does not contribute while for the doubler poles it affects their masses as

$$am_f + \frac{2L}{a}. \tag{2.19}$$

Hence the doublers decouple from the theory when taking the continuum limit, i.e., $a \to 0$. Additionally one usually defines the hopping parameter

$$\kappa_f = \frac{1}{2am_f + 8} \tag{2.20}$$

and absorbs a factor of $\sqrt{a^3/2\kappa_f}$ into redefinitions of $\overline{\psi}^f(n)$ and $\psi^f(n)$.

Combining eqs. (2.16) and (2.17) we thus obtain the Wilson fermion action

$$\mathcal{S}_{\mathrm{F}}^{\mathrm{Wilson}}\Big[\psi,\overline{\psi},U\Big] = \sum_{n\in\Lambda}\sum_{f} \overline{\psi}^f(n)\left(\psi^f(n) - \kappa_f \sum_{\mu=\pm1}^{\pm4}(1-\gamma_\mu)U_\mu(n)\psi^f(n+\hat{\mu})\right), \tag{2.21}$$

which approaches the continuum action with $\mathcal{O}(a)$ discretization effects.

2.4. Wilson gauge action

Looking at eq. (2.15) one can easily verify that traces of closed loops of link variables are gauge invariant. The shortest nontrivial loop (cf. fig. 1) is called the plaquette $U_{\mu\nu}(n)$ and is defined as

$$U_{\mu\nu}(n) = U_\mu(n)U_\nu(n+\hat{\mu})U_\mu(n+\hat{\nu})^\dagger U_\nu(n)^\dagger. \tag{2.22}$$

[1] In the literature one often finds this term with a coefficient r called Wilson parameter, where setting $r = 1$ ($r = 0$) corresponds to the Wilson (naive) fermion action.

With it the Wilson gauge action can be written as [66]

$$\mathcal{S}_{\mathrm{G}}^{\mathrm{Wilson}}\Big[U\Big] = \frac{\beta}{3}\sum_{n\in\Lambda}\sum_{\mu<\nu}\mathrm{Re}\,\mathrm{Tr}\left(\mathbb{1} - U_{\mu\nu}(n)\right), \tag{2.23}$$

where we have introduced the inverse coupling $\beta = 6/g^2$. Rewriting

$$U_\mu(n) = e^{iaA_\mu(n)} \tag{2.24}$$

and using the Baker-Campbell-Hausdorff formula

$$e^{aA}e^{aB} = e^{aA+aB+\frac{a^2}{2}[A,B]+\mathcal{O}(a^3)} \tag{2.25}$$

one can verify that the Wilson gauge action approaches the continuum action with $\mathcal{O}(a^2)$ discretization effects.

2.5. Symanzik improvement

While the Wilson fermion action has $\mathcal{O}(a)$ discretization effects, the Wilson gauge action has $\mathcal{O}(a^2)$. Within the Symanzik improvement program [67, 68] one can reduce the discretization effects of Wilson fermions to $\mathcal{O}(a^2)$ such that the whole action is $\mathcal{O}(a)$-improved. In a similar fashion one can also improve the Wilson gauge action. To this end one writes an effective action

$$\mathcal{S}_{\text{eff.}} = \int d^4x\Big(\mathcal{L}_{\text{cont.}}(x) + a\sum_i \mathcal{L}_i^{(1)}(x) + a^2\sum_i \mathcal{L}_i^{(2)}(x) + \dots\Big) \tag{2.26}$$

with all possibly contributing terms $\mathcal{L}_i^{(k)}$ of dimension $4+k$. These terms can then be used to counter the discretization effects of their corresponding order.

2.5.1. Wilson clover fermion action

In the case of the Wilson fermion action there are 5 possible terms of dimension 5:

$$\mathcal{L}_1^{(1)}(x) = \overline{\psi}(x)\sigma_{\mu\nu}F_{\mu\nu}(x)\psi(x) \tag{2.27a}$$

$$\mathcal{L}_2^{(1)}(x) = \overline{\psi}(x)\vec{D}_\mu\vec{D}_\mu\psi(x) + \overline{\psi}(x)\overleftarrow{D}_\mu\overleftarrow{D}_\mu\psi(x) \tag{2.27b}$$

$$\mathcal{L}_3^{(1)}(x) = m\,\mathrm{Tr}\left(F_{\mu\nu}F_{\mu\nu}\right) \tag{2.27c}$$

$$\mathcal{L}_4^{(1)}(x) = m\left(\overline{\psi}(x)\vec{\not{D}}\psi(x) + \overline{\psi}(x)\overleftarrow{\not{D}}\psi(x)\right) \tag{2.27d}$$

$$\mathcal{L}_5^{(1)}(x) = m^2\overline{\psi}(x)\psi(x) \tag{2.27e}$$

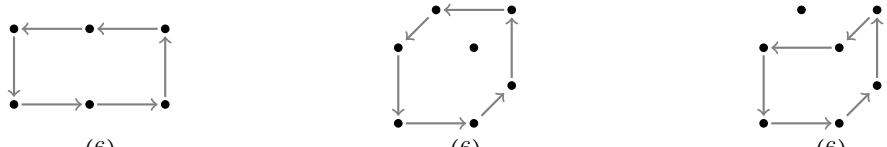

Figure 2: Illustration of all dimensions 6 elementary loops. All types have to be considered for the improvement of the Wilson gauge action.

The equations of motion can be used to eliminate $\mathcal{L}_2^{(1)}(x)$ and $\mathcal{L}_4^{(1)}(x)$, while $\mathcal{L}_3^{(1)}(x)$ and $\mathcal{L}_5^{(1)}(x)$ already appear in the Wilson fermion action. Therefore, the latter can be absorbed into redefinitions of the bare parameters.

Thus the Wilson-clover fermion action is given using the discretized version of $\mathcal{L}_1^{(1)}(x)$:

$$\mathcal{S}_{\mathrm{F}}^{\mathrm{clover}}\Big[\psi,\overline{\psi},U\Big] = \mathcal{S}_{\mathrm{F}}^{\mathrm{Wilson}}\Big[\psi,\overline{\psi},U\Big] + a^2 c_{SW}\sum_{n\in\Lambda}\sum_{f}\ \overline{\psi}^f(n)\sigma_{\mu\nu}F_{\mu\nu}^{\mathrm{lat}}(n)\psi(n), \tag{2.28}$$

with the discretized field strength tensor

$$F_{\mu\nu}^{\mathrm{lat}}(n) = \frac{-i}{8a^2}\Big(Q_{\mu\nu}(n) - Q_{\nu\mu}(n)\Big), \tag{2.29}$$

where

$$Q_{\mu\,\nu}(n) = U_{\mu\,\nu}(n) + U_{\mu\,-\nu}(n) + U_{-\mu\,-\nu}(n) + U_{-\mu\,\nu}(n) \tag{2.30}$$

is the sum over all adjacent plaquettes (hence the name clover). For the tree-level improved Wilson action and $N_f = 3$ the Sheikholeslami-Wohlert [69] coefficient c_{SW} was determined in ref. [70].

We remark that using Wilson-clover fermions reduces discretization effects of the whole action to $\mathcal{O}(a^2)$. However in order to achieve a full $\mathcal{O}(a)$-improvement also local operators have to be corrected. We will discuss in section 3.7 how we improve our currents of interest appropriately.

2.5.2. Tree-level improved Wilson gauge action

For the improvement of the Wilson gauge action we consider the plaquette and all dimension 6 operators. Following [71] we can define the dimension d of a closed of gauge links by taking the continuum limit and expanding as

$$\mathcal{P}^{(d)} \overset{a\to 0}{=} \sum_n a^n \mathcal{P}^{(d,n)}. \tag{2.31}$$

The dimension d is then given as the smallest n for which $\mathcal{P}^{(d,n)} \neq 0$.

For the improved gauge action we make the ansatz:

$$\mathcal{S}_{\mathrm{G}}^{\text{Imp. Wilson}}\Big[U\Big] = c_1^{(4)}\mathcal{S}_{\mathrm{G}}^{\text{Wilson}}\Big[U\Big] + \frac{\beta}{3}\sum_{i=1}^{3} c_i^{(6)} \sum_{\mathcal{C}\in\mathcal{P}_i^{(6)}} \mathrm{ReTr}\big(\mathbb{1} - U(\mathcal{C})\big), \tag{2.32}$$

where $c_k^{(l)}$ are parameters that need to be determined either perturbatively or non-perturbatively, $\mathcal{P}_i^{(6)}$ is the set of all elementary loops of type i and dimension 6 (cf. fig. 2), and $U(\mathcal{C})$ is the oriented product of link variables along the path $\mathcal{C}$. In [71] it was shown that for a tree-level improved action it is sufficient to set

$$c_1^{(4)} = \frac{5}{3} - 24x, \tag{2.33a}$$

$$c_1^{(6)} = -\frac{1}{12} + x, \tag{2.33b}$$

$$c_2^{(6)} = 0, \tag{2.33c}$$

$$c_3^{(6)} = x, \tag{2.33d}$$

where x is a free parameter and $|x| < \frac{1}{16}$ ensures that the action is positive. For convenience, x was set to zero within the CLS effort such that only plaquettes and rectangles contribute to the gauge action. This action is also called the Lüscher-Weisz gauge action and has leading $\mathcal{O}(a^2g^2)$ discretization effects.

2.6. Fermion determinant

All fermion fields have to obey Fermi statistics, i.e., all fermion fields have to anti-commute with each other. For example, with explicit indices, this means

$$\psi_\alpha^{f,c}(n)\psi_{\alpha'}^{f',c'}(n') = -\psi_{\alpha'}^{f',c'}(n')\psi_\alpha^{f,c}(n), \tag{2.34a}$$

$$\overline{\psi}_\alpha^{f,c}(n)\psi_{\alpha'}^{f',c'}(n') = -\psi_{\alpha'}^{f',c'}(n')\overline{\psi}_\alpha^{f,c}(n). \tag{2.34b}$$

Therefore, the fermion fields are introduced as Grassmann numbers.

Using Grassmann numbers one can analytically calculate the Gaussian integral over fermion fields in 2.9, i.e.,

$$\int D[\overline{\psi},\psi]\; e^{\sum_f \overline{\psi}^f D^f \psi^f} = \prod_f \det(D_f) \tag{2.35}$$

where we used matrix representations for the fermion fields ψ, $\overline{\psi}$, and for the Dirac operator D_f. $\det(D_f)$ is called the fermion determinant.

We assume the up and down quarks to be mass degenerate. This is well justified from

nature, e.g., when looking at the similar masses of the proton and the neutron. Thus the corresponding determinants simplify to

$$\det(D_u)\det(D_d) = \det(D_\ell)\det(D_\ell) = \det(D_\ell^\dagger)\det(D_\ell) = \det(D_\ell^\dagger D_\ell). \tag{2.36}$$

This guarantees that the light determinant is always a real positive number. However, due to statistical fluctuations, the light determinant may become very small and unstable to determine. To circumvent this problem, one can employ twisted mass reweighting, which will be discussed in the next section.

For heavier quark flavors mass degeneracy is a very badly fulfilled symmetry. In these cases one implements a rational approximation for the determinant which will be discussed in section 2.6.2.

2.6.1. Twisted mass

Twisted mass reweighting can avoid instabilities in the light quark determinant by shifting the eigenvalue spectrum of the Dirac operator along the positive real axis. The starting point is the exact relation [72]

$$\det\left(D_\ell^\dagger D_\ell\right) = \omega^\ell \det\left(f(D_\ell^\dagger D_\ell)\right), \tag{2.37}$$

where f is a function that yields a modified Dirac operator and ω^ℓ is the associated reweighting factor. We consider two modifications (cf. [73] and table 1 in [72])[2]

$$f_1(D_\ell^\dagger D_\ell) = D_\ell^\dagger D_\ell + \mu^2, \tag{2.38}$$

$$f_2(D_\ell^\dagger D_\ell) = \frac{\left(D_\ell^\dagger D_\ell + \mu^2\right)^2}{D_\ell^\dagger D_\ell + 2\mu^2}, \tag{2.39}$$

where f_1 is the traditional modification for twisted mass reweighting and f_2 was proposed in [72]. During the generation of the CLS ensembles, f_2 was employed. For both f_1 and f_2 the parameter μ serves as an infrared regularization and shifts the spectrum of the Dirac operator along the positive real axes. The corresponding reweighting factors are

[2] In practice one also implements an even-odd preconditioning at this point, which we do not discuss in this thesis. We refer the interested reader to [74] for more information.

then given as

$$\omega_1^\ell = \det\left(\frac{D_\ell^\dagger D_\ell}{D_\ell^\dagger D_\ell + \mu^2}\right), \tag{2.40}$$

$$\omega_2^\ell = \det\left(\frac{D_\ell^\dagger D_\ell}{\left(D_\ell^\dagger D_\ell + \mu^2\right)^2}\left(D_\ell^\dagger D_\ell + 2\mu^2\right)\right). \tag{2.41}$$

The strategy is to use $\det\left(f(D_\ell^\dagger D_\ell)\right)$ in the generation of the ensembles and account for small deviations by calculating the reweighting factors after the simulation. In section 2.7 we will discuss how to include the reweighting in the analysis.

2.6.2. Rational approximation

While the two light flavors are easy to include in the simulation if one assumes mass-degeneracy, the inclusion of heaver quarks is more involved since

$$\det(D_f) = \pm\left|\det(D_f)\right| \tag{2.42}$$

can be positive or negative. The positive square root $\sqrt{D_f^\dagger D_f}$ can be approximated by the rational function [73]

$$\det\left(\sqrt{D_f^\dagger D_f}\right) \approx \det(R_f) \tag{2.43}$$

where

$$R_f = A^{-1}\prod_{i=1}^{N_p}\frac{D_f^\dagger D_f + \bar{\mu}_i^2}{D_f^\dagger D_f + \bar{\nu}_i^2} \tag{2.44}$$

and for a given number of poles N_p the matrix A and the parameters $\bar{\mu}_i$ and $\bar{\nu}_i$ can be determined using Zolotarev's optimal approximation. The corresponding reweighting factor is then defined as

$$\omega_f = \det\left(D_f R_f^{-1}\right). \tag{2.45}$$

Note that, by definition, this factor can switch its sign in the simulation and negative reweighting factors may have to be included. For a detailed discussion we refer the interested reader to ref. [75].

2.7. Monte Carlo simulations

In lattice QCD one can estimate path integrals (e.g. the r.h.s. of eq. 2.9) using Monte Carlo methods. To this end one generates gauge configurations using importance sam-

pling with the probability

$$\frac{1}{Z}\, e^{-\mathcal{S}[\psi,\overline{\psi},A_\mu]} \prod_f \det D_f. \tag{2.46}$$

An observable A is then evaluated on all gauge configurations i and the vacuum expectation value can be estimated via

$$\frac{1}{N_{\text{conf.}}} \sum_{i=0}^{N_{\text{conf.}}-1} A^i, \tag{2.47}$$

where $N_{\text{conf.}}$ is the total number of configurations. For a detailed introduction we refer the reader to ref. [64].

Our CLS ensembles include $N_f = 2 + 1$ flavors of quarks, i.e., two degenerate light quarks and the strange quark. The employed probability then reads

$$\frac{1}{Z}\, e^{-\mathcal{S}[\psi,\overline{\psi},A_\mu]} \det\Big(f_2(D_\ell^\dagger D_\ell)\Big) \det R_s, \tag{2.48}$$

cf. sections 2.6.1 and 2.6.2. Thus we have to take two reweighting factors, ω_l and ω_s, into account when calculating expectation values:

$$\frac{\sum_{i=0}^{N_{\text{conf.}}-1} \omega_l^i \omega_s^i A^i}{\sum_{i=0}^{N_{\text{conf.}}-1} \omega_l^i \omega_s^i}. \tag{2.49}$$

The impact of reweighting on resampling is outlined in appendix A.

2.8. Open boundary conditions

In lattice QCD the traditional choice is to use periodic boundary conditions for the gauge links, since they preserve translational invariance of ensemble averages. However, within the CLS effort, we want to be able to take all relevant limits, i.e., physical masses, infinite volume and continuum limits. In this respect, periodic boundaries are problematic for small lattice spacings a since the Hybrid Monte Carlo algorithm can get trapped in sectors of gauge fields with fixed topological charge [76] which dramatically increases the auto-correlation times of the simulation. Using open boundary conditions avoids this problem by allowing the topological charge to flow in and out through the boundary.

To this end one demands for the field strength tensor $F_{\mu\nu}(x)$

$$F_{4i}(x)\Big|_{x_0=0} = F_{4i}(x)\Big|_{x_0=T} = 0 \tag{2.50}$$

for $i \in \{1, 2, 3\}$. The downside of this approach is that open boundaries introduce lattice artifacts near and at the boundary which can be removed using an appropriate improvement [77]. However these effects are expected to decay exponentially such that one can safely ignore them when calculating observables far away from the boundary.

3. Analysis methods

3.1. Scale setting

When doing lattice calculations the lattice spacing a is only set implicitly in the parameters, requiring a determination after the simulation is done. In earlier lattice simulations the static quark potential and the Sommer parameter r_0, which require fits and/or extrapolations, were used. For the CLS ensembles we set the scale by equating the Wilson flow time t to the reference time t_0, which does not require any fits. For a detailed review we refer the reader to [78] and only briefly sketch the method below.

Following [77] the Wilson flow is given by

$$V_\mu^0(n) = U_\mu(n) \tag{3.1}$$

$$\dot{V}_\mu^t(n) = -g_0^2 \left\{ \partial_{x,\mu} \mathcal{S}_\mathrm{G}\left[V^t\right] \right\} V_\mu^t(n) \tag{3.2}$$

where $U_\mu(n)$ is the gauge link configuration and $\partial_{x,\mu}$ is the natural su(3)-valued differential operator with respect to $V_\mu^t(n)$ (cf. appendix A in [78]). Using the $V_\mu^t(n)$ we can calculate the average action density

$$E(t) = \frac{1}{4N_s^3 N_t} \sum_n \mathrm{Tr}\left\{ G_{\mu\nu}^{V^t}(n) G_{\mu\nu}^{V^t}(n) \right\} \tag{3.3}$$

where $G_{\mu\nu}^{V^t}(n)$ is the discretized field strength tensor (cf. eq. (2.29)) evaluated on the Wilson flow $V_\mu^t(n)$. In case of the open boundary ensembles the positions close to the boundaries are neglected. Finally t_0 is defined through equating

$$t^2 E(t)\Big|_{t=t_0} = 0.3, \tag{3.4}$$

where some interpolation is required. The lattice spacing can then be obtained from

$$\sqrt{8t_0} = 0.413 \text{ fm}. \tag{3.5}$$

In ref. [79] this final step is performed by means of a global fit to several inverse couplings β simultaneously. The resulting lattice spacings a are collected in table 1.

3.2. Propagators

The propagator is one of the most important object that one can calculate directly in lattice QCD. It is the inverse of the Dirac-operator D_f, which can be computed from

β	3.40	3.46	3.55	3.70	3.85
$a\,[\mathrm{fm}]$	0.086	0.076	0.064	0.050	0.039

Table 1: Lattice spacings a, corresponding to the five different inverse couplings β used in this thesis. The lattice spacings have been obtained by determining the Wilson flow time at the $SU(3)$ symmetric point in lattice units, $t_0^\star/a^2$, and setting $t_0^\star$ using the result $\mu_{\mathrm{ref}}^\star = (8t_0^\star)^{-1/2} \approx 478$ MeV of ref. [80].

the gauge configuration using the employed action.[3] The full (also called all-to-all) propagator is a complex $12N_s^3N_t \times 12N_s^3N_t$ matrix and connects all lattice sites, color, and Dirac indices with each other. Its determination is usually not feasible due to the huge amount of memory required and in many cases it is sufficient to only determine a single column (also called point-to-all propagator). There are however workarounds, e.g., the sequential source and stochastic methods which we will discuss in sections 3.8.1 and 3.8.2, respectively.

For the point-to-all determination we can write

$$G^{bc_0}_{\beta\gamma_0}(y,x_0) = \sum_x D_f^{-1}{}^{bc}_{\beta\gamma}(y,x)\; S^c_\gamma(x)^{(c_0,\gamma_0,x_0)}\,, \tag{3.6}$$

where $G^{bc_0}_{\beta\gamma_0}(y,x_0)$ is the propagator that connects the point x_0 with all other points, and $S^c_\gamma(x)^{(c_0,\gamma_0,x_0)}$ is the source vector. In this work we start out with a point source, i.e.,

$$S^c_\gamma(x)^{(c_0,\gamma_0,x_0)} = \delta(x-x_0)\delta_{cc_0}\delta_{\gamma\gamma_0}, \tag{3.7}$$

and smeared it afterwards (cf. section 3.3.2). Applying D_f from the left on both sides of eq. (3.6) leads to the system

$$\sum_y D_f{}^{cb}_{\gamma\beta}(x,y) G^{bc_0}_{\beta\gamma_0}(y,x_0) = S^c_\gamma(x)^{(c_0,\gamma_0,x_0)}\,, \tag{3.8}$$

which we have to solve 12 times (once for each c_0 and γ_0) in order to obtain the point-to-all propagator.

3.3. Smearing techniques

The gauge field within a configuration is a heavily fluctuating function. For our local currents (insertions) we must not interfere with this since it encodes the actual physical information. However in terms of our sources and sinks we can significantly increase the

[3] Thus (for Wilson fermions) the flavor f is determined solely by setting κ, so that flavors with the same mass also share the exact same propagator.

overlap with the ground state of our creation and annihilation operators by applying Wuppertal smearing [81, 82] on APE smoothed [83] gauge fields, which we will describe in the following sections.

3.3.1. APE smoothing

The APE smoothing averages the gauge links with the staples

$$C_{\mu\nu}(U,x) = \sum_{\rho=\pm\nu} U_\rho(x) U_\mu(x+\hat{\rho}) U_{-\rho}(x+\hat{\rho}+\hat{\mu}). \tag{3.9}$$

The starting point is the original gauge field, i.e.,

$$U_\mu^{(0)}(x) = U_\mu(x). \tag{3.10}$$

We restrict ourselves to smoothing the spatial components as

$$U_i^{(n+1)}(x) = P_{SU(3)} \left\{ \alpha U_i^{(n)}(x) + \sum_{j\neq i} C_{ij}\left(U^{(n)}, x\right) \right\} \tag{3.11}$$

with the weight factor α and

$$P_{SU(3)}\{V\} = X \in SU(3) \,\Big|\, \max\left\{ \mathrm{Re}\,\mathrm{Tr}\left(XV^\dagger\right) \right\} \tag{3.12}$$

projects the result back to $SU(3)$ by maximizing the real part of the trace $\mathrm{Tr}\left(XV^\dagger\right)$. To obtain the smoothed gauge field we have set $\alpha = 2.5$ and used 25 iterations of eq. (3.11).

3.3.2. Wuppertal smearing

Wuppertal smearing is an iterative procedure that creates a Gaussian shape out of a δ source (cf. eq. (3.7)) using nearest neighbors. Physically this is motivated since real hadrons are not point-like particles but spatially extended. The smearing prescription reads

$$S^{(n+1)}(x) = \frac{1}{1+6d}\left(S^{(n)}(x) + d \sum_{j=\pm1}^{\pm3} U_j(x) S^{(n)}(x+\hat{j}) \right), \tag{3.13}$$

with the iteration count n and the smearing parameter d, which we have set to 0.25.

For a source as in eq. (3.7) we only need to apply the smearing on a single time slice. However for the sink of the resulting propagator we need to perform the smearing on the whole lattice volume. Additionally, we employed APE smoothed gauge links (cf. section 3.3.1) in eq. (3.13) as this further smooths the Gaussian source, see [84].

We define the smearing radius via

$$r_{\mathrm{sm}}^2 = \sum_{n_1,n_2,n_3=-N_s/2}^{N_s/2-1} \tilde{S}^\dagger(a\vec{n}) a^2 \vec{n}^2 \tilde{S}(a\vec{n}), \tag{3.14}$$

with the normalized smearing function $\tilde{S}(a\vec{n})$ where the position of the delta source is shifted to the origin and

$$\sum_{n_1,n_2,n_3=-N_s/2}^{N_s/2-1} \tilde{S}^\dagger(a\vec{n}) \tilde{S}(a\vec{n}) = 1. \tag{3.15}$$

We collect the smearing radii for our ensembles in table 2 on page 49.

3.4. Operator definitions

In order to calculate the correlation functions we need for extracting nucleon form factors, we take the quark content of the proton and define the nucleon annihilation and creation operators as

$$\mathcal{N}^\alpha(\vec{x},t) = \epsilon_{abc}\, u_a^\alpha(\vec{x},t) \left(u_b(\vec{x},t)^T C\gamma_5 d_c(\vec{x},t) \right), \tag{3.16a}$$

$$\overline{\mathcal{N}}^{\bar{\alpha}}(\vec{x},t) = \epsilon_{\bar{a}\bar{b}\bar{c}} \left(\overline{u}_{\bar{b}}(\vec{x},t) C\gamma_5 \overline{d}_{\bar{c}}(\vec{x},t)^T \right) \overline{u}_{\bar{a}}^{\bar{\alpha}}(\vec{x},t), \tag{3.16b}$$

where we have used the charge conjugation matrix C in the usual quark-diquark structure. The operators in eqs. (3.16) annihilate/create all states with the same quantum numbers as the nucleon and we define the ground state, i.e., the state with the lowest energy, as the nucleon.

In order to calculate the contribution of the ground state to our correlation functions we define the overlap factors with the nucleon ground state as

$$\langle 0|\mathcal{N}^\alpha(\vec{0},0)|N_\sigma^{\vec{p}}\rangle = \sqrt{Z_{\vec{p}}}\, n_{\vec{p},\sigma}^\alpha, \qquad \langle N_\sigma^{\vec{p}}|\overline{\mathcal{N}}^{\bar{\alpha}}(\vec{0},0)|0\rangle = \sqrt{Z_{\vec{p}}}\, \bar{n}_{\vec{p},\sigma}^{\bar{\alpha}}, \tag{3.17}$$

with the nucleon spinors $n_{\vec{p},\sigma}^\alpha$ and $\bar{n}_{\vec{p},\sigma}^{\bar{\alpha}}$ and a nucleon state $|N_\sigma^{\vec{p}}\rangle$ with momentum $\vec{p}$ and spin-projection σ. In general the overlap factors $Z_{\vec{p}}$ will also depend on the smearing. Since we always use the same smearing at the source and the sink we neglect this dependence in our notation.

3.5. Two-point functions

One of the two correlation functions that we need for extracting nucleon form factors is the two-point function where one creates a nucleon at time t_0 and annihilates it at

time t_f. It encodes the mass of the nucleon, which we need for the determination of the form factors, and it serves as a normalization of the three-point function, which we will discuss in section 3.9. Additionally we use the two-point functions to define a generic excited state mass, cf. section 4.4.

With the definitions of section 3.4, the nucleon two-point function reads

$$C^{\vec{p}}_{\text{2pt},P_+}(t_f - t_0) = a^3 \sum_{\vec{x}} e^{-i\vec{p}(\vec{x}-\vec{x}_0)} P_+^{\bar{\alpha}\alpha} \langle \mathcal{N}^\alpha(\vec{x}, t_f) \overline{\mathcal{N}}^{\bar{\alpha}}(\vec{x}_0, t_0) \rangle, \tag{3.18}$$

where we create a nucleon source at space-time position $(\vec{x}_0, t_0)$ and destroy it at $(\vec{x}, t_f)$. We project on positive parity with the unpolarized projector $P_+ = \frac{1}{2}(1 + \gamma_4)$. Using the Fourier transform we can fix the momentum $\vec{p}$ and the resulting two-point function will only depend on the time difference $t = t_f - t_0$. We proceed with the evaluation of the Wick contractions:

$$\begin{aligned}
C^{\vec{p}}_{\text{2pt},P_+}(t) &= a^3 \sum_{\vec{x}} e^{-i\vec{p}(\vec{x}-\vec{x}_0)} P_+^{\bar{\alpha}\alpha} \epsilon_{abc} \epsilon_{\bar{a}\bar{b}\bar{c}} (C\gamma_5)^{\beta\gamma} (C\gamma_5)^{\bar{\beta}\bar{\gamma}} \times \\
&\quad \times \langle u_a^\alpha(\vec{x}, t_f) u_b^\beta(\vec{x}, t_f) d_c^\gamma(\vec{x}, t_f)\ \bar{u}_{\bar{b}}^{\bar{\beta}}(\vec{x}, t_0) \bar{d}_{\bar{c}}^{\bar{\gamma}}(\vec{x}_0, t_0) \bar{u}_{\bar{a}}^{\bar{\alpha}}(\vec{x}_0, t_0) \rangle \\
&= a^3 \sum_{\vec{x}} e^{-i\vec{p}(\vec{x}-\vec{x}_0)} P_+^{\bar{\alpha}\alpha} \epsilon_{abc} \epsilon_{\bar{a}\bar{b}\bar{c}} (C\gamma_5)^{\beta\gamma} (C\gamma_5)^{\bar{\beta}\bar{\gamma}} \times \\
&\quad \times D_{c\bar{c}}^{\gamma\bar{\gamma}}(x, x_0) \left(U_{a\bar{b}}^{\alpha\bar{\beta}}(x, x_0) U_{b\bar{a}}^{\beta\bar{\alpha}}(x, x_0) - U_{a\bar{a}}^{\alpha\bar{\alpha}}(x, x_0) U_{b\bar{b}}^{\beta\bar{\beta}}(x, x_0) \right),
\end{aligned} \tag{3.19}$$

where $U = D_u^{-1}$ and $D = D_d^{-1}$ are the up and down quark propagators, respectively, and we used the short hands $x = (\vec{x}, t_f)$ and $x_0 = (\vec{x}_0, t_0)$. Since we work in the limit of exact isospin symmetry, a single point-to-all propagator (cf. eq. (3.6)) is sufficient to evaluate the equation above. Since we thereby fix the source position x_0, we can repeat this calculation for several spatially and temporally separated sources on the lattice.

Using translational invariance and inserting a full set of states we can rewrite eq. (3.18), which results in

$$\begin{aligned}
C^{\vec{p}}_{\text{2pt},P_+}(t) &= P_+^{\bar{\alpha}\alpha} a^3 \sum_{\vec{x}} e^{-i\vec{p}\vec{x}} \langle \mathcal{N}^\alpha(\vec{x}, t) \overline{\mathcal{N}}^{\bar{\alpha}}(\vec{0}, 0) \rangle \\
&\overset{t \gg 0}{=} P_+^{\bar{\alpha}\alpha} \sum_\sigma \frac{1}{2E_{\vec{p}}} \langle 0 | \mathcal{N}^\alpha(0, 0) e^{-E_{\vec{p}} t} | N_\sigma^{\vec{p}} \rangle \langle N_\sigma^{\vec{p}} | \overline{\mathcal{N}}^{\bar{\alpha}}(\vec{0}, 0) | 0 \rangle \\
&= \frac{Z_{\vec{p}}}{2E_{\vec{p}}} e^{-E_{\vec{p}} t} P_+^{\bar{\alpha}\alpha} \sum_\sigma n_{\vec{p},\sigma}^\alpha \bar{n}_{\vec{p},\sigma}^{\bar{\alpha}} \\
&= Z_{\vec{p}} \frac{E_{\vec{p}} + m}{E_{\vec{p}}} e^{-E_{\vec{p}} t},
\end{aligned} \tag{3.20}$$

where m is the mass of the nucleon and $E_{\vec{p}}$ is the energy of the nucleon with momentum $\vec{p}$. We used the time evolution operator and neglected both backward propagation and excited state contributions. In the final step one can evaluate the sum over the spin-projections σ using the well-known rules for spinors.

Since our lattice action is fully $\mathcal{O}(a)$-improved we implemented the continuum dispersion relation

$$E_{\vec{p}} = \sqrt{m^2 + \vec{p}^2} \tag{3.21}$$

for the ground state energy in eq. (3.20). Since this relation only holds up to $\mathcal{O}(a^2)$ effect, we test its validity in section 5.2 before we use it in the form factor analysis afterwards.

3.6. Insertion currents

The local currents, which we use as the insertion operators in the three-point functions, are defined as

$$\mathcal{P}(\vec{x},t) = \bar{u}_a(\vec{x},t)\gamma_5 u_a(\vec{x},t) - \bar{d}_a(\vec{x},t)\gamma_5 d_a(\vec{x},t), \tag{3.22}$$

$$\mathcal{A}_\mu(\vec{x},t) = \bar{u}_a(\vec{x},t)\gamma_\mu\gamma_5 u_a(\vec{x},t) - \bar{d}_a(\vec{x},t)\gamma_\mu\gamma_5 d_a(\vec{x},t), \tag{3.23}$$

which are the isovector pseudoscalar and isovector axial currents, respectively. In the continuum these currents are related to each other through the axial ward identity or partial conservation of the axial current (PCAC). On the lattice, however, the PCAC relation is only valid up to discretization effects, i.e.,

$$\partial_\mu \mathcal{A}_\mu = 2m_\ell \mathcal{P} + \mathcal{O}(a), \tag{3.24}$$

where m_ℓ is the light quark PCAC mass. We reduce the discretization effects to $\mathcal{O}(a^2)$ using the improved currents in the next section.

We can express matrix elements between two nucleon states in terms of their Lorentz decompositions J, i.e.,

$$\langle N^{\vec{p}'}_{\sigma'} | \mathcal{O}\left(\vec{0},0\right) | N^{\vec{p}}_{\sigma} \rangle = \bar{n}^{\gamma}_{\vec{p}',\sigma'} J[\mathcal{O}]^{\gamma\bar{\gamma}} n^{\bar{\gamma}}_{\vec{p},\sigma}, \tag{3.25}$$

where $q_\mu = p'_\mu - p_\mu$ and $\mathcal{O} \in \{\mathcal{P}, \mathcal{A}_\mu\}$. In Euclidean space the Lorentz decompositions read

$$J[\mathcal{P}] = \gamma_5 G_P(Q^2), \tag{3.26}$$

$$J[\mathcal{A}_\mu] = \gamma_\mu\gamma_5 G_A(Q^2) - \frac{iq_\mu}{2m_N}\gamma_5 G_{\tilde{P}}(Q^2), \tag{3.27}$$

where m is the mass of the nucleon. Using the equations of motion and eq. (3.24) also the form factors can be related to each other as

$$m_\ell G_P(Q^2) = mG_A(Q^2) + \frac{Q^2}{4m} G_{\tilde{P}}(Q^2) + \mathcal{O}(a), \tag{3.28}$$

where we again reduce the discretization effects to $\mathcal{O}(a^2)$ using improved currents.

3.7. $\mathcal{O}(a)$-improvement

As mentioned in section 2.5.1 we still need to improve the local currents $\mathcal{A}_\mu$ and $\mathcal{P}$. Following [64] and similar to the improvement of the action, we start by writing down all possible candidates for the improvement of the axial current:

$$\delta\mathcal{A}^1_\mu(x) = \overline{\psi}(x)\gamma_5\sigma_{\mu\nu}\left(\vec{D}_\nu(x) - \overleftarrow{D}_\nu(x)\right)\psi(x), \tag{3.29a}$$

$$\delta\mathcal{A}^2_\mu(x) = \partial_\mu\left(\overline{\psi}(x)\gamma_5\psi(x)\right), \tag{3.29b}$$

$$\delta\mathcal{A}^3_\mu(x) = m_\ell\overline{\psi}(x)\gamma_\mu\gamma_5\psi(x), \tag{3.29c}$$

where ψ and $\overline{\psi}$ represent some quark field combination. Using the equations of motion we can eliminate $\delta\mathcal{A}^1_\mu$, while $\delta\mathcal{A}^3_\mu$ is just the original operator with a quark mass coefficient and can be absorbed into the multiplicative renormalization, which we will discuss in section 3.10. Thus, using $\delta\mathcal{A}^2_\mu = \partial_\mu\mathcal{P}$, the improved local axial current can be written as

$$\mathcal{A}^{\text{imp}}_\mu(x) = \mathcal{A}_\mu(x) + c_A\partial_\mu\mathcal{P}(x), \tag{3.30}$$

with the symmetrically discretized derivative

$$\partial_\mu f(x) = \frac{f(x + a\hat{\mu}) - f(x - a\hat{\mu})}{2a}. \tag{3.31}$$

The coefficient c_A depends on the lattice spacing a and was non-perturbatively determined in [85].

In the case of the pseudoscalar current $\mathcal{P}$, the only candidate is $m_\ell P$, which is again absorbed into the renormalization, hence

$$\mathcal{P}^{\text{imp}}(x) = \mathcal{P}(x). \tag{3.32}$$

3.8. Three-point functions

In order to extract the form factors we are interested in we have to analyze matrix elements of our local currents $\mathcal{P}$ and $\mathcal{A}_\mu$ between nucleon states. We can obtain these

matrix elements from nucleon three-point functions (or the equivalent ratio, cf. section 3.9) where we create a nucleon at the source at time t_0, insert a current $\mathcal{O}$ at t_i, and finally destroy the nucleon at time t_f.

Thus, we define the three-point function as

$$\begin{aligned} C^{\vec{p}',\vec{p},\mathcal{O}}_{\text{3pt},\Gamma}(t,\tau) &= \Gamma_{\bar{\alpha}\alpha} C^{\vec{p}',\vec{p},\mathcal{O}}_{\text{3pt},\alpha\bar{\alpha}}(t,\tau) \\ &= \Gamma_{\bar{\alpha}\alpha} a^6 \sum_{\vec{x},\vec{y}} e^{-i\vec{p}'(\vec{x}-\vec{x}_0)+i(\vec{p}'-\vec{p})(\vec{y}-\vec{x}_0)} \langle \mathcal{N}^{\alpha}(\vec{x},t_f)\mathcal{O}(\vec{y},t_i)\overline{\mathcal{N}}^{\bar{\alpha}}(\vec{x}_0,t_0)\rangle, \end{aligned} \tag{3.33}$$

with the initial and final momenta, $\vec{p}$ and $\vec{p}'$, respectively, as well as the polarization operator Γ, which we will choose to be $P^i_+ = P_+ i\gamma_i\gamma_5$. The three-point function only depends on the time differences, $t = t_f - t_0$ and $\tau = t_i - t_0$, and for later reference we implicitly defined the three-point function with open spin indices $C^{\vec{p}',\vec{p},\mathcal{O}}_{\text{3pt},\alpha\bar{\alpha}}(t,\tau)$.

The ground state contribution to the three-point function can be computed in a similar fashion as for the two-point function, i.e., by using translational invariance and inserting two complete sets of states:

$$\begin{aligned} C^{\vec{p}',\vec{p},\mathcal{O}}_{\text{3pt},\Gamma}(t,\tau) &= \Gamma_{\bar{\alpha}\alpha} a^6 \sum_{\vec{x},\vec{y}} e^{-i\vec{p}'\vec{x}+i(\vec{p}'-\vec{p})\vec{y}} \langle \mathcal{N}^{\alpha}(\vec{x},t)\mathcal{O}(\vec{y},\tau)\overline{\mathcal{N}}^{\bar{\alpha}}(\vec{0},0)\rangle \\ &= \Gamma_{\bar{\alpha}\alpha} \sum_{\sigma',\sigma} \frac{1}{4E_{\vec{p}'}E_{\vec{p}}} \langle 0|\mathcal{N}^{\alpha}(\vec{0},t)|N^{\vec{p}'}_{\sigma'}\rangle \langle N^{\vec{p}'}_{\sigma'}|\mathcal{O}(\vec{0},\tau)|N^{\vec{p}}_{\sigma}\rangle \langle N^{\vec{p}}_{\sigma}|\overline{\mathcal{N}}^{\bar{\alpha}}(\vec{0},0)|0\rangle + \dots \\ &\overset{t\gg\tau\gg 0}{=} \Gamma_{\bar{\alpha}\alpha} \sum_{\sigma',\sigma} \frac{\sqrt{Z_{\vec{p}'}Z_{\vec{p}}}}{4E_{\vec{p}'}E_{\vec{p}}} e^{-E_{\vec{p}'}(t-\tau)} e^{-E_{\vec{p}}\tau} n^{\alpha}_{\vec{p}',\sigma'} \bar{n}^{\gamma}_{\vec{p}',\sigma'} J[\mathcal{O}]^{\gamma\bar{\gamma}} n^{\bar{\gamma}}_{\vec{p},\sigma} \bar{n}^{\bar{\alpha}}_{\vec{p},\sigma} \\ &= \frac{\sqrt{Z_{\vec{p}'}Z_{\vec{p}}}}{4E_{\vec{p}'}E_{\vec{p}}} e^{-E_{\vec{p}'}(t-\tau)} e^{-E_{\vec{p}}\tau} \operatorname{Tr}\left\{\Gamma(\not{p}'+m)J[\mathcal{O}](\not{p}+m)\right\}. \end{aligned} \tag{3.34}$$

This functional form of the ground state is valid for all possible quark contents of the insertion operator and for all choices of the polarization matrix Γ.

In the following we will treat the up and down quark insertions separately, starting with the current insertion in the down quark line, i.e., $\mathcal{O}_d = \bar{d}\Gamma_{\text{ins}}d$. We rewrite eq. (3.33) as

$$\begin{aligned} C^{\vec{p}',\vec{p},\mathcal{O}_d}_{\text{3pt},\Gamma}(t,\tau) = \Gamma_{\bar{\alpha}\alpha} a^6 \sum_{\vec{x},\vec{y}} & e^{-i\vec{p}'(\vec{x}-\vec{x}_0)+i(\vec{p}'-\vec{p})(\vec{y}-\vec{x}_0)} \epsilon_{abc}\epsilon_{\bar{a}\bar{b}\bar{c}} (C\gamma_5)^{\beta\gamma}(C\gamma_5)^{\bar{\beta}\bar{\gamma}} \Gamma^{\bar{\delta}\delta}_{\text{ins}} \times \\ & \times \langle u^{\alpha}_a(\vec{x},t_f) u^{\beta}_b(\vec{x},t_f) d^{\gamma}_c(\vec{x},t_f)\ \bar{d}^{\bar{\delta}}_d(\vec{y},t_i) d^{\delta}_d(\vec{y},t_i)\ \bar{u}^{\bar{\beta}}_{\bar{b}}(\vec{x}_0,t_0) \bar{d}^{\bar{\gamma}}_{\bar{c}}(\vec{x}_0,t_0) \bar{u}^{\bar{\alpha}}_{\bar{a}}(\vec{x}_0,t_0)\rangle. \end{aligned} \tag{3.35}$$

We depict the connected and disconnected contractions in the first and last row of figure 3, respectively. The resulting connected part of the three-point function reads

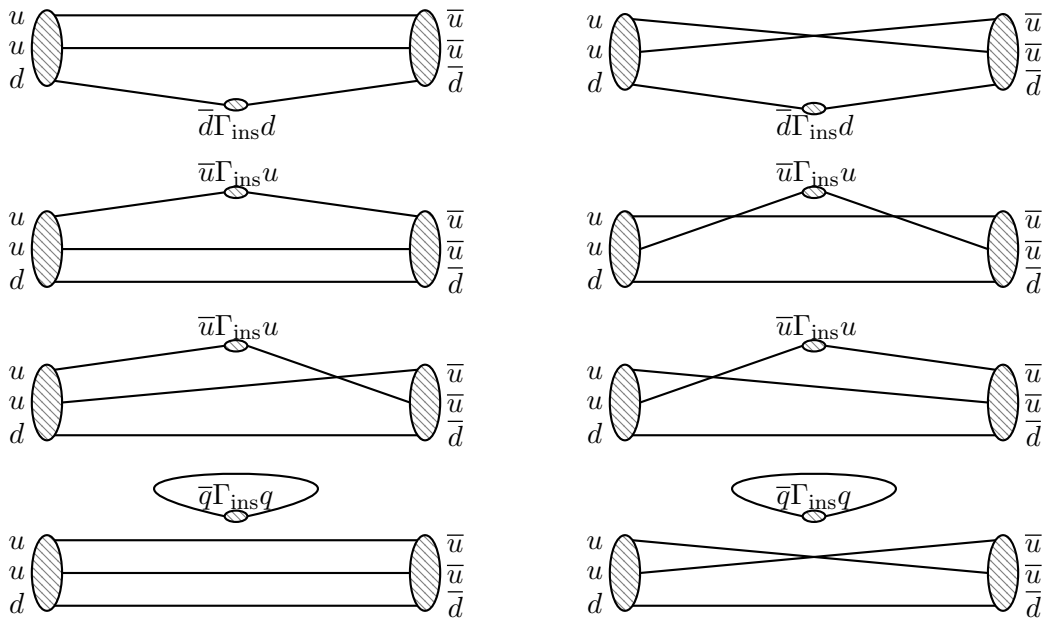

Figure 3: Contractions for the nucleon three-point function. The connected contractions for a u-insertion are depicted in the first row, while the second and third row correspond to a d-insertion. The last row shows the disconnected contractions, which are identical for both u- and d-insertions.

$$C^{\vec{p}',\vec{p},\mathcal{O}_d}_{\text{3pt,conn},\Gamma}(t,\tau) = \Gamma_{\bar{\alpha}\alpha} a^6 \sum_{\vec{x},\vec{y}} e^{-i\vec{p}'(\vec{x}-\vec{x}_0)+i(\vec{p}'-\vec{p})(\vec{y}-\vec{x}_0)} \epsilon_{abc}\epsilon_{\bar{a}\bar{b}\bar{c}} (C\gamma_5)^{\beta\gamma}(C\gamma_5)^{\bar{\beta}\bar{\gamma}} \Gamma^{\bar{\delta}\delta}_{\text{ins}} \times \\ \times D^{\gamma\bar{\delta}}_{cd}(x,y) D^{\delta\bar{\gamma}}_{d\bar{c}}(y,x_0) \left(U^{\alpha\bar{\beta}}_{a\bar{b}}(x,x_0) U^{\beta\bar{\alpha}}_{b\bar{a}}(x,x_0) - U^{\alpha\bar{\alpha}}_{a\bar{a}}(x,x_0) U^{\beta\bar{\beta}}_{b\bar{b}}(x,x_0) \right). \tag{3.36}$$

The disconnected part of the three-point function reads

$$C^{\vec{p}',\vec{p},\mathcal{O}_d}_{\text{3pt,disc},\Gamma}(t,\tau) = -\Gamma_{\bar{\alpha}\alpha} a^6 \sum_{\vec{x},\vec{y}} e^{-i\vec{p}'(\vec{x}-\vec{x}_0)+i(\vec{p}'-\vec{p})(\vec{y}-\vec{x}_0)} \epsilon_{abc}\epsilon_{\bar{a}\bar{b}\bar{c}} (C\gamma_5)^{\beta\gamma}(C\gamma_5)^{\bar{\beta}\bar{\gamma}} \Gamma^{\bar{\delta}\delta}_{\text{ins}} \times \\ \times D^{\delta\bar{\delta}}_{dd}(y,y) D^{\gamma\bar{\gamma}}_{c\bar{c}}(x,x_0) \left(U^{\alpha\bar{\beta}}_{a\bar{b}}(x,x_0) U^{\beta\bar{\alpha}}_{b\bar{a}}(x,x_0) - U^{\alpha\bar{\alpha}}_{a\bar{a}}(x,x_0) U^{\beta\bar{\beta}}_{b\bar{b}}(x,x_0) \right), \tag{3.37}$$

which conveniently factorizes into the two-point function and the momentum projected trace of the disconnected loop:

$$C^{\vec{p}',\vec{p},\mathcal{O}_d}_{\text{3pt,disc},\Gamma}(t,\tau) = -C^{\vec{p}'}_{\text{2pt},\Gamma}(t) \sum_{\vec{y}} e^{i(\vec{p}'-\vec{p})(\vec{y}-\vec{x}_0)} \text{Tr}\Big\{ \Gamma_{\text{ins}} D_{dd}(y,y) \Big\}. \tag{3.38}$$

The derivation is similar for $\mathcal{O}_u = \bar{u}\Gamma_{\text{ins}}u$ but slightly more involved since there are

two u-lines where the current can be inserted. The result for the connected part is (cf. row 2 and 3 of figure 3)

$$C^{\vec{p}',\vec{p},\mathcal{O}_u}_{\text{3pt,conn},\Gamma}(t,\tau) = \Gamma_{\bar{\alpha}\alpha} a^6 \sum_{\vec{x},\vec{y}} e^{-i\vec{p}'(\vec{x}-\vec{x}_0)+i(\vec{p}'-\vec{p})(\vec{y}-\vec{x}_0)} \epsilon_{abc}\epsilon_{\bar{a}\bar{b}\bar{c}} (C\gamma_5)^{\beta\gamma} (C\gamma_5)^{\bar{\beta}\bar{\gamma}} \Gamma^{\bar{\delta}\delta}_{\text{ins}} D^{\gamma\bar{\gamma}}_{c\bar{c}}(x,x_0) \times$$
$$\times \Big(U^{\alpha\bar{\delta}}_{ad}(x,y) U^{\delta\bar{\beta}}_{d\bar{b}}(y,x_0) U^{\beta\bar{\alpha}}_{b\bar{a}}(x,x_0) + \tag{3.39}$$
$$U^{\alpha\bar{\beta}}_{a\bar{b}}(x,x_0) U^{\beta\bar{\delta}}_{bd}(x,y) U^{\delta\bar{\alpha}}_{d\bar{a}}(y,x_0) -$$
$$U^{\alpha\bar{\delta}}_{ad}(x,y) U^{\delta\bar{\alpha}}_{d\bar{a}}(y,x_0) U^{\beta\bar{\beta}}_{b\bar{b}}(x,x_0) -$$
$$U^{\alpha\bar{\alpha}}_{a\bar{a}}(x,x_0) U^{\beta\bar{\delta}}_{bd}(x,y) U^{\delta\bar{\beta}}_{d\bar{b}}(y,x_0) \Big)$$

while the disconnected part yields exactly the same as for $\mathcal{O}_d$, i.e.,

$$C^{\vec{p}',\vec{p},\mathcal{O}_u}_{\text{3pt,disc},\Gamma}(t,\tau) = C^{\vec{p}',\vec{p},\mathcal{O}_d}_{\text{3pt,disc},\Gamma}(t,\tau). \tag{3.40}$$

This is due to the mass degeneracy of the up and down quarks. Hence, when using isovector currents, the disconnected contributions will cancel exactly and we drop them here.

For both quark insertions we require an all-to-all propagator to evaluate eqs. (3.36) and (3.39). Using sequential sources or stochastic estimators circumvents this problem and reduces it to an point-to-all-like solve. We will briefly discuss both methods in the following sections.

3.8.1. Sequential sources

In this approach, the all-to-all propagators in eqs. (3.36) and (3.39) are calculated by sequentially inverting from source to sink and from sink to insertion. As an example, we consider the d-quark insertion and rewrite eq. (3.36) as

$$C^{\vec{p}',\vec{p},\mathcal{O}_d}_{\text{3pt},\Gamma}(t,\tau) = a^3 \sum_{\vec{y}} e^{i(\vec{p}'-\vec{p})(\vec{y}-\vec{x}_0)} \text{Tr}\Big\{ \gamma_5 \Sigma^\dagger_{\bar{c}d}(y,x_0) \gamma_5 \Gamma_{\text{ins}} D_{d\bar{c}}(y,x_0) \Big\}, \tag{3.41}$$

with the sequential propagator Σ which contains all the information at the sink, i.e., sink time t_f, polarization Γ, and final momentum $\vec{p}'$. From comparing with eq. (3.36) we find

$$\big[\gamma_5 \Sigma^\dagger(y,x_0)\gamma_5\big]^{\bar{\gamma}\delta}_{\bar{c}d} = a^3 \sum_{\vec{x}} S^{\bar{\gamma}\gamma}_{\bar{c}c}(x) \Big[\gamma_5 D^\dagger(y,x)\gamma_5\Big]^{\gamma\delta}_{cd}, \tag{3.42}$$

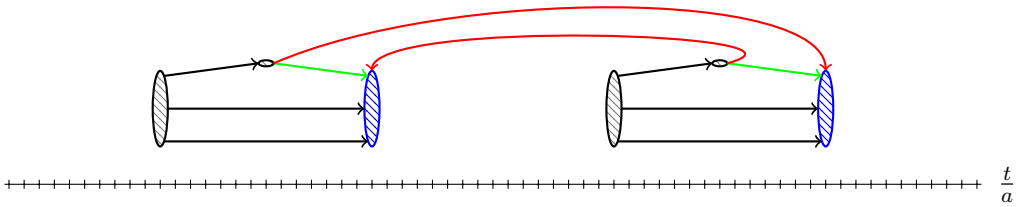

Figure 4: Illustration of the coherent sink method [7] used for some of our ensembles. The black ellipses depict the source position of the point-to-all propagators (black lines). The blue ellipses depict the sequential sources which are combined into one coherent sink. The green and red lines correspond to gauge-invariant and non-gauge-invariant contributions of the coherent sink solve, respectively.

where we have used γ_5-hermiticity and defined the sequential source as[4]

$$\begin{aligned} S^{\bar{\gamma}\gamma}_{\bar{c}c}(x) = \Gamma_{\bar{\alpha}\alpha} e^{-i\vec{p}'(\vec{x}-\vec{x}_0)} \epsilon_{abc}\epsilon_{\bar{a}\bar{b}\bar{c}} (C\gamma_5)^{\beta\gamma} (C\gamma_5)^{\bar{\beta}\bar{\gamma}} \times \\ \times \left(U^{\alpha\bar{\beta}}_{a\bar{b}}(x,x_0) U^{\beta\bar{\alpha}}_{b\bar{a}}(x,x_0) - U^{\alpha\bar{\alpha}}_{a\bar{a}}(x,x_0) U^{\beta\bar{\beta}}_{b\bar{b}}(x,x_0) \right). \end{aligned} \tag{3.43}$$

We can now solve for Σ by applying the dagger on both sides and multiplying the Dirac operator D_d from the left:

$$\sum_{\vec{y}} D_d{}^{\gamma\delta}_{c\bar{c}}(x,y) \Big[\gamma_5 \Sigma_{\bar{c}d}(y,x_0) \Big]^{\delta\bar{\gamma}} = \Big[\gamma_5 S^{\dagger}_{cd}(x) \Big]^{\gamma\bar{\gamma}} \delta_{x_4 t_f}. \tag{3.44}$$

We fix all properties of the sink when we create the sequential source S. Thus we have to carry out one full solve per polarization matrix Γ, final time t_f, final momentum $\vec{p}'$, and also per quark insertion since the result for S would be very different for a u-quark insertion. A common and sensible choice is to set $\vec{p}' = 0$, which was used in the analysis for all of our ensembles with the exception of D201, where we employed the stochastic method which we will describe in the next section.

In ref. [7] the LHPC collaboration suggested to use so-called coherent sinks (illustrated in fig. 4) to reduce the computational cost of nucleon three-point functions. In this approach we start out by calculating the point-to-all propagator for N temporally separated source positions, where the separations should be chosen large enough such that the source-sink distances fit in, i.e., larger than $t+a$. From these propagators we can derive the sequential sources, for example with some fixed source-sink distance, and put all sources into one object. Then we solve on this one object, instead of the N sequential sources separately, and reconstruct the three-point function from this solution. We

[4] For the sake of brevity we omit the implied dependencies on the source position x_0, final momentum $\vec{p}'$, final time t_f, and polarization matrix Γ here.

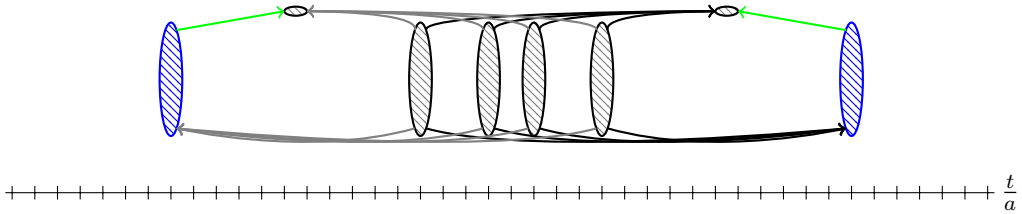

Figure 5: Illustration of the stochastic three-point function code which we employed for D201. The black ellipses depict the sources of the point-to-all propagators. Black and gray lines correspond to forward and backward contributions of the point-to-all propagators, respectively. The blue ellipses depict the stochastically seeded sinks which are solved on in order to obtain the all-to-all propagators depicted in green.

thereby include non-gauge-invariant contributions (depicted in red in figure 4) which will cancel in the ensembles average. This reduces the number of solves for different source positions, however one still needs to perform a solve for each polarization matrix, quark insertion and, source-sink distance.

3.8.2. Stochastic estimators

Another possibility for calculating the all-to-all propagator in eqs. (3.36) and (3.39) is to approximate it stochastically using $\mathbb{Z}_2$ noise vectors. This method is, in terms of the resulting correlators, more flexible than sequential sources since, e.g., for different polarizations or sink momenta no extra inversions are required. However, one introduces an additional uncertainty through the stochastic estimation of the propagator, which is added on top of the statistical error.

In our implementation (cf. figure 5) we seed N_{st} random $\mathbb{Z}_2$ sources at the forward and backward sink timeslices, t_f^{fwd} and t_f^{bwd}, i.e.,[5]

$$S^{(j)}{}_c^{\gamma}(x) = \begin{cases} e^{i\theta}, & \text{if } x_4 \in \left\{t_f^{\mathrm{fwd}}, t_f^{\mathrm{bwd}}\right\}, \\ 0, & \text{otherwise,} \end{cases} \tag{3.45}$$

where $j \in \{1, \ldots, N_{\mathrm{st}}\}$ is the stochastic index and $\theta \in \left\{\frac{\pi}{4}, \frac{3\pi}{4}, \frac{5\pi}{4}, \frac{7\pi}{4}\right\}$ is randomly chosen for each stochastic index, lattice site and color and spin component. Due to the $\mathbb{Z}_2$ noise,

[5] One obtains the all-to-all propagator only if one seeds the $\mathbb{Z}_2$ noise on the whole lattice. Technically we calculate a "time slice-to-all" propagator but in order to avoid confusion we call it all-to-all.

the $S^{(j)}{}_c^{\gamma}(x)$ have the following properties [86]:

$$\frac{1}{N_{\mathrm{st}}} \sum_j S^{(j)}{}_c^{\gamma}(x) = 0 + \mathcal{O}\left(\frac{1}{\sqrt{N}}\right), \tag{3.46}$$

$$\frac{1}{N_{\mathrm{st}}} \sum_j S^{(j)}{}_c^{\gamma}(x) S^{*(j)}{}_d^{\delta}(y) = \begin{cases} \delta_{cd}\delta_{\gamma\delta}\delta(x-y) + \mathcal{O}\left(\frac{1}{\sqrt{N}}\right), & \text{if } x_4 \in \left\{t_f^{\mathrm{fwd}}, t_f^{\mathrm{bwd}}\right\}, \\ 0, & \text{otherwise.} \end{cases} \tag{3.47}$$

For each stochastic index we determine $\Sigma^{(j)}{}_d^{\delta}(y)$ by solving

$$\sum_y D_f{}_{cd}^{\gamma\delta}(x,y) \Sigma^{(j)}{}_d^{\delta}(y) = S^{(j)}{}_c^{\gamma}(x). \tag{3.48}$$

Finally, the all-to-all propagator is obtained via

$$\begin{aligned} \frac{1}{N_{\mathrm{st}}} \sum_j \Sigma^{(j)}{}_d^{\delta}(y) S^{*(j)}{}_c^{\gamma}(x) &= \sum_z D_f^{-1}{}_{db}^{\delta\beta}(y,z) \left[\frac{1}{N_{\mathrm{st}}} \sum_j S^{(j)}{}_b^{\beta}(z) S^{*(j)}{}_c^{\gamma}(x) \right] \\ &= \begin{cases} D_f^{-1}{}_{dc}^{\delta\gamma}(y,x) + \mathcal{O}\left(\frac{1}{\sqrt{N}}\right) & \text{if } x_4 \in \left\{t_f^{\mathrm{fwd}}, t_f^{\mathrm{bwd}}\right\}, \\ 0, & \text{otherwise.} \end{cases} \end{aligned} \tag{3.49}$$

To add even more flexibility to the method we can factorize the three-point functions in spectator and insertion parts, and calculate both parts with open spin indices. This enables us, e.g., to reuse the same insertion part, which contains the stochastic estimation, for several baryons and mesons. Since, in this thesis, we only applied this method for D201 we will not go into more detail here and refer the interested reader to [86, 87].

3.9. Ratios

The nucleon isovector form factors are obtained by a simultaneous fit to two-point functions and to the ratio

$$R_{\Gamma,\mathcal{O}}^{\vec{p}',\vec{p}}(t,\tau) = \frac{C_{3\mathrm{pt},\Gamma}^{\vec{p}',\vec{p},\mathcal{O}}(t,\tau)}{C_{2\mathrm{pt},P_+}^{\vec{p}'}(t)}, \tag{3.50}$$

using the parametrizations given in section 4.4. In the literature also the ratio

$$\frac{C_{3\mathrm{pt},\Gamma}^{\vec{p}',\vec{p},\mathcal{O}}(t,\tau)}{C_{2\mathrm{pt},P_+}^{\vec{p}'}(t)} \sqrt{\frac{C_{2\mathrm{pt},P_+}^{\vec{p}'}(\tau) C_{2\mathrm{pt},P_+}^{\vec{p}'}(t) C_{2\mathrm{pt},P_+}^{\vec{p}}(t-\tau)}{C_{2\mathrm{pt},P_+}^{\vec{p}}(\tau) C_{2\mathrm{pt},P_+}^{\vec{p}}(t) C_{2\mathrm{pt},P_+}^{\vec{p}'}(t-\tau)}} \tag{3.51}$$

is found, which is constructed such that the overlap factors drop out and the ground state contribution is time-independent. This is not the case for the ratio (3.50), where the ground state contribution is $\propto e^{-(E_{\vec{p}}-E_{\vec{p}'})\tau}$. Nevertheless, we find it to be advantageous for various reasons:

1. It allows for a maximal cancellation of correlations, since the interpolating currents at the source and the sink occur at exactly the same spacetime positions with exactly the same phase factors in two- and three-point functions, cf. eqs. (3.18) and (3.33).

2. In contrast to eq. (3.51) it does not introduce additional excited states from two-point functions at small separations τ or $t-\tau$.

3. One avoids a technical problem of eq. (3.51): in the course of the error analysis one can encounter negative values for single bootstrap samples due to statistical fluctuations such that the argument of the square root is negative.

Note that point 1 also explains why fitting the ratio (3.50) is preferable to fitting the three-point function. In principle, using the three-point function is of course equivalent. In practice, however, one would need even better statistics to enable fully correlated, simultaneous fits.

3.10. Renormalization

The local axial and pseudoscalar currents in our calculation have to be renormalized. We use the renormalization factors Z_A from ref. [88] (as recommended in this reference, we use the values $Z^l_{A,\mathrm{sub}}$ from their table 7), which have been determined using a new method based on the chirally rotated Schrödinger functional [89]. In addition, we use the nonperturbative quark mass dependent $\mathcal{O}(a)$-improvement coefficients described in ref. [90] (but with updated values from ref. [91]). The isovector currents are multiplicatively renormalized using

$$\mathcal{A}^{\mathrm{ren}}_\mu = Z_A(\beta)\Big[1+2am^{\mathrm{bare}}_\ell b_A(\beta)+2a(2m^{\mathrm{bare}}_\ell+m^{\mathrm{bare}}_s)\tilde{b}_A(\beta)\Big]\mathcal{A}^{\mathrm{imp}}_\mu, \tag{3.52}$$

$$m^{\mathrm{ren}}_\ell\mathcal{P}^{\mathrm{ren}} = Z_A(\beta)\Big[1+2am^{\mathrm{bare}}_\ell b_A(\beta)+2a(2m^{\mathrm{bare}}_\ell+m^{\mathrm{bare}}_s)\tilde{b}_A(\beta)\Big]m^{\mathrm{imp}}_\ell\mathcal{P}, \tag{3.53}$$

where m^{imp}_ℓ is the PCAC light quark mass obtained from improved currents,

$$m^{\mathrm{imp}}_\ell = \frac{\langle 0|\partial_\mu\mathcal{A}^{\mathrm{imp}}_\mu|\pi\rangle}{2\langle 0|\mathcal{P}|\pi\rangle}. \tag{3.54}$$

The bare quark mass

$$m_q^{\text{bare}} = \frac{1}{2a}\left(\frac{1}{\kappa_q} - \frac{1}{\kappa_{\text{crit}}}\right) \tag{3.55}$$

is calculated using the hopping parameter κ_q (cf. table 2) and its critical value κ_{crit} [79]. We exploit the fact that the product of quark mass and pseudoscalar current renormalizes in exactly the same way as the axialvector current. $\tilde{b}_A$ has been found to be zero within errors and smaller than 0.1 [91]. This corresponds to shifts of at most 4‰, depending on the ensemble, that decrease towards the continuum limit. We neglect this effect, which is small compared to the other sources of errors, and proceed with continuum limit extrapolations that are quadratic in a.

4. EFT-based analysis

Employing a theory where hadrons are the effective degrees of freedom (like baryon chiral perturbation theory) in order to elucidate the excited state structure in correlation functions is appealing, in particular if multi-hadron states with additional pions are the relevant excitations, see refs. [92–96]. In many cases, however, these contributions are relatively small and one can deal with them using standard methods like, e.g., source/sink-smearing and multi-exponential fits that allow for generic excited state contributions. As will be explained in detail in this section, the situation is different in the context of isovector axial and pseudoscalar form factors, where $N\pi$ contributions can actually be a leading term from the EFT point of view due to pion pole dominance (PPD). Especially for small pion masses, this effect outweighs the exponential suppression at the currently available source-sink distances due to the small energy gap.[6] In this situation, multi-exponential fits with generic excited states become very unstable and usually fail to isolate the ground state contribution (see the discussions in refs. [29, 31, 32, 34]).[7]

In refs. [98, 99] nucleon three-point functions with axialvector and pseudoscalar current insertions have been analyzed using ChPT and compelling qualitative evidence has been presented that the violations of the PCAC and PPD relations are indeed caused by $N\pi$ excited states. This is done as follows: first, one calculates the excited state contribution to the form factor using ChPT. The predicted, excited state contaminated form factor is found to agree quite well with recent data from the PACS collaboration [32], cf. refs. [99, 100]. In a second step, one may attempt to correct the error by subtracting the calculated excited state contaminations a posteriori (see, e.g., refs. [98, 101], where such a subtraction has been performed for the induced pseudoscalar form factor). While this method yields convincing qualitative results, there are some open questions and limitations that need to be addressed:

1. In general, the operator smearing can have a different effect on N and $N\pi$ overlap factors, which a leading order ChPT calculation does not allow for. There are heuristic arguments that this effect of the smearing should be negligible as long as the smearing radii r_{sm} are much smaller than the Compton wavelength of the pion, $\lambda_\pi \approx 1.41\,\mathrm{fm}$, cf. refs. [92, 94–96]. This seems to contradict the observation that the operator smearing used in actual simulations has a strong impact on the signal of excited states. In refs. [12, 14] it has been found that smearing radii of roughly $r_{\mathrm{sm}} \sim 0.5\,\mathrm{fm}$ maximize the ground state overlap. In the lattice analysis performed in this work, the optimized smearing radii are on some ensembles even

[6] Note that, due to the exponential deterioration of the signal, one cannot expect the source-sink distances to become dramatically larger in future simulations.

[7] An alternative method has been proposed in ref. [97], which appears to resolve the ground state contribution in this situation. We will comment on this method in some detail in sections 5.3 and 6.1.

larger (up to 0.8 fm, cf. table 2), and it is questionable whether a dependence on the smearing can be completely excluded for such smearing radii.[8]

2. So far, an a posteriori subtraction of the excited states has only been performed in combination with the ratio method on the lattice. It is unclear how one would avoid double counting, if one combines it with a standard excited state analysis, e.g., by using multi-exponential fits.

3. Estimating the systematic error tied to the ChPT based subtraction is challenging.

From a lattice QCD perspective the situation is quite clear concerning point 2. If there is a large $N\pi$ excited state contribution, then it should be taken into account explicitly in the multi-state fits to the correlation functions.[9] In this approach, point 1 can be addressed simultaneously by allowing for a smearing dependence of the $N\pi$ coupling to the interpolating currents. Furthermore, we can avoid systematic uncertainties (point 3) by relaxing ChPT constraints. In the following, we will describe in detail how this can be achieved.

4.1. Diagrams

The first and second rows of figure 6 show the tree-level Feynman diagrams that contribute to the correlation functions. As discussed in ref. [98], these yield the most important contribution to the correlation function. The squares on the right and left depict the smeared source and sink currents, while the one in the middle corresponds to the inserted local quark bilinears (axialvector or pseudoscalar currents in our case). The dashed and solid lines depict pion and nucleon propagators, while the circle stands for a pion-nucleon interaction vertex. The dotted red lines are for illustration only and indicate the identity operators (i.e., the sum over all hadronic states) that are usually inserted between source and current as well as between current and sink, cf. eq. (3.34). This elucidates that the diagram in the first row yields a contribution to the ground state, while the diagrams on the left- and right-hand sides in the second row give rise to a nucleon-pion excitation in the final and initial state, respectively. For the diagram in the middle of the second row, however, the situation is not that simple, since the nucleon-pion interaction is not restricted to a specific time-slice. As a consequence, the

[8] Note that our analysis in section 5 suggests that there is no strong suppression of the $N\pi$ states due to the smearing and that the leading order ChPT approximation for the interpolating currents is actually quite good.

[9] One can also try to circumvent the problem entirely by either suppressing or subtracting the unwanted excited state contributions. In ref. [102] the pion pole contribution is suppressed by analyzing the matrix elements of currents with a Gaussian profile instead of local currents. Ref. [34] presents a method to subtract some of the excited state contributions.

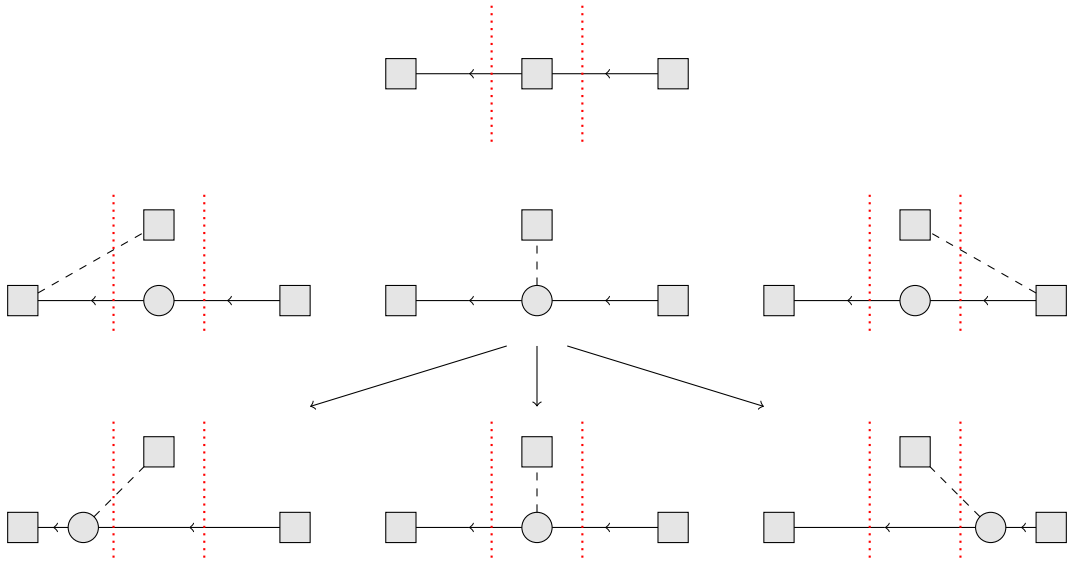

Figure 6: Feynman diagrams showing the most important (tree-level) contributions to the axial and pseudoscalar three-point functions. The squares correspond to explicitly inserted operators: the right and left ones correspond to smeared three-quark baryon interpolating currents at the source (at time 0) and the sink (at time t), respectively, while the ones in the middle depict a pseudoscalar or an axialvector operator insertion (at time τ). The circles correspond to pion-nucleon interaction vertices, while the dashed and solid lines represent pion and nucleon propagators, respectively. The dotted red vertical lines indicate the sums over hadronic states one usually introduces to interpret correlation functions.

diagram contributes to both the ground state and the excited states, as shown in the bottom row of figure 6. This follows from an explicit calculation of the diagrams (see below). We emphasize that there is no one-to-one correspondence between the individual contributions in the spectral decomposition and the diagrams. For example, both the diagram in the first row and the diagram in the middle of the second row contribute to the ground state and, actually, an infinite number of diagrams will contribute to each state if one takes into account higher orders in ChPT (see ref. [98] for a list of one-loop diagrams). Finally, a single diagram can contribute to multiple states in the spectral decomposition, cf. the bottom row of figure 6. We will exploit the fact that the pion pole contribution to the ground state automatically gives rise to an associated excited state.

Before addressing the details, let us note that the following calculation is in large parts already contained in refs. [98, 99], where also one-loop diagrams are taken into account.

Also the presentation in ref. [102] is based on similar considerations (cf. also ref. [103]). However, we will present the result in a more general way (without using a particular spin projection or fixing initial and final state momenta to a predefined configuration) such that it can be used in a variety of simulation setups.

4.2. Feynman rules

The first ingredient we need in order to evaluate the diagrams in figure 6 are the corresponding Feynman rules. Here we follow the conventions of ref. [104], but adapt them to our choices for the currents (see eq. (3.23)) and convert them to position space. We work in two-flavor baryon ChPT here. However, since we only consider the nucleon sector and are only working at tree-level accuracy, a three-flavor calculation would give exactly the same result. Note that in this section all time variables are in Minkowski time and will be rotated to imaginary times only at the very end. The pion and nucleon propagators read

$$S_N(x) = i \int \frac{d^4q}{(2\pi)^4}\, e^{-iqx} \frac{\not{q} + m}{q^2 - m^2 + i\epsilon}, \tag{4.1}$$

$$S_\pi^{ab}(x) = \delta^{ab} S_\pi(x) = i \int \frac{d^4q}{(2\pi)^4}\, e^{-iqx} \frac{\delta^{ab}}{q^2 - m_\pi^2 + i\epsilon}. \tag{4.2}$$

For the vertices of the current insertions we have

$= g_A \gamma^\mu \gamma_5 \sigma^3,$ (4.3)

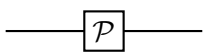

$= 0,$ (4.4)

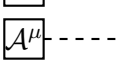

$= -2F_\pi \partial^\mu \delta^{a3},$ (4.5)

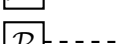

$= -2iF_\pi B \delta^{a3}, \qquad B \equiv \frac{m_\pi^2}{2m_\ell},$ (4.6)

where we only take into account the leading contribution in the chiral counting[10] and all derivatives are understood to act on the pion propagator. Here, F_π and g_A correspond to the pion decay constant and the axial coupling in the chiral limit, respectively, while B is the condensate parameter and σ^a are Pauli matrices.

For the leading $N\pi$ interaction vertex we have

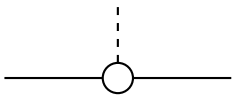
$= -i \frac{g_A}{2F_\pi} \not{\partial} \gamma_5 \sigma^a.$ (4.7)

[10] Note that γ_5 is counted as first order in baryon ChPT, while other elements of the Clifford algebra are counted as zeroth order, see, e.g., ref. [105]. This explains why the NN vertex of the pseudoscalar current vanishes at leading order.

The vertices for local three-quark currents have been derived in ref. [106]. We adapt these to the smeared interpolating currents used here by allowing for momentum- and smearing-dependent couplings. With the nucleon isospinor Ψ_N, where $\Psi_p = (1,0)^T$ and $\Psi_n = (0,1)^T$, the leading order vertices read

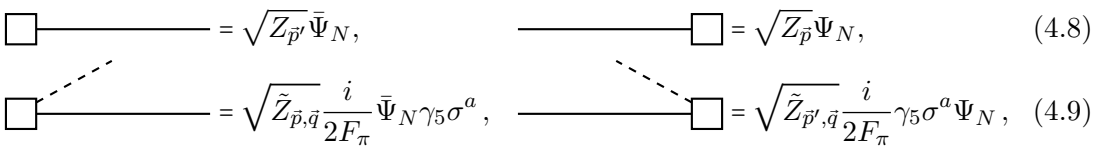

(4.8) (4.9)

where one can actually assume $Z_{\vec{p}} = Z_{\vec{p}}(\vec{p}^{\,2})$ and $Z_{\vec{p},\vec{q}} = Z_{\vec{p},\vec{q}}(\vec{p}^{\,2}, \vec{p}\cdot\vec{q}, \vec{q}^{\,2})$ up to lattice artifacts (obviously, the couplings will also depend on the masses, the smearing method and the smearing radii). We will use $Z = Z_{\vec{p}}$, $Z' = Z_{\vec{p}\,'}$, $\tilde{Z} = \tilde{Z}_{\vec{p}\,',\vec{q}}$, and $\tilde{Z}' = \tilde{Z}_{\vec{p},\vec{q}}$ as shorthand notations. In the following we always consider protons, i.e., $\bar{\Psi}_p\sigma^3\Psi_p = 1$. We will *not* assume

$$\sqrt{\tilde{Z}_{\vec{p},\vec{q}}} = \sqrt{Z_{\vec{p}\,'}} + \text{higher order}\,, \qquad \sqrt{\tilde{Z}_{\vec{p}\,',\vec{q}}} = \sqrt{Z_{\vec{p}}} + \text{higher order}\,, \tag{4.10}$$

which should hold at least approximately for small smearing radii, as discussed above. Instead, we will test the validity of this assumption by comparing it to our data, cf. figure 10 in section 5.2. We complete the setup with the definition of the following energies and four-momenta

$$E = \sqrt{\vec{p}^{\,2} + m^2}\,, \quad E' = \sqrt{\vec{p}^{\,\prime 2} + m^2}\,, \quad E_\pi = \sqrt{(\vec{p}\,' - \vec{p})^2 + m_\pi^2}\,, \tag{4.11}$$

$$p = \begin{pmatrix} E \\ \vec{p} \end{pmatrix}, \quad p' = \begin{pmatrix} E' \\ \vec{p}\,' \end{pmatrix}, \quad q = \begin{pmatrix} E' - E \\ \vec{p}\,' - \vec{p} \end{pmatrix}, \quad r_\pm = \begin{pmatrix} E_\pi \\ \pm(\vec{p}\,' - \vec{p}) \end{pmatrix}. \tag{4.12}$$

4.3. Evaluation of the diagrams

We will now consider one example for each type of diagram in figure 6 with an axialvector current insertion, starting with the purely nucleonic diagram (in the first row of figure 6). Defining the four-vectors $x = (t, \vec{x})$, $y = (\tau, \vec{y})$, we obtain

$$\begin{aligned}
&\sqrt{Z'}\sqrt{Z} \int d^3x\, e^{-i\vec{p}\,'\vec{x}} \int d^3y\, e^{-i(\vec{p}-\vec{p}\,')\vec{y}} S_N(x-y) g_A \gamma^\mu\gamma_5 S_N(y) = \\
&= -\sqrt{Z'}\sqrt{Z} \int \frac{dE_2}{2\pi}\, e^{-iE_2(t-\tau)} \int \frac{dE_1}{2\pi}\, e^{-iE_1\tau} \frac{(\gamma_0 E_2 - \vec{\gamma}\vec{p}\,' + m) g_A \gamma^\mu\gamma_5 (\gamma_0 E_1 - \vec{\gamma}\vec{p} + m)}{(E_2^2 - \vec{p}\,'^2 - m^2 + i\epsilon)(E_1^2 - \vec{p}^{\,2} - m^2 + i\epsilon)} \\
&= \frac{\sqrt{Z'}\sqrt{Z}}{2E'2E} e^{-iE'(t-\tau)} e^{-iE\tau} (\not{p}\,' + m) g_A \gamma^\mu\gamma_5 (\not{p} + m)\,.
\end{aligned} \tag{4.13}$$

In the first step, one integrates over the positions which gives delta distributions in momentum space, which in turn eliminate the integrals over the three-momenta from

the propagators. Then, we close both integration contours in the lower half of the complex plane and use Cauchy's residue theorem twice. Rotating to imaginary times ($t \to -it$ and $\tau \to -i\tau$) one obtains the axial part of eq. (3.34) to zeroth order accuracy in ChPT, exactly as expected.

Next, we consider the left diagram in the second row of figure 6, where the current insertion couples to a pion that directly connects to the sink, while the nucleon propagates directly from source to sink. We find

$$\begin{aligned}
&\sqrt{\tilde{Z}'}\sqrt{Z}\int d^3x\, e^{-i\vec{p}'\vec{x}}\int d^3y\, e^{-i(\vec{p}-\vec{p}')\vec{y}}\left(\frac{i}{2F_\pi}\gamma_5\right)\left(-2F_\pi\frac{\partial}{\partial y_\mu}\right)S_\pi(x-y)S_N(x) = \\
&= -\sqrt{\tilde{Z}'}\sqrt{Z}\int\frac{dE_2}{2\pi}\,e^{-iE_2(t-\tau)}\int\frac{dE_1}{2\pi}e^{-iE_1 t}\,\frac{\binom{E_2}{\vec{q}}^\mu}{E_2^2-\vec{q}^2-m_\pi^2+i\epsilon}\,\frac{\gamma_5(\gamma_0 E_1-\vec{\gamma}\vec{p}+m)}{E_1^2-\vec{p}^2-m^2+i\epsilon} \\
&= +\frac{\sqrt{\tilde{Z}'}\sqrt{Z}}{2E2E_\pi}e^{-iE_\pi(t-\tau)}e^{-iEt}r_+^\mu\gamma_5(\not{p}+m),
\end{aligned} \tag{4.14}$$

where we have introduced the notation $\binom{E_2}{\vec{q}}^\mu$ to list the components of a 4-vector. The pion carries the three-momentum $\vec{q}$, while the nucleon propagates with momentum $\vec{p}$. As in the first diagram, the integrals over the energies can be calculated independently. The diagram yields an $N\pi$ excitation in the final state with the energy $E + E_\pi$. In general this will not be the excited state with the smallest possible energy. For the diagram where the pion propagates from the source to the insertion (cf. the right diagram in the second row of figure 6) one obtains, carrying out an analogous calculation,

$$-\frac{\sqrt{Z'}\sqrt{\tilde{Z}}}{2E'2E_\pi}e^{-iE't}e^{-iE_\pi\tau}r_-^\mu(\not{p}'+m)\gamma_5, \tag{4.15}$$

which yields an $N\pi$ excitation in the initial state.

Finally, the diagram where the nucleon-pion interaction happens dynamically (the middle diagram in the second row of figure 6) gives

$$\begin{aligned}
&\sqrt{Z'}\sqrt{Z}\int d^3x\, e^{-i\vec{p}'\vec{x}}\int d^3y\, e^{-i(\vec{p}-\vec{p}')\vec{y}}\int d^4z \\
&\quad\times S_N(x-z)\left[\left(-i\frac{g_A}{2F_\pi}\gamma_\nu\gamma_5\frac{\partial}{\partial z_\nu}\right)\left(-2F_\pi\frac{\partial}{\partial y_\mu}\right)S_\pi(z-y)\right]S_N(z) = \\
&= g_A\sqrt{Z'}\sqrt{Z}\int\frac{dE_2}{2\pi}\,e^{-iE_2(t-\tau)}\int\frac{dE_1}{2\pi}\,e^{-iE_1\tau} \\
&\quad\times\frac{\binom{E_2-E_1}{\vec{q}}^\mu\binom{E_2-E_1}{\vec{q}}^\nu}{(E_2-E_1)^2-\vec{q}^2-m_\pi^2+i\epsilon}\,\frac{(\gamma_0 E_2-\vec{\gamma}\vec{p}'+m)\gamma_\nu\gamma_5(\gamma_0 E_1-\vec{\gamma}\vec{p}+m)}{(E_2^2-\vec{p}'^2-m^2+i\epsilon)(E_1^2-\vec{p}^2-m^2+i\epsilon)}.
\end{aligned} \tag{4.16}$$

In this case, where the virtual pion has the three-momentum $\vec{q}$ and the energy $E_2 - E_1$,

the remaining integrations over E_1 and E_2 are not independent of each other. We will perform them consecutively starting with E_1. Similarly to the procedure for the other diagrams, both integration contours can be closed in the lower half of the complex plane. There, the integrand has two single poles, which collapse to a double pole if $E_2 = E - E_\pi$. The latter case has to be treated separately. The result after the first integration is

$$g_A \sqrt{Z'} \sqrt{Z} i \int \frac{dE_2}{2\pi} f(E_2), \tag{4.17}$$

where, for $E_2 \neq E - E_\pi$,

$$\begin{aligned} f(E_2) = {} & e^{-iE_2(t-\tau)} e^{-iE\tau} \left(\tfrac{E_2 - E}{\vec{q}} \right)^\mu \left(\tfrac{E_2 - E}{\vec{q}} \right)^\nu \frac{(\gamma_0 E_2 - \vec{\gamma}\vec{p}\,' + m)\gamma_\nu \gamma_5 (\not{p} + m)}{2E((E_2 - E)^2 - E_\pi^2 + i\epsilon)(E_2^2 - E'^2 + i\epsilon)} \\ & + e^{-iE_2 t} e^{-iE_\pi \tau} \left(\tfrac{-E_\pi}{\vec{q}} \right)^\mu \left(\tfrac{-E_\pi}{\vec{q}} \right)^\nu \frac{(\gamma_0 E_2 - \vec{\gamma}\vec{p}\,' + m)\gamma_\nu \gamma_5 (\gamma_0 (E_2 + E_\pi) - \vec{\gamma}\vec{p} + m)}{2E_\pi (E_2^2 - E'^2 + i\epsilon)((E_2 + E_\pi)^2 - E^2 + i\epsilon)} . \end{aligned} \tag{4.18}$$

For $E_2 = E - E_\pi$, one can check that $f(E_2)$ is finite, which is the only relevant information since it means that there is no pole at this point when using the residue theorem for E_2 later on. Thus, one finds that $f(E_2)$ has three poles in the lower half of the complex plane. The first term in eq. (4.18) has two single poles, while the second term in eq. (4.18) has only one single pole. Its second, seeming pole is at $E_2 = E - E_\pi$, where eq. (4.18) is not evaluated. One obtains three contributions that correspond to the diagrams in the bottom row of figure 6:

$$\begin{aligned} & - \frac{g_A \sqrt{Z'} \sqrt{Z}}{2E'2E} e^{-iE'(t-\tau)} e^{-iE\tau} q^\mu q^\nu \frac{(\not{p}\,' + m)\gamma_\nu \gamma_5 (\not{p} + m)}{q^2 - m_\pi^2} \\ & - \frac{g_A \sqrt{Z'} \sqrt{Z}}{2E2E_\pi} e^{-iE_\pi(t-\tau)} e^{-iEt} r_+^\mu r_+^\nu \frac{(\not{p} + \not{r}_+ + m)\gamma_\nu \gamma_5 (\not{p} + m)}{(p + r_+)^2 - m^2} \\ & - \frac{g_A \sqrt{Z'} \sqrt{Z}}{2E'2E_\pi} e^{-iE't} e^{-iE_\pi \tau} r_-^\mu r_-^\nu \frac{(\not{p}\,' + m)\gamma_\nu \gamma_5 (\not{p}\,' + \not{r}_- + m)}{(p' + r_-)^2 - m^2}, \end{aligned} \tag{4.19}$$

where we have written the result in terms of the four-vectors defined in eqs. (4.12). The first term yields a contribution to the ground state. It is responsible for the leading, pole dominant contribution to the induced pseudoscalar form factor. The second and the third term contribute to the same $N\pi$ excitations in the final and initial states as those in eqs. (4.14) and (4.15), respectively.

This concludes our calculation of the tree-level diagrams shown in figure 6 for the axialvector current insertion. For the pseudoscalar current the calculation is analogous and we will not repeat it here. By matching the result obtained for the ground state with the usual form factor decompositions (using eq. (3.34) in combination with eqs. (3.26)

and (3.27) after rotating to Euclidean times) one finds

$$G_A(Q^2) = g_A + \text{higher order}, \tag{4.20}$$

$$G_{\tilde{P}}(Q^2) = g_A \frac{4m^2}{Q^2 + m_\pi^2} + \text{higher order}\,, \tag{4.21}$$

$$G_P(Q^2) = g_A \frac{m}{m_\ell} \frac{m_\pi^2}{Q^2 + m_\pi^2} + \text{higher order}. \tag{4.22}$$

We emphasize that we will not enforce these results for the ground state contribution. In eq. (4.20) this corresponds to augmenting the axial coupling in the chiral limit to the full axial form factor, which is justified at leading order accuracy. In the same spirit, we have already tacitly used the actual nucleon mass in the propagator instead of its chiral limit value, which is also correct to leading order accuracy in ChPT. It is consistent to perform the same replacement $g_A \mapsto G_A$ in the complete calculation. (We will show that this choice is in much better agreement with the data at nonzero Q^2, cf. section 5.2 and, in particular, figure 10.) After doing so, eqs. (4.21) and (4.22) yield the PPD assumptions [107, 108] for the (induced) pseudoscalar form factors, as expected.

It turns out to be convenient to define the ratios

$$a = \frac{\sqrt{\tilde{Z}}}{\sqrt{Z}}, \qquad\qquad a' = \frac{\sqrt{\tilde{Z}'}}{\sqrt{Z'}}, \tag{4.23}$$

where $a = a' = 1$ would correspond to the assumption that the smearing does not affect the overlap of the interpolating currents with the $N\pi$ excited states (compared to the ground state). Note that in general a and a' are functions of the momenta. Putting everything together and rotating to Euclidean time ($t \to -it$ and $\tau \to -i\tau$) we find

$$\begin{aligned} C_{\text{3pt}}^{\vec{p}',\vec{p},\mathcal{A}^\mu} = {} & + \frac{\sqrt{Z'}\sqrt{Z}}{2E'\,2E} e^{-E'(t-\tau)} e^{-E\tau} (\not{p}' + m) \left[G_A \gamma^\mu \gamma_5 + G_{\tilde{P}} \frac{q^\mu}{2m} \gamma_5 \right] (\not{p} + m) \\ & - \frac{\sqrt{Z'}\sqrt{Z}}{2E\,2E_\pi} e^{-(E+E_\pi)(t-\tau)} e^{-E\tau} r_+^\mu \left(b' \gamma_5 (\not{p} + m) + G_A \frac{(\not{p} + m) \not{r}_+ \gamma_5 (\not{p} + m)}{(p + r_+)^2 - m^2} \right) \\ & + \frac{\sqrt{Z'}\sqrt{Z}}{2E'\,2E_\pi} e^{-E'(t-\tau)} e^{-(E'+E_\pi)\tau} r_-^\mu \left(b (\not{p}' + m) \gamma_5 - G_A \frac{(\not{p}' + m) \not{r}_- \gamma_5 (\not{p}' + m)}{(p' + r_-)^2 - m^2} \right) \\ & + \ldots, \end{aligned} \tag{4.24}$$

for the axial current and

$$
\begin{aligned}
C_{\mathrm{3pt}}^{\vec{p}',\vec{p},\mathcal{P}} = &+\frac{\sqrt{Z'}\sqrt{Z}}{2E'\,2E}e^{-E'(t-\tau)}e^{-E\tau}(\not{p}'+m)G_P\gamma_5(\not{p}+m)\\
&-\frac{\sqrt{Z'}\sqrt{Z}}{2E\,2E_\pi}e^{-(E+E_\pi)(t-\tau)}e^{-E\tau}B\left(b'\gamma_5(\not{p}+m)+G_A\frac{(\not{p}+m)\not{r}_+\gamma_5(\not{p}+m)}{(p+r_+)^2-m^2}\right)\\
&-\frac{\sqrt{Z'}\sqrt{Z}}{2E'\,2E_\pi}e^{-E'(t-\tau)}e^{-(E'+E_\pi)\tau}B\left(b(\not{p}'+m)\gamma_5-G_A\frac{(\not{p}'+m)\not{r}_-\gamma_5(\not{p}'+m)}{(p'+r_-)^2-m^2}\right)\\
&+\ldots,
\end{aligned}
\tag{4.25}
$$

for the pseudoscalar current, where

$$
b=-a+G_A\frac{m_\pi^2}{(p'+r_-)^2-m^2},\qquad\qquad b'=-a'+G_A\frac{m_\pi^2}{(p+r_+)^2-m^2},
\tag{4.26}
$$

and the dots represent additional excited state contributions. These results can be used for all momentum configurations and with arbitrary spin projections. After taking the trace with the specific matrices P_+^i that we use here, the result can be further simplified, see below. We emphasize that the leading, pole enhanced $N\pi$ excited state contribution calculated here occurs either in the initial state or in the final state, but not in both simultaneously.

4.4. Spectral decomposition

In this section we will provide the explicit expressions for the correlation functions that are used in our analysis, including our parametrization of additional generic excited states. For the latter we will assume that they occur with the same energies in both, two- and three-point functions. Some state-of-the-art lattice analyses of form factors take into account up to three excited states in the two-point and up to two excited states in the three-point functions, see, e.g., ref. [109]. Whether this is necessary depends on the available statistics and on the applied source/sink smearing. In our simulation a relatively large number of smearing steps was performed, leading to large smearing radii, cf. table 2. In this situation, we find it sufficient to add only one generic excited state to the two- and three-point correlators on top of the pion pole enhanced state that we have calculated in the last section. Including the additional generic excited state term, we obtain for the two-point function

$$
C_{\mathrm{2pt},P_+}^{\vec{p}}(t)=Z_{\vec{p}}\frac{E_{\vec{p}}+m}{E_{\vec{p}}}e^{-E_{\vec{p}}t}\left(1+A_{\vec{p}}e^{-\Delta E_{\vec{p}}t}\right).
\tag{4.27}
$$

In the following we will abbreviate $\Delta E = \Delta E_{\vec{p}}$ and $\Delta E' = \Delta E_{\vec{p}'}$. Note that we do not assume any dispersion relation for the excited state energies, nor do we assume that these are single hadron states. Instead, we treat them as free fit parameters. We define the trace occurring in the ground state contribution to the three-point function as

$$B^{\vec{p}',\vec{p}}_{\Gamma,\mathcal{O}} = \mathrm{Tr}\big\{\Gamma(\not{p}' + m)J[\mathcal{O}](\not{p} + m)\big\}. \tag{4.28}$$

The explicit results can be found in appendix B, together with the remaining traces needed to evaluate eqs. (4.24) and (4.25). For the three-point functions we obtain the parametrization

$$\begin{aligned} C^{\vec{p}',\vec{p},\mathcal{A}^\mu}_{\mathrm{3pt},P^i_+} &= \frac{\sqrt{Z'}\sqrt{Z}}{2E'\,2E} e^{-E'(t-\tau)} e^{-E\tau} \\ &\quad \times \Bigg[B^{\vec{p}',\vec{p}}_{P^i_+,\mathcal{A}^\mu} \Big(1 + B_{10} e^{-\Delta E'(t-\tau)} + B_{01} e^{-\Delta E \tau} + B_{11} e^{-\Delta E'(t-\tau)} e^{-\Delta E \tau} \Big) \\ &\qquad + e^{-\Delta E'_{N\pi}(t-\tau)} \frac{E'}{E_\pi} r^\mu_+ \Big(c' p^i + d' q^i \Big) + e^{-\Delta E_{N\pi}\tau} \frac{E}{E_\pi} r^\mu_- \Big(c\, p'^i + d\, q^i \Big), \Bigg] \end{aligned} \tag{4.29}$$

$$\begin{aligned} C^{\vec{p}',\vec{p},\mathcal{P}}_{\mathrm{3pt},P^i_+} &= \frac{\sqrt{Z'}\sqrt{Z}}{2E'\,2E} e^{-E'(t-\tau)} e^{-E\tau} \\ &\quad \times \Bigg[B^{\vec{p}',\vec{p}}_{P^i_+,\mathcal{P}} \Big(1 + B_{10} e^{-\Delta E'(t-\tau)} + B_{01} e^{-\Delta E \tau} + B_{11} e^{-\Delta E'(t-\tau)} e^{-\Delta E \tau} \Big) \\ &\qquad + e^{-\Delta E'_{N\pi}(t-\tau)} \frac{E'}{E_\pi} \frac{m_\pi^2}{2m_\ell} \Big(c' p^i + d' q^i \Big) - e^{-\Delta E_{N\pi}\tau} \frac{E}{E_\pi} \frac{m_\pi^2}{2m_\ell} \Big(c\, p'^i + d\, q^i \Big) \Bigg], \end{aligned} \tag{4.30}$$

where we have suppressed the dependence of the excited state parameters on the momenta, the spin-projection, and the current insertion: $B_{ij} = B_{ij}(\vec{p}', \vec{p}, \Gamma, \mathcal{O})$. We have defined $\Delta E_{N\pi} = E_\pi + (E' - E)$, $\Delta E'_{N\pi} = E_\pi - (E' - E)$ and

$$c = -2b - 4G_A \frac{m E_\pi + p' \cdot r_-}{(p' + r_-)^2 - m^2}, \qquad c' = -2b' - 4G_A \frac{m E_\pi + p \cdot r_+}{(p + r_+)^2 - m^2}, \tag{4.31}$$

$$d = -G_A \frac{4m(m + E')}{(p' + r_-)^2 - m^2}, \qquad d' = G_A \frac{4m(m + E)}{(p + r_+)^2 - m^2}. \tag{4.32}$$

Equations (4.31) and (4.32) are only valid up to higher order corrections in ChPT. For instance, one could replace G_A by $(Q^2 + m_\pi^2) G_{\tilde{P}}/(4m^2)$ or by $(Q^2 + m_\pi^2) m_\ell G_P/(m m_\pi^2)$ in the $N\pi$ excited state contributions (cf. eqs. (4.20), (4.21) and (4.22)) and the result would still be valid at leading order. From a plain vanilla ChPT power-counting point of view one could even replace G_A by g_A. Therefore, in anticipation of possible higher order corrections, we may relax the assumptions even further by using c, c', d, and d' as free fit parameters, which reduces the ChPT input. This has the additional advantage

that it does not allow the excited state signal to have a direct influence on the result for the ground state form factors. Naturally, one has to pay for the increased number of fit parameters with a slightly larger statistical error for the ground state result – a small price considering that one gets rid of one source of systematic uncertainty. In section 5.2 we will assess the validity of the ChPT predictions by comparing them to the results obtained from the fits. In particular we will be able to check whether the data is consistent with the parameter-free ChPT prediction for d and whether the direct coupling of the smeared three-quark interpolating currents to the $N\pi$ state differs from the leading order ChPT prediction calculated for local currents.

Note the elegance of the parametrization given in eqs. (4.29) and (4.30). Even after relaxing the conditions (4.31) and (4.32), it encodes the relative strength of the $N\pi$ excited state contribution in the different channels. The importance of this knowledge must not be underestimated. For instance, combining eq. (4.28) with eq. (4.29) one can see that any determination of the axial form factor using solely the $\mathcal{A}_1$, $\mathcal{A}_2$, and $\mathcal{A}_3$ channels is not affected by these excited states at all.

Finally, let us note that for the kinematics we use in the numerical analysis, setting the final state momentum to zero, $\vec{p}\,' = 0$, such that $\vec{p} = -\vec{q}$ (this setup is used in many lattice simulations), the parametrization becomes even simpler since one can replace $c'p^i + d'q^i = e'q^i$ (with $e' = d' - c'$) and $cp'^i + dq^i = dq^i$. In this kinematic situation, the $N\pi$ excited state energy corresponds to $E_N(0) + E_\pi(-\vec{q})$ in the initial state and $E_N(\vec{p}) + E_\pi(\vec{q})$ in the final state.

5. Data analysis

5.1. Ensembles

In order to determine the axial and (induced) pseudoscalar form factors using the correlation functions described in sections 3.5 and 3.8, we have analyzed a large set of lattice ensembles generated within the CLS effort [73].[11] The ensembles have been generated using a tree-level Symanzik improved gauge action and $N_f = 2 + 1$ flavors of nonperturbatively order a improved Wilson (clover) fermions, see sections 2.3.2 and 2.5.1. An efficient and stable hybrid Monte Carlo sampling is achieved by applying twisted-mass determinant reweighting [76], which avoids near-zero modes of the Wilson Dirac operator, cf. section 2.6.1. The polynomial approximation of the strange quark determinant was corrected for by reweighting too, employing the method introduced in ref. [75]. We use the nucleon interpolator defined in eq. (3.16), where the individual quarks at the source and the sink are Wuppertal-smeared [81], employing spatially APE-smoothed [83] gauge links.

Some of the CLS ensembles (cf. table 2 for a full list of the ensembles used in this work) have been simulated employing very fine lattices down to $a = 0.039$ fm. For these lattices we avoid large autocorrelation times by using open boundary conditions in the time direction [76, 77]. While employing open boundary conditions is crucial for fine lattice spacings, we use lattices with both open and periodic boundary conditions for the coarser spacings. In total we have five different lattice spacings ranging from $a = 0.039$ fm to $a = 0.086$ fm, see table 1. The spatial and temporal extents are encoded in the letter of the ensemble name, see table 3.

As illustrated in figure 7, the available ensembles have been generated along three different trajectories in the quark mass plane:[12]

a) sym, blue: trajectory with exact flavor symmetry, where the light and strange quark masses are degenerate ($m_\ell = m_s$)

b) trM, green: ensembles created with $2m_\ell + m_s = \text{const.}$, such that $2m_K^2 + m_\pi^2 \approx \text{phys.}$

c) msc, red: ensembles created keeping the renormalized strange quark mass constant [111], so that $2m_K^2 - m_\pi^2 \approx \text{phys.}$

[11] The ensembles rqcd021 and rqcd030 have been generated using the BQCD code [110].

[12] See also ref. [111]. In practice the ensembles do not always lie exactly on top of the green and red trajectories shown in figure 7.

Ens.	b.c.	κ_l	κ_s	m_π	m_K	$m_\pi L$	$r_{\rm sm}$	#conf.	$t/a_{\#\rm meas.}$	traj.
				$\beta = 3.4$						
U103	o	0.13675962	0.13675962	417	417	4.4	0.638	2473	8_1, 10_2, 12_3, 14_4	trM, sym
H101	o	0.13675962	0.13675962	420	420	5.9	0.643	2000	8_2, 10_2, 12_2, 14_2	trM, sym
H102	o	0.136865	0.136549339	352	439	4.9	0.669	1997	8_1, 10_2, 12_3, 14_4	trM
H105	o	0.13697	0.13634079	279	465	3.9	0.735	1996	8_1, 10_2, 12_3, 14_4	trM
N101	o	0.13697	0.13634079	279	463	5.8	0.722	320	8_1, 10_2, 12_3, 14_4	trM
C101	o	0.13703	0.136222041	220	472	4.6	0.772	2343	8_1, 10_2, 12_3, 14_4	trM
D101	o	0.13703	0.136222041	220	473	6.1	0.799	323	8_1, 10_2, 12_3, 14_4	trM
D150	p	0.137088	0.13610755	126	479	3.5	0.844	579	8_1, 10_2, 12_3, 14_4	trM, msc
H107	o	0.13694566590798	0.136203165143476	366	546	5.1	0.673	1564	8_2, 10_2, 12_3, 14_4	msc
H106	o	0.137015570024	0.136148704478	272	516	3.8	0.680	1553	8_2, 10_2, 12_3, 14_4	msc
C102	o	0.13703	0.136222041	222	501	4.6	0.779	1500	8_2, 10_2, 12_3, 14_4	msc
rqcd021	p	0.136813	0.136813	338	338	4.7	0.676	1541	8_2, 10_2, 12_4, 14_4	sym
				$\beta = 3.46$						
B450	p	0.13689	0.13689	418	418	5.2	0.617	1594	9_1, 11_2, 13_3, 16_4	trM, sym
S400	o	0.136984	0.136702387	352	442	4.3	0.665	2872	9_1, 11_2, 13_3, 16_4	trM
N401	o	0.1370616	0.1365480771	285	461	5.3	0.721	1100	9_1, 11_2, 13_3, 16_4	trM
D450	p	0.137126	0.136420428639937	214	477	5.3	0.784	620	9_4, 11_4, 13_4, 16_4	trM
B452	p	0.1370455	0.136378044	350	545	4.3	0.650	1944	9_3, 11_3, 13_3, 16_4	msc
N450	p	0.1370986	0.136352601	285	524	5.3	0.706	1132	9_4, 11_4, 13_4, 16_4	msc
D451	p	0.13714	0.136337761	217	503	5.4	0.784	532	9_4, 11_4, 13_4, 16_4	msc
rqcd030	p	0.1369587	0.1369587	317	317	3.9	0.688	1224	9_4, 11_4, 13_8, 16_8	sym
X450	p	0.136994	0.136994	263	263	4.9	0.739	400	9_2, 11_2, 13_4, 16_4	sym
				$\beta = 3.55$						
N202	o	0.137	0.137	411	411	6.4	0.610	884	11_1, 14_2, 16_2, 19_4	trM, sym
N203	o	0.13708	0.136840284	345	442	5.4	0.660	1543	11_1, 14_2, 16_3, 19_4	trM

Ens.	b.c.	κ_l	κ_s	m_π	m_K	$m_\pi L$	r_{sm}	#conf.	$t/a_{\#\mathrm{meas.}}$	traj.
N200	o	0.13714	0.13672086	284	462	4.4	0.696	1712	11_1, 14_2, 16_3, 19_4	trM
D200	o	0.1372	0.136601748	201	481	4.2	0.786	1999	11_1, 14_2, 16_3, 19_4	trM
E250	p	0.137232867	0.136536633	130	489	4.1	0.829	490	11_4, 14_4, 16_4, 19_4	trM, msc
N204	o	0.137112	0.136575049	351	545	5.5	0.661	1500	11_2, 14_2, 16_3, 19_4	msc
N201	o	0.13715968	0.136561319	285	523	4.5	0.727	1522	11_2, 14_2, 16_3, 19_4	msc
D201	o	0.1372067	0.136546844	199	501	4.1	0.778	1078	11_4, 14_4, 16_4, 19_4	msc
X250	p	0.13705	0.13705	348	348	5.4	0.655	345	11_2, 14_2, 16_4, 19_4	sym
X251	p	0.1371	0.1371	267	267	4.2	0.719	436	11_4, 14_4, 16_8, 19_8	sym
				$\beta = 3.7$						
N300	o	0.137	0.137	422	422	5.1	0.591	760	14_1, 17_2, 21_2, 24_4	trM, sym
N302	o	0.137064	0.1368721791358	346	451	4.2	0.644	1383	14_1, 17_2, 21_3, 24_4	trM
J303	o	0.137123	0.1367546608	257	475	4.2	0.705	634	14_1, 17_2, 21_6, 24_8	trM
N304	o	0.137079325093654	0.136665430105663	351	554	4.3	0.620	1652	14_2, 17_2, 21_3, 24_4	msc
J304	o	0.137123	0.1367546608	260	523	4.2	0.708	1525	14_3, 17_3, 21_3, 24_4	msc
				$\beta = 3.85$						
J500	o	0.136852	0.136852	410	410	5.2	0.579	750	17_1, 22_2, 27_3, 32_4	trM, sym
J501	o	0.1369032	0.136749715	333	445	4.2	0.613	1507	17_1, 22_2, 27_3, 32_4	trM

Table 2: List of the ensembles used in this work with the respective boundary condition in time (periodic (p) or open (o)), labeled by their identifier and sorted by the inverse coupling β. We list the light and strange hopping parameters κ_ℓ and κ_s used in the simulation and the resulting approximate meson masses (given in MeV). We also provide the root mean squared smearing radii r_{sm} for the light quark sources in fm defined in eq. (3.14). #conf. gives the number of configurations analyzed. The column t/a lists the source-sink distances in lattice units that have been analyzed on this lattice. The subscript #meas. specifies how many measurements have been performed for the respective source-sink distance. The last column specifies on which trajectories in the quark mass plane the ensemble lies, cf. figure 7. An in-depth description of the ensemble generation can be found in ref. [73]. Note that ensemble D201 was only used for the test with nonzero final momentum shown in figure 12.

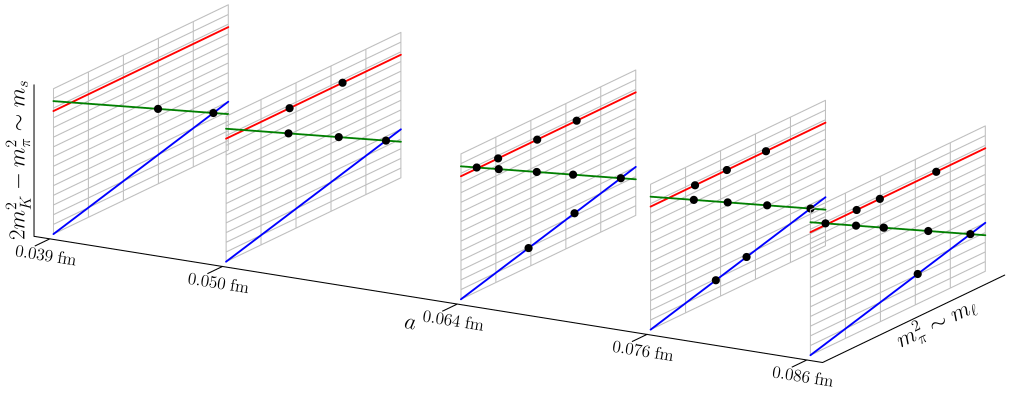

Figure 7: Schematic visualization of the analyzed CLS ensembles in the space spanned by the lattice spacing and the quark masses. On the flavor symmetric plane (blue), where $m_\ell = m_s$, flavor multiplets of hadrons have degenerate masses (e.g., $m_K^2 = m_\pi^2$). The green lines are defined to have physical average quadratic meson mass ($2m_K^2 + m_\pi^2 =$ phys.). This corresponds to an approximately physical mean quark mass ($2m_\ell + m_s \approx$ phys.). The red lines are defined by $2m_K^2 - m_\pi^2 =$ phys. and indicate an almost physical strange quark mass ($m_s \approx$ phys.). Physical masses are reached at the intersections of green and red lines.

Along trajectory a) observables do not depend on the quark mass splitting. Data from these ensembles thus enables a precise determination of the dependence on the average quark mass, and can also be used to obtain results in the three-flavor chiral limit. Trajectory b), where the average quark mass is kept approximately constant, yields complementary information on flavor symmetry breaking. The additional data along trajectory c) provides further insight into the dependence on the light quark mass. The physical point is close to the intersection of the latter two trajectories. Since we cover a large fraction of the relevant quark mass plane, any deviation of an ensemble from its target trajectory can be taken into account.

The ensembles cover a range of volumes with $3.5 \leq m_\pi L \leq 6.4$ allowing us to investigate and control finite volume effects. The majority of the ensembles has $m_\pi L > 4$. Having multiple quark mass trajectories with a wide range of lattice spacings and volumes enables us to simultaneously extrapolate to physical masses, to infinite volume, and to the continuum limit by means of a global fit to 37 ensembles. Our extrapolation strategy is explained in detail in section 6.2.

5.2. Fits to the correlation functions

On each ensemble we have analyzed 4 source-sink separations that have been chosen such that they correspond roughly to the physical distances 0.7 fm, 0.9 fm, 1.0 fm, and 1.2 fm.

	N_s	N_t		N_s	N_t		N_s	N_t
B	32	64	J	64	192	H	32	96
C	48	96	S	32	128	X	48	64
D	64	128	U	24	128	rqcd021	32	32
E	96	192	N	48	128	rqcd030	32	64

Table 3: List of lattice volumes that are used in this work, where N_s and N_t are the number of points in spatial and temporal direction, respectively. The volumes are encoded in the first letter of the ensemble name with the exception of the rqcd ensembles.

The source-sink distance in lattice units and the corresponding number of measurements per configuration are specified in table 2. On some ensembles we have reduced the computational cost by applying the coherent sink technique, cf. section 3.8.1. For the statistical analysis we generate 500 bootstrap samples per ensemble using a bin size of 20 molecular dynamics units to eliminate autocorrelations.

The nucleon energies determined from fits to two-point functions using the spectral decomposition in eq. (4.27) with one generic excited state agree with the continuum dispersion relation, see figure 8. With this justification, we employ the continuum dispersion relation for single nucleon energies in the subsequent analysis.

Results of the simultaneous fits using the ratio defined in eq. (3.50) and the two-point functions are shown in figure 9, where we have selected cases in which the effect due to the pion pole enhanced excited states is large, i.e., ensembles with small pion masses at small (but nonzero) momentum transfer. Note that for our kinematics the parametrization (4.29) and (4.30) only includes two additional fit parameters (d and e') in addition to the usual excited state parametrization. These two parameters describe the $N\pi$ related excited state contributions for the axialvector and pseudoscalar channels simultaneously, for all spin-projections. That this is even possible strongly indicates that the results given in section 4.4 are a very good approximation of the underlying physics.

In order to take into account systematic uncertainties of our excited state analysis, we perform a fit range variation, where the minimal distance between the operators is varied between $2a$ and $4a$ in the ratios, and between $2a$ and $3a$ in the two-point functions. In figures 9 and 11 the full circles (dots) correspond to data points that are always (never) part of the fitted window, while the open symbols indicate data points that are used only in some of the fits. The error bands of the extracted ground state contributions contain both the statistical error and the error related to the choice of the fit range.

In figure 9 the yellow bands correspond to the ground state contributions extracted from the EFT-inspired ansatz for the three-point function (eqs. (4.29) and (4.30)), while

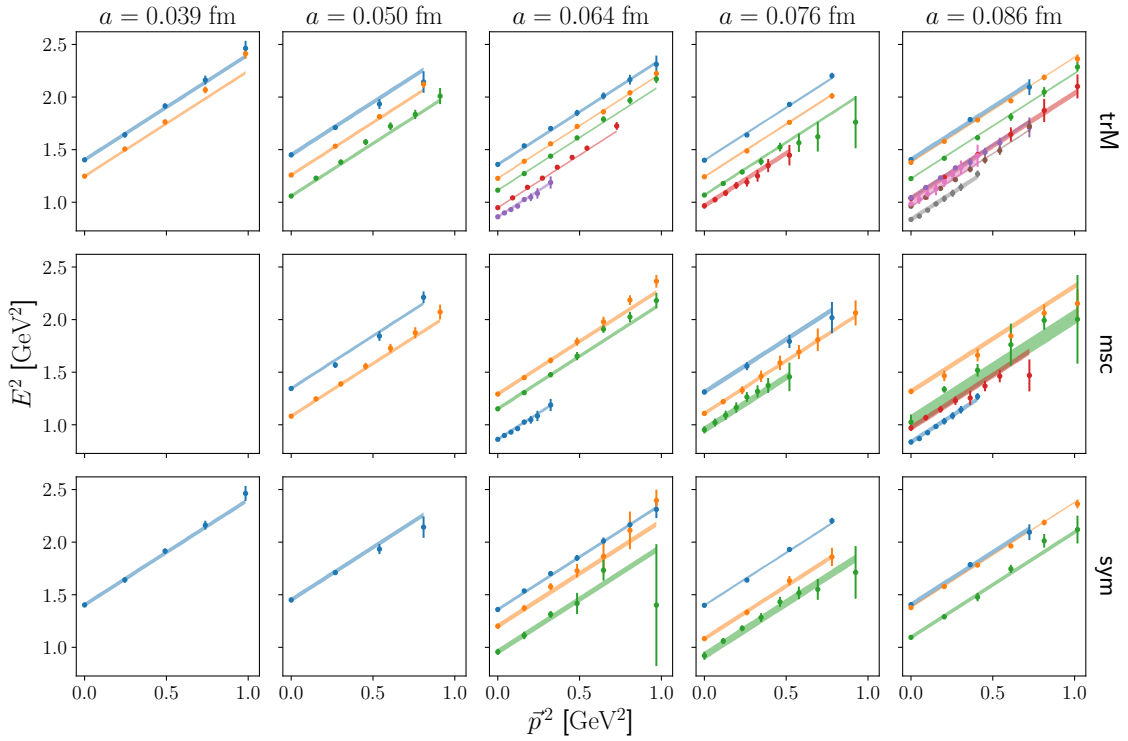

Figure 8: Nucleon dispersion relation for the ensembles listed in table 2. The data points show the squared ground state energies obtained from fits to two-point functions using the ansatz (4.27) and treating the energies as free fit parameters. The lines correspond to $E^2 = m^2 + \vec{p}^2$ using the nucleon mass m determined at zero momentum.

the gray band is the ground state signal obtained from a traditional multistate fit ansatz (also using eqs. (4.29) and (4.30), but without the explicit $N\pi$ contribution, i.e., setting $c = c' = d = d' = 0$). The decomposition of the ground state matrix elements in terms of form factors is determined by eq. (4.28); see appendix B for an explicit evaluation. As one can see, the ground state contribution can be disentangled from the huge signal of the $N\pi$ state (which fails to be resolved using the traditional ansatz with generic excited state contributions). Here, it is particularly advantageous that the coefficients of the $N\pi$ contributions are constrained for various channels and spin projections in our fit, which simplifies the determination of the corresponding fit parameters ($e' = d' - c'$ and d, for our kinematics). To this end, the seemingly linear behavior of $\mathcal{A}_0$ (i.e., row 3 in figure 9, where the spin projection is aligned with the momentum) is actually helpful and it is noteworthy that this data can be described very well by our fit ansatz. The ratio shown in the top panels (which is sensitive to G_A but independent of $G_{\tilde{P}}$) is not affected by

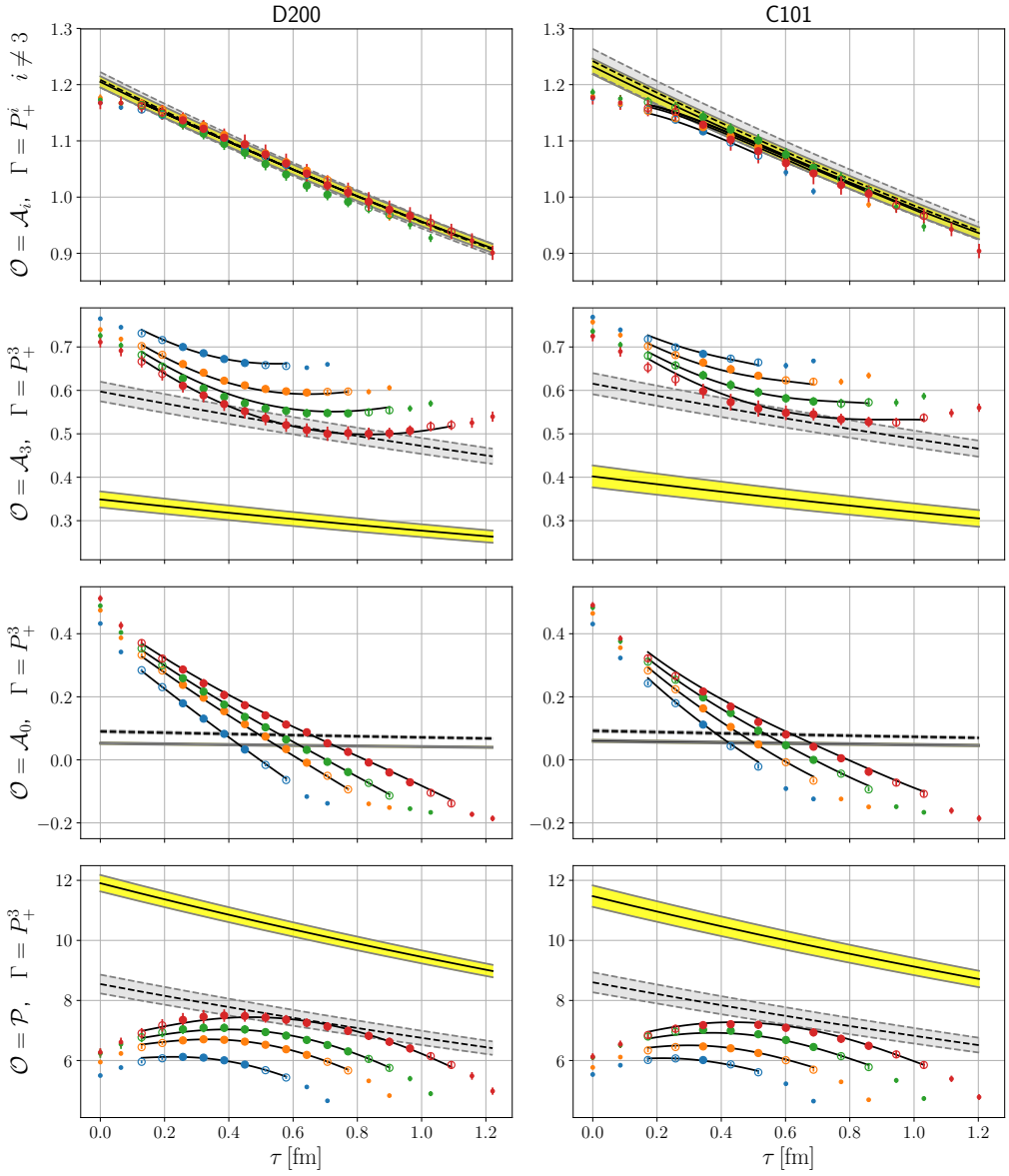

Figure 9: Fits to the ratio $R^{\vec{0},\vec{p}}_{\Gamma,\mathcal{O}}$ (defined in eq. (3.50)) at a momentum transfer $\vec{q} = -\vec{p} = \frac{2\pi}{L}(0,0,-1)^T$ for ensemble D200 (left side) and C101 (right side) for various channels and spin projections, where we have exploited rotational symmetry to average over equivalent directions. The solid lines correspond to a simultaneous fit to all the channels taking into account the leading $N\pi$ contribution using eqs. (4.29) and (4.30). The yellow band corresponds to the ground state. The gray band (dashed lines) shows the ground state extracted from a traditional fit using one generic excited state. The ground state contributions in the top (bottom) panels are sensitive to G_A (G_P), exclusively, while those in the second and the third row yield linear combinations of G_A and $G_{\tilde{P}}$ (see eqs. (B.3)-(B.6)). The bands include the statistical error and an error due to a variation of the fit range.

the pole enhanced $N\pi$ excited state contribution.[13] Indeed, we do not see any evidence in our numerical data for $N\pi$ or other low-lying multiparticle state contributions in this channel. This supports the choice made in previous lattice calculations to determine the axial form factor using this channel, in combination with traditional excited state fits.

The ansatz including the $N\pi$ excited states explicitly allows for a much better description of the data. In the case of D200 for instance, fits using block-correlated covariance matrices yield $\chi^2/\text{d.o.f.} \approx 1.31$ (including $N\pi$) versus $\chi^2/\text{d.o.f.} \approx 7.17$ (excluding $N\pi$). Note, however, that we have decided to use uncorrelated fits to extract the results. This avoids instabilities in the covariance matrix and prevents an underestimation of the statistical errors.

We find that almost the complete excited state contamination can be attributed to this $N\pi$ state, and that there are only very mild additional contributions at the sink (where $\vec{p}' = \vec{0}$). Nevertheless, we refrain from removing the additional generic excited states from the parametrization, in order to exclude an underestimation of the error in the extracted ground state contribution. Actually, one can also obtain a very good description of the data with even smaller statistical errors if one would use the ChPT-biased parametrizations discussed in section 4, which may indicate that possible higher order corrections are small. Nevertheless, the latter would entail a systematic uncertainty that we intend to avoid.

5.2.1. Predictions from EFT

We can confront the results of our fits with the corresponding ChPT prediction, see figure 10. In particular for the parameters d and d' in eqs. (4.29) and (4.30) ChPT yields a parameter free prediction, see eq. (4.32). Since d corresponds to one of our fit parameters, a direct comparison is possible (left plot in figure 10). As anticipated in section 4, the prediction using $G_A(Q^2)$ (circles) as the pion-nucleon coupling, instead of $g_A = G_A(0)$ (crosses), agrees well with our data, even at large Q^2, where one would usually not expect ChPT to work.

For our kinematics, the $N\pi$ excitation in the final state can also couple directly to the three-quark operator (this corresponds to the diagrams on the left and right in the second row of figure 6). Therefore, we can try to determine a' (defined in eq. (4.23)) directly from the data. A value $a' = 1$ means that the leading order ChPT estimate for the coupling of $N\pi$ to the three-quark operators calculated for local currents is exact in spite of the smearing. As one can see from the large statistical errors in the right plot of figure 10, our data is not very sensitive to a'. This is expected, since c and c' (which contains a') are suppressed compared to d and d' by one factor of $\mathcal{O}(\frac{m_\pi}{m})$. We neither

[13] The small shift within errors occurs because we perform a simultaneous fit such that the determined energy of the generic excited state is influenced by the fit in the other channels.

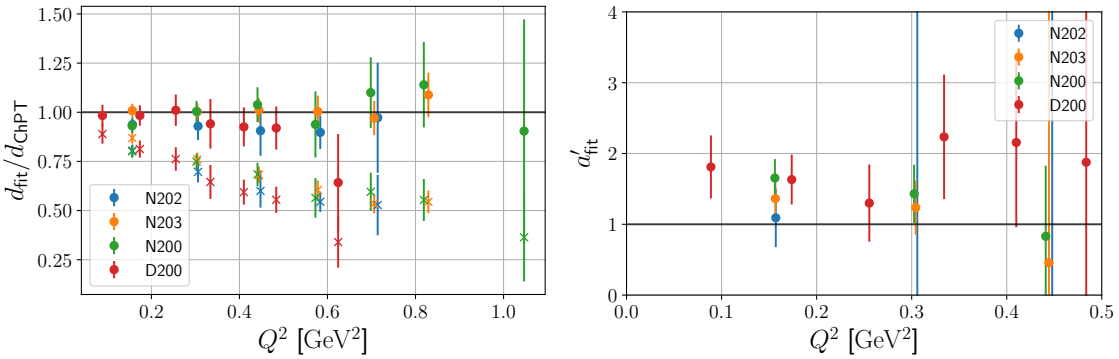

Figure 10: The plot on the left shows how well the parameter free tree-level ChPT prediction d_{ChPT} (circles; see eq. (4.32)) describes the data obtained from the fit (d_{fit}). As anticipated in section 4, the estimate using g_A instead of G_A (crosses) is not as good. This simply means that at nonzero momentum transfer the coupling of the pion to the nucleon is given by $G_A(Q^2)$ instead of g_A, as expected. In the plot on the right we show a' (cf. eq. (4.23)) obtained from our fit to the data. A value of $a' = 1$ would imply that the leading order ChPT estimate for the coupling of $N\pi$ to the three-quark operators is exact and that the operator smearing does not affect the coupling at all. As one can see, the data is not very sensitive to the value of a'. We do not see any significant momentum dependence and no strong smearing effect.

see a significant momentum dependence nor a strong smearing effect. If anything, the direct coupling of the three-quark operators to $N\pi$ seems to be slightly enhanced by the smearing.

5.2.2. Subtracted currents

In figure 11 we reinvestigate the subtraction method that was proposed in ref. [34]. As one can clearly see in the upper panels of figure 11, it almost entirely removes the seemingly linear behavior in the $\mathcal{A}_0$ channel caused by the $N\pi$ states. We find that the results for the ground state obtained from fits to the unsubtracted (solid lines; ground state yellow) and the subtracted (dashed lines; ground state red) data are mutually compatible, once we take into account the leading $N\pi$ contribution.[14] For the subtracted correlation functions, the fit ansatz given in section 4.4 has to be adapted appropriately, cf. appendix C. However, the ground state extracted from the subtracted data has a much larger statistical uncertainty. A closer look shows that the subtraction method

[14] Note that the subtraction method in combination with traditional excited state fits (as used in ref. [34]) does not yield the correct ground state. In particular in the pseudoscalar channel the correction overshoots and yields too large values. This has strong effects on $G_{\tilde{P}}$ and G_P, while G_A is unaffected. For a detailed study of this topic see also ref. [112]

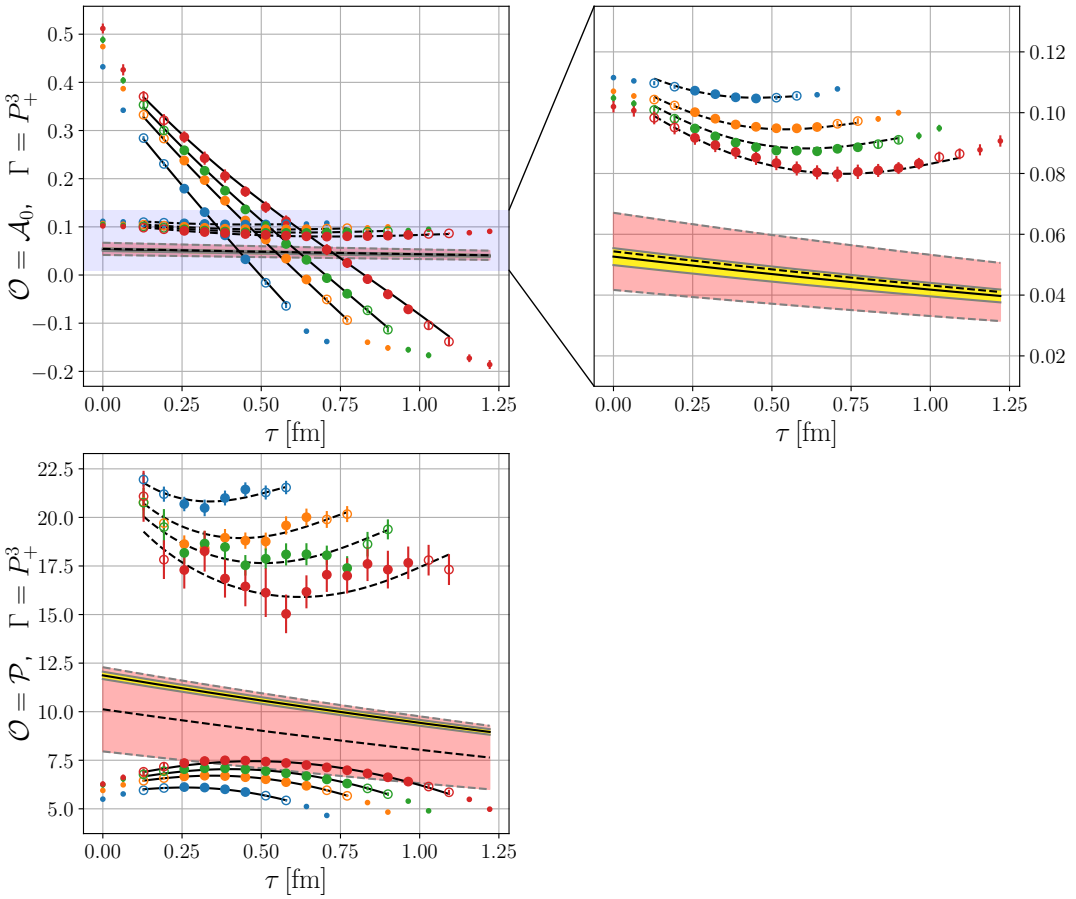

Figure 11: Comparison to the subtraction method proposed in ref. [34] for the ratio $R^{\vec{0},\vec{p}}_{\Gamma,\mathcal{O}}$ (defined in eq. (3.50)) at the momentum transfer $\vec{q} = -\vec{p} = \frac{2\pi}{L}(0,0,-1)^T$ for ensemble D200. The solid and dashed lines show fits to the unsubtracted and subtracted data, respectively, where the yellow and red bands show the corresponding ground state signals. In both cases we have taken into account the leading $N\pi$ contribution. For the subtracted current the fit ansatz has to be adapted, cf. appendix C.

here has fallen victim to its own success: since the largest and clearest excited state contaminations (in $\mathcal{A}_0$) have been subtracted successfully, the corresponding parameters cannot be determined as reliably, which in turn leads to a large error in the ground state. One can conclude that a combination of the analysis method presented here (taking into account the relevant $N\pi$ excitation explicitly in the fit to the correlation function) and the subtraction method proposed in ref. [34] is not advantageous.

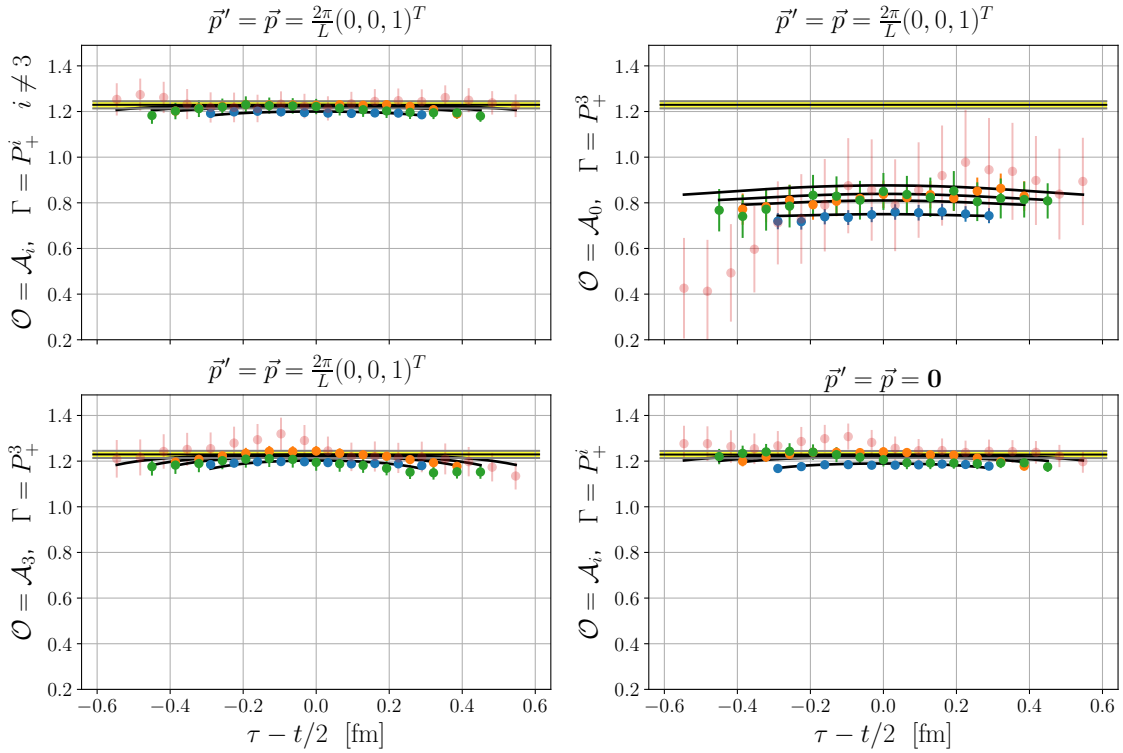

Figure 12: Fits to the ratio $R^{\vec{p},\vec{p}}_{\Gamma,\mathcal{O}}$ (as defined in eq. (3.50), but rescaled such that the ground state contribution in all the channels corresponds to g_A) at the momentum transfer $\vec{q} = \vec{0}$, with $\vec{p}' = \vec{p} = \frac{2\pi}{L}(0,0,1)^T$ and with $\vec{p}' = \vec{p} = \vec{0}$ for the contributing axial channels. This analysis has been performed on ensemble D201. The solid lines correspond to a simultaneous fit to all the channels taking into account the leading $N\pi$ contribution using eqs. (4.29) and (4.30), where the yellow band corresponds to the ground state. The bands include the statistical error and an error due to a variation of the fit range.

5.2.3. Finite final momentum check

As a consistency check, we have also considered the case $\vec{q} = 0$ with $\vec{p}' = \vec{p} \neq \vec{0}$ on one of our ensembles (D201). In this situation, eq. (4.29) predicts that the correlation functions of $\mathcal{A}_1$, $\mathcal{A}_2$, and $\mathcal{A}_3$ are not affected by the $N\pi$ excited state, while $\mathcal{A}_0$ gets a contribution $\propto \exp\big(-(E_N + m_\pi/2)t\big)\cosh\big(m_\pi(\tau - t/2)\big)$ in the three-point function. In figure 12 we show that this is indeed the case and that a simultaneous fit using eq. (4.29) yields a consistent description of the data for all the channels. This suggest that the observation in ref. [19] (see also ref. [33]), that a determination of g_A from the $\mathcal{A}_0$ channel in a moving frame (at $Q^2 = 0$) gives results different from those obtained using $\mathcal{A}_1$, $\mathcal{A}_2$, and $\mathcal{A}_3$, can be attributed to the same $N\pi$ excited state contaminations that have been problematic at nonzero Q^2 in other studies.

5.3. Excited state energies

In ref. [97] it has been proposed to use the signal of the timelike axialvector channel to determine the energy of the low-lying $N\pi$ excitation. The main difference with respect to the traditional excited state fit method is that one does not impose that the leading excited states in the two- and three-point functions have the same energy. In figure 13 (which roughly reproduces Fig. 3 of ref. [97][15]) we show the energy gaps to the various excited states obtained from two different fits to the correlation functions on ensemble D200 (with $m_\pi \approx 201\,\text{MeV}$). The dots (fit 1) have been obtained using the method proposed in ref. [97] (with the slight difference that we perform a simultaneous fit to all the channels instead of the two-step method presented there), while the crosses (fit 2) have been obtained using our fit ansatz from eqs. (4.29) and (4.30) but leaving $\Delta E_{N\pi}$ and $\Delta E'_{N\pi}$ as free fit parameters. In contrast to fit 1, fit 2 contains the additional excited states known from the two-point function, which leads to larger statistical uncertainties, in particular when the energy levels of the $N\pi$ state and the excited state from the two-point function (blue data points) get close to each other. Both kinds of fits lead to energies for the nucleon-pion states that approximately correspond to those of a noninteracting system (cf. the diagrams in the left and the right column of figure 6), which for our kinematics means that $E_{N\pi} = E_N(\vec{0}) + E_\pi(\vec{q})$ in the initial state (orange, dotted line) and $E'_{N\pi} = E_N(-\vec{q}) + E_\pi(\vec{q})$ in the final state (green, dashed line). The fact that both methods result in compatible values for the $N\pi$ excited state energies is encouraging and suggests that the physical interpretation obtained using EFT (cf. section 4) is correct.

In particular for the low-lying $N\pi$ state (which for our kinematics occurs in the initial state) at intermediate Q^2 one can see that the energies obtained from the fits slightly undershoot those of the noninteracting system. This effect is found to be a bit more significant in ref. [97]. One may speculate that this small deviation is due to an interaction between the nucleon and the pion. For the time being we have chosen to ignore these small deviations in our fits.

[15] Figure number from the arXiv v2 version.

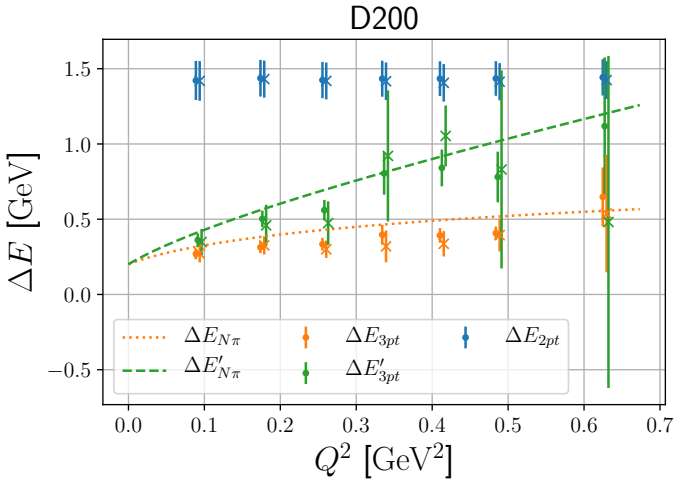

Figure 13: Energy gaps between the ground state and the excited states on the ensemble D200. The crosses have been obtained from a fit using the ansatz from eqs. (4.29) and (4.30) but taking $\Delta E_{3\mathrm{pt}} = \Delta E_{N\pi}$ and $\Delta E'_{3\mathrm{pt}} = \Delta E'_{N\pi}$ as free fit parameters, while $\Delta E_{2\mathrm{pt}} = \Delta E$ corresponds to the energy of the generic excited state determined from two- and three-point functions. The dots have been obtained from a fit without an explicit $N\pi$ state (i.e., $c = c' = d = d' = 0$ in eqs. (4.29) and (4.30)) but relaxing the condition that the excited state energies in two- and three-point function have to match (i.e., $\Delta E_{3\mathrm{pt}} = \Delta E$ and $\Delta E'_{3\mathrm{pt}} = \Delta E'$ from the three-point function and $\Delta E_{2\mathrm{pt}} = \Delta E$ from the two-point function). The orange, dotted line and the green, dashed line show the energy gaps for a noninteracting nucleon-pion system in the initial and the final state, respectively, as obtained from the diagrams in the left and the right column of figure 6. For our kinematics the energies are $E_{N\pi} = E_N(\vec{0}) + E_\pi(\vec{q})$ and $E'_{N\pi} = E_N(-\vec{q}) + E_\pi(\vec{q})$.

6. Form factors and extrapolations

6.1. Approximate restoration of PCAC and PPD

As mentioned in the introduction, form factors extracted from data using a traditional fit ansatz (with the same excited state energies in the two- and the three-point functions) show strong violations of PCAC and PPD. In particular in the case of PCAC this result was puzzling since the latter is fulfilled at the correlation function level (up to small, expected discretization effects). In order to quantify the violation of the PCAC relation at the form factor level (cf. eq. (3.28)), we define the ratio (cf. also ref. [29])

$$r_{\mathrm{PCAC}} = \frac{\frac{m_\ell}{m} G_P(Q^2) + \frac{Q^2}{4m^2} G_{\tilde{P}}(Q^2)}{G_A(Q^2)}, \tag{6.1}$$

where $r_{\mathrm{PCAC}} = 1$ if PCAC holds exactly. As the panel on the left-hand side of figure 14 demonstrates, using the parametrization of excited state contributions described in section 4.4, the PCAC relation is now fulfilled reasonably well on all ensembles, in particular on the ensembles with small pion masses, which previously exhibited the largest deviations. We emphasize that our fit ansatz does not impose PCAC on the ground state. While we see a significant improvement for all ensembles, small deviations of $\sim 5\%$ remain in some cases.

The induced pseudoscalar form factor is often estimated by

$$G_{\tilde{P}}(Q^2) \overset{?}{\approx} \frac{4m^2 G_A(Q^2)}{m_\pi^2 + Q^2} \quad \Rightarrow \quad r_{\mathrm{PPD}} = \frac{(m_\pi^2 + Q^2) G_{\tilde{P}}(Q^2)}{4m^2 G_A(Q^2)} \overset{?}{=} 1, \tag{6.2}$$

which is usually referred to as the pion pole dominance (PPD) assumption. Note that this relation does not have to hold exactly, even in the continuum. However, one would expect it to be satisfied at least approximately for small pion masses. The panel on the right-hand side of figure 14 shows that this is indeed the case if one explicitly takes into account the pion pole enhanced excited states in the spectral decomposition of the correlation function.

As reported in ref. [97] the problem can also be resolved (though within larger statistical uncertainties), if one uses a traditional multi-state fit ansatz, but relaxes the condition that the excited state energies of the two- and three-point functions have to match. One can exploit the huge excited state signal in the timelike axialvector channel to determine the energy gaps quite precisely (cf. also section 5.3). This can be seen as further confirmation that the previously observed large deviations from PCAC and PPD were indeed caused by unresolved, pion pole enhanced excited states. Note, however, that our ansatz (shown in eqs. (4.29) and (4.30)) conveys insight into the structure of

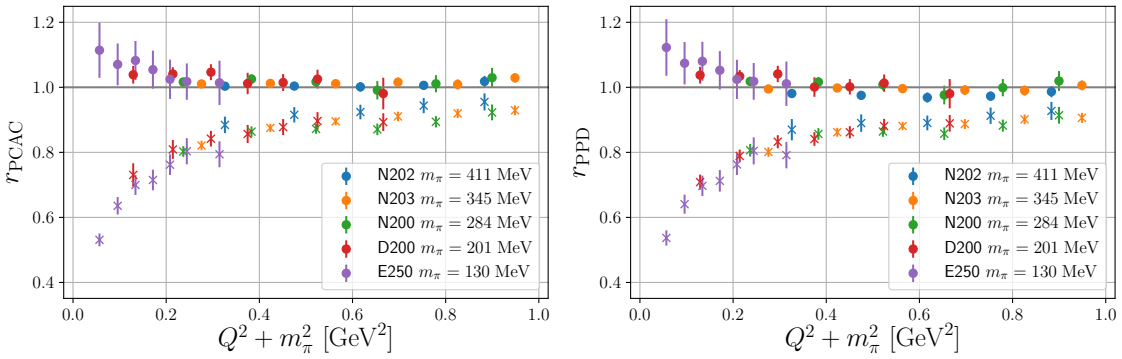

Figure 14: Violation of PCAC (left panel) and PPD (right panel) displayed for various ensembles along the trajectory with constant average quark mass (green lines in figure 7) at $\beta = 3.55$. The plots show the ratios defined in eqs. (6.1) and (6.2). The filled circles are obtained taking into account the pion pole enhanced excited states directly in the fit functions, while the crosses were obtained using a traditional fit ansatz (with the same excited state energies in the two- and three-point functions).

the excited state contamination. For instance, it is clear that, for $\mathcal{A}^\mu$ with $\mu = 1, 2, 3$, the result for G_A will not be affected by the leading $N\pi$ excited state contribution. Heuristically speaking, this is because G_A is not subject to pion pole dominance.

6.2. Parametrization and extrapolation

In this section we will explore two common form factor parametrizations: the traditional dipole ansatz and the z-expansion, which has become fashionable lately. In both cases we also consider parametrizations that are consistent with PCAC in the continuum (section 6.2.3) and we will use a generic ansatz for the combined continuum, chiral, and volume extrapolation explained in section 6.2.4.

6.2.1. Dipole ansatz

Motivated by eqs. (4.20), (4.21), and (4.22), we rewrite the form factors as

$$G_A(Q^2) \equiv A(Q^2)\,, \quad G_{\tilde{P}}(Q^2) \equiv \frac{4m^2}{Q^2 + m_\pi^2}\tilde{P}(Q^2)\,, \quad G_P(Q^2) \equiv \frac{m}{m_\ell}\frac{m_\pi^2}{Q^2 + m_\pi^2}P(Q^2), \quad (6.3)$$

where the pion pole is isolated (cf. also ref. [26]) such that one can use similar parametrizations for the residual form factors $X(Q^2)$, $X \in \{A, \tilde{P}, P\}$. The prefactors not only ensure that all the functions $X(Q^2)$ have the same mass dimension, but also enable us to obtain the correct chiral behavior of the form factors at small Q^2 despite using the same generic ansatz for all the form factors, see section 6.2.4 below.

One can consider various parametrizations for the residual form factors. For instance, one can use a dipole ansatz

$$X(Q^2) = \frac{g_X}{\left(1 + Q^2/M_X^2\right)^2}, \tag{6.4}$$

which reproduces the traditional dipole form for the axial form factor with the axial coupling g_A and the axial dipole mass M_A. This parametrization not only yields the correct low-energy behavior (if one uses a generic parametrization for the pion mass, volume, and lattice spacing dependence of g_X and M_X, cf. section 6.2.4 below), but also yields the correct asymptotic limit $G_A \propto 1/Q^4$, $G_{\tilde{P}} \propto 1/Q^6$, and $G_P \propto 1/Q^6$ [113], at large momentum transfer.

6.2.2. z-expansion

One may also parametrize the residual form factors using the z-expansion [114, 115], which automatically imposes analyticity constraints. This corresponds to an expansion of the form factors in the variable

$$z(Q^2) = \frac{\sqrt{t_{\text{cut}} + Q^2} - \sqrt{t_{\text{cut}} - t_0}}{\sqrt{t_{\text{cut}} + Q^2} + \sqrt{t_{\text{cut}} - t_0}}, \tag{6.5}$$

where $t_{\text{cut}} = 9m_\pi^2$ is the particle production threshold and t_0 is a tunable parameter.[16] We then parametrize

$$X(Q^2) = \sum_{n=0}^{N} a_n^X z(Q^2)^n, \tag{6.6}$$

where the $X(Q^2)$ are defined as in section 6.2.1. Without additional constraints this parametrization has $N+1$ free parameters and is usually called a $z^{(N+1)}$ ansatz. Again, the generic parametrization discussed in section 6.2.4 will yield the correct chiral behavior. However, eq. (6.6) does not incorporate any constraints at large momentum transfer. In order to reproduce the correct asymptotic behavior one has to enforce restrictions of the type

$$\lim_{Q\to\infty} Q^k X(Q^2) \stackrel{!}{=} 0, \quad \text{for} \quad 0 \le k \le n\,, \tag{6.7}$$

which can be implemented (as long as $n < N$) by demanding

$$0 = \sum_{l=0}^{N} l^k a_l^X, \quad \text{for} \quad 0 \le k \le n\,. \tag{6.8}$$

[16] We have set t_0 to $-t_{\text{cut}}^{\text{phys}} = -9m_{\pi,\text{phys}}^2$ in our analysis. By choosing a negative value one can avoid the erratic behavior at $t_{\text{cut}} = t_0$, while approaching the chiral limit.

These can be incorporated, e.g., by fixing

$$a_k^X = \frac{(-1)^{k+n+1}}{k!(n-k)!} \sum_{l=n+1}^{N} \frac{l!}{(l-(n+1))!(l-k)} a_l^X, \quad \text{for} \quad 0 \le k \le n. \tag{6.9}$$

Alternatively, one can solve the problem recursively by setting

$$a_k^X = \frac{(-1)^{2k+1}}{k!} \sum_{l=k+1}^{N} \frac{l!}{(l-(k+1))!(l-k)} a_l^X, \quad \text{for} \quad 0 \le k \le n. \tag{6.10}$$

To enforce the correct scaling in the asymptotic limit, $G_A \propto 1/Q^4$, $G_{\tilde{P}} \propto 1/Q^6$, and $G_P \propto 1/Q^6$ [113], we have to apply the formulas above for $n = 3$, thereby fixing a_k^X for $k = 0, 1, 2, 3$, such that 4 coefficients are fixed and only $N - 3$ coefficients are free parameters.[17] This parametrization with the correct asymptotic behavior is usually referred to as the $z^{4+(N-3)}$ ansatz.

6.2.3. Consistency with PCAC in the continuum

Let us assume the following ansatz for the extrapolation to the physical point ($m_\pi \to m_\pi^{\text{phys}}$, $a \to 0$, $L \to \infty$),

$$x = x^{\mathfrak{a}}(m_\pi, m_K, L) x^a(a, m_\pi, m_K), \tag{6.11}$$

where we have factorized the dependence on the lattice spacing into x^a with

$$x^a(0, m_\pi, m_K) = 1 \tag{6.12}$$

for all parameters in the form factor decompositions, i.e., $x \in \{g_A, M_A, g_{\tilde{P}}, M_{\tilde{P}}, g_P, M_P\}$ for the dipole ansatz, and $x \in \left\{a_n^A, a_n^{\tilde{P}}, a_n^P\right\}$, $n = 4, 5 \ldots, N$ for the z-expansion. This allows us to perform a combined fit to all ensembles for each form factor. The expressions used for $x^{\mathfrak{a}}$ and x^a will be given below in section 6.2.4.

Since we know that the partial conservation of the axial current has to be satisfied exactly in the continuum limit, we can use eq. (3.28) to obtain G_P from G_A and $G_{\tilde{P}}$

$$\frac{m_\ell}{m} G_P(Q^2) = G_A(Q^2) - \frac{Q^2}{4m^2} G_{\tilde{P}}(Q^2) + \mathcal{O}(a^2). \tag{6.13}$$

However, one then has to impose the additional constraints

$$\lim_{Q \to \infty} Q^n \left(G_A(Q^2) - \frac{Q^2}{4m^2} G_{\tilde{P}}(Q^2) \right) \Big|_{a=0} \stackrel{!}{=} 0 \tag{6.14}$$

[17] We neglect possible $\mathcal{O}(Q^2 a^2)$ lattice artifacts since we only have lattice data with $Q^2 \ll a^{-2}$. Such effects could be implemented by relaxing the constraint (6.7) at nonzero lattice spacing.

via

$$\lim_{Q\to\infty} Q^n \left(A(Q^2) - \tilde{P}(Q^2) \right) \Big|_{a=0} \stackrel{!}{=} 0 \quad \text{for} \quad n \in \{4,5\}\,, \tag{6.15}$$

in order to preserve the correct asymptotic behavior of G_P, cf. also eq. (6.3). For the dipole parametrizations one gets

$$g_A M_A^4 \Big|_{a=0} \stackrel{!}{=} g_{\tilde{P}} M_{\tilde{P}}^4 \Big|_{a=0}\,. \tag{6.16}$$

The equivalent constraints for the z-expansion can be obtained using eq. (6.9) and read

$$\left(a_k^A - a_k^{\tilde{P}} \right) \Big|_{a=0} = \frac{(-1)^k}{k!(5-k)!} \sum_{l=6}^{N} \frac{l!}{(l-6)!(l-k)} \left(a_l^A - a_l^{\tilde{P}} \right) \Big|_{a=0} \quad \text{for} \quad k \in \{4,5\}. \tag{6.17}$$

Let us now parametrize the pseudoscalar form factor using

$$P(Q^2) = \left(1 + \frac{Q^2}{m_\pi^2} \right) P_1(Q^2) - \frac{Q^2}{m_\pi^2} P_2(Q^2). \tag{6.18}$$

This ansatz becomes consistent with PCAC in the continuum limit once we demand that

$$P_1(Q^2) \Big|_{a=0} = A(Q^2) \Big|_{a=0}\,, \qquad P_2(Q^2) \Big|_{a=0} = \tilde{P}(Q^2) \Big|_{a=0}\,. \tag{6.19}$$

Unfortunately, PCAC is broken on the lattice by discretization effects, such that $P_1(Q^2)$ and $P_2(Q^2)$ differ from $A(Q^2)$ and $\tilde{P}(Q^2)$ at nonzero lattice spacing. Hence, we use the same ansatz for both (e.g., the dipole form (6.4) or the z-expansion (6.6)), but we start with independent parameters. Here, the asymptotic constraints yield

$$\lim_{Q\to\infty} Q^n \left(P_1(Q^2) - P_2(Q^2) \right) \stackrel{!}{=} 0 \quad \text{for} \quad n < 6, \tag{6.20}$$

independent of a. Note, that eq. (6.19) and (6.20) can only be fulfilled simultaneously if the axial and induced pseudoscalar form factors meet the requirement (6.14). For the two parametrizations (cf. sections 6.2.1 and 6.2.2) that we consider, the constraints for $n < 4$ hold automatically. Similar to the above, the remaining two constraints can be satisfied by

$$g_{P_1} M_{P_1}^4 \stackrel{!}{=} g_{P_2} M_{P_2}^4 \tag{6.21}$$

when using the dipole ansatz, and by

$$\left(a_k^{P_1} - a_k^{P_2} \right) = \frac{(-1)^k}{k!(5-k)!} \sum_{l=6}^{N} \frac{l!}{(l-6)!(l-k)} \left(a_l^{P_1} - a_l^{P_2} \right) \quad \text{for} \quad k \in \{4,5\}, \tag{6.22}$$

when using the z-expansion.

To summarize, if we wish our form factor parametrizations to obey PCAC in the continuum limit, we start by parametrizing $P(Q^2)$ as in eq. (6.18), thereby introducing more parameters at first. However, as discussed above, these parameters are highly constrained such that the ansatz enforcing PCAC will have less free fit parameters in the end. Using the dipole ansatz, we have $g_A, M_A, g_{\tilde{P}}, M_{\tilde{P}}, g_{P_1}, M_{P_1}, g_{P_2}, M_{P_2}$, which can be factorized in a lattice spacing dependent and a lattice spacing independent part as shown in eq. (6.11). The constraints discussed above can be incorporated by setting

$$g_{P_2} = g_{P_1}\left(\frac{M_{P_1}}{M_{P_2}}\right)^4, \qquad g_{P_1}^{\mathfrak{a}} = g_A^{\mathfrak{a}}, \qquad \left[g_{P_2}^{\mathfrak{a}} = g_{\tilde{P}}^{\mathfrak{a}},\right] \tag{6.23}$$

$$g_{\tilde{P}}^{\mathfrak{a}} = g_A^{\mathfrak{a}}\left(\frac{M_A^{\mathfrak{a}}}{M_{\tilde{P}}^{\mathfrak{a}}}\right)^4, \qquad M_{P_1}^{\mathfrak{a}} = M_A^{\mathfrak{a}}, \qquad M_{P_2}^{\mathfrak{a}} = M_{\tilde{P}}^{\mathfrak{a}}, \tag{6.24}$$

where the constraint in brackets is not independent of the others. If one uses the z-expansion, one starts with $a_n^A, a_n^{\tilde{P}}, a_n^{P_1}, a_n^{P_2}$, $n = 4, 5 \ldots, N$. Again, we assume these coefficients to be factorized as in eq. (6.11). Here, the constraints discussed above can be implemented by setting

$$a_k^{P_2} = a_k^{P_1} + \frac{(-1)^k}{k!(5-k)!}\sum_{l=6}^{N}\frac{l!}{(l-6)!(l-k)}\left(a_l^{P_2} - a_l^{P_1}\right) \quad \text{for} \quad k \in \{4,5\}, \tag{6.25}$$

$$a_k^{\tilde{P},\mathfrak{a}} = a_k^{A,\mathfrak{a}} + \frac{(-1)^k}{k!(5-k)!}\sum_{l=6}^{N}\frac{l!}{(l-6)!(l-k)}\left(a_l^{\tilde{P},\mathfrak{a}} - a_l^{A,\mathfrak{a}}\right) \quad \text{for} \quad k \in \{4,5\}, \tag{6.26}$$

$$a_k^{P_1,\mathfrak{a}} = a_k^{A,\mathfrak{a}} \quad \text{for} \quad k \in \{4,5,\ldots,N\}, \tag{6.27}$$

$$a_k^{P_2,\mathfrak{a}} = a_k^{\tilde{P},\mathfrak{a}} \quad \text{for} \quad k \in \{\left[4,5,\right]6,\ldots,N\}. \tag{6.28}$$

As above, the constraints in brackets are not independent of the others.

6.2.4. Continuum, quark mass, and volume extrapolation

In our combined analysis of all the ensembles we will consider four kinds of fits: the dipole ansatz (2P), the z-expansion with the correct asymptotic behavior ($z^{4+(N-3)}$), and the two corresponding parametrizations where PCAC holds automatically in the continuum (!2P and $!z^{4+(N-3)}$, respectively). They are listed in table 4. We have factorized the occurring parameters $x = x^{\mathfrak{a}}x^a$ (see eq. (6.11)) into a continuum limit part $x^{\mathfrak{a}}$, and a part which describes discretization effects, x^a, where $x^a \to 1$ for $a \to 0$, see eq. (6.12). In the parametrizations that respect PCAC, the number of parameters is reduced due to the constraints derived in section 6.2.3 (see also table 4). We perform a combined

id	PCAC	$x^{\not a}$	x^a	#params per FF
2P	×	$g_A^{\not a}$, $g_{\tilde{P}}^{\not a}$, $g_P^{\not a}$, $M_A^{\not a}$, $M_{\tilde{P}}^{\not a}$, $M_P^{\not a}$	g_A^a, $g_{\tilde{P}}^a$, g_P^a, M_A^a, $M_{\tilde{P}}^a$, M_P^a	18
!2P	✓	$g_A^{\not a}$, $M_A^{\not a}$, $M_{\tilde{P}}^{\not a}$	g_A^a, $g_{\tilde{P}}^a$, $g_{P_1}^a$, M_A^a, $M_{\tilde{P}}^a$, $M_{P_1}^a$, $M_{P_2}^a$	13
$z^{4+(N-3)}$	×	$a_4^{A,\not a}$, $a_5^{A,\not a}$, …, $a_N^{A,\not a}$, $a_4^{\tilde{P},\not a}$, $a_5^{\tilde{P},\not a}$, …, $a_N^{\tilde{P},\not a}$, $a_4^{P,\not a}$, $a_5^{P,\not a}$, …, $a_N^{P,\not a}$	$a_4^{A,a}$, $a_5^{A,a}$, …, $a_N^{A,a}$, $a_4^{\tilde{P},a}$, $a_5^{\tilde{P},a}$, …, $a_N^{\tilde{P},a}$, $a_4^{P,a}$, $a_5^{P,a}$, …, $a_N^{P,a}$	$9N-27$
$!z^{4+(N-3)}$	✓	$a_4^{A,\not a}$, $a_5^{A,\not a}$, …, $a_N^{A,\not a}$, $a_6^{\tilde{P},\not a}$, $a_7^{\tilde{P},\not a}$, …, $a_N^{\tilde{P},\not a}$	$a_4^{A,a}$, $a_5^{A,a}$, …, $a_N^{A,a}$, $a_4^{\tilde{P},a}$, $a_5^{\tilde{P},a}$, …, $a_N^{\tilde{P},a}$, $a_4^{P_1,a}$, $a_5^{P_1,a}$, …, $a_N^{P_1,a}$, $a_6^{P_2,a}$, $a_7^{P_2,a}$, …, $a_N^{P_2,a}$	$8N-30$

Table 4: Overview of the form factor parametrizations. We will use the dipole ansatz (2P) and the z-expansion with the correct asymptotic behavior ($z^{4+(N-3)}$) as described in sections 6.2.1 and 6.2.2, respectively. For both cases we also consider parametrizations where PCAC is fulfilled in the continuum limit (marked by a preceding ! in the identifier), cf. section 6.2.3. In the rightmost column, we give the total number of fit parameters used for the combined continuum, quark mass, and volume extrapolation per form factor, assuming that formulas (6.29) and (6.30) are used for the extrapolation of $x^{\not a}$ and x^a, respectively.

continuum, quark mass, and volume extrapolation using the generic ansatz

$$\begin{aligned} x^{\not a}(m_\pi, m_K, L) &= c_1^x + c_2^x \bar{m}^2 + c_3^x \delta m^2 \\ &\quad + c_4^x \frac{m_\pi^2}{\sqrt{m_\pi L}} e^{-m_\pi L} + c_5^x \frac{m_K^2}{\sqrt{m_K L}} e^{-m_K L} + c_6^x \frac{m_\eta^2}{\sqrt{m_\eta L}} e^{-m_\eta L}, \end{aligned} \tag{6.29}$$

$$x^a(a, m_\pi, m_K) = 1 + a^2 \left(d_1^x + d_2^x \bar{m}^2 + d_3^x \delta m^2 \right), \tag{6.30}$$

where we set $m_\eta^2 = (4m_K^2 - m_\pi^2)/3$ using the Gell-Mann–Oakes–Renner relation [116]. The functional form of the finite volume terms is motivated by the leading contribution found in ChPT calculations of the axial coupling, cf. refs. [117, 118]. To parametrize the quark mass plane we have defined the linear combinations

$$\delta m^2 = m_K^2 - m_\pi^2 \approx B(m_s - m_l), \tag{6.31}$$

$$\bar{m}^2 = \left(2m_K^2 + m_\pi^2\right)/3 \approx 2B\left(m_s + 2m_l\right)/3, \tag{6.32}$$

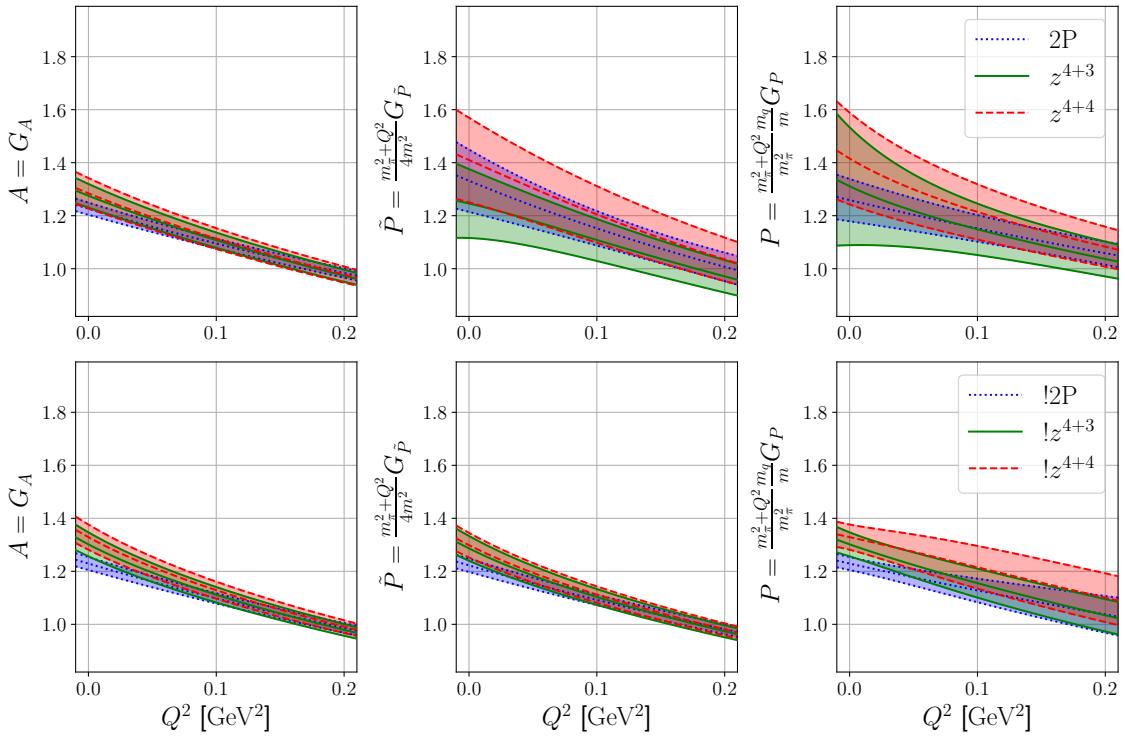

Figure 15: Comparison of continuum results at the physical point for the residual form factors obtained using the different fits, cf. table 4. The fits enforcing PCAC in the continuum (lower panels) yield significantly smaller statistical errors. The mean values of the plotted curves can be reproduced using the parameters provided in table 5.

such that $\delta m = 0$ corresponds to exact flavor symmetry, i.e., the blue line in figure 7, while the green line with physical average masses is defined by $\bar{m} = \text{phys.} \approx 411\,\text{MeV}$. Along the line of an approximately physical strange quark mass, i.e., the red line in figure 7, the average mass varies; all ensembles used in this study have $\bar{m} < 500\,\text{MeV}$. Note that our additional ensembles with exact flavor symmetry (along the blue line in figure 7) facilitate the determination of the parameters c_1^x, c_2^x, d_1^x, and d_2^x.

6.3. Results

Figure 15 provides a compilation of (continuum, quark mass, and finite volume extrapolated) form factors that have been obtained from the parametrizations discussed in the previous sections. The parameters producing the central values can be taken from table 5. Surprisingly, even the fits using a dipole ansatz (2P) give a reasonable description of the data (actually, it has in most cases the smallest χ^2/d.o.f. of all fits, cf. table 5), despite the fact that the functional form is very constrained. However, the latter may

id	X	χ^2/d.o.f.	g_X	M_X [GeV]
2P	A	0.80	1.226	1.311
	$\tilde{P}$	0.65	1.332	1.154
	P	0.66	1.259	1.487
!2P	$A = P_1$	0.71	1.229	1.312
	$\tilde{P} = P_2$		1.222	1.313

id	X	χ^2/d.o.f.	a_0^X	a_1^X	a_2^X	a_3^X	a_4^X	a_5^X	a_6^X	a_7^X
z^{4+3}	A	0.94	1.009	-1.756	-1.059	1.621	3.919	-5.739	2.005	
	$\tilde{P}$	0.66	1.008	-1.831	-1.713	4.994	-1.522	-1.984	1.047	
	P	0.66	1.066	-1.461	-1.053	-2.504	12.446	-12.260	3.766	
$!z^{4+3}$	$A = P_1$	0.83	1.013	-1.713	-0.591	-0.771	7.790	-8.418	2.689	
	$\tilde{P} = P_2$		1.007	-1.678	-0.680	-0.653	7.701	-8.382	2.684	
z^{4+4}	A	0.97	1.014	-1.777	-1.026	1.596	3.928	-5.740	2.005	-0.00003
	$\tilde{P}$	0.61	1.080	-2.211	-0.920	4.201	-1.164	-2.016	1.031	0.00001
	P	0.66	1.117	-1.692	-0.641	-2.858	12.583	-12.271	3.762	-0.00012
$!z^{4+4}$	$A = P_1$	0.79	1.027	-1.773	-0.488	-0.854	7.818	-8.418	2.688	0.00002
	$\tilde{P} = P_2$		1.015	-1.703	-0.662	-0.625	7.649	-8.352	2.678	-0.00031

Table 5: Results for the parameters at the physical point in the continuum for the dipole ansatz (6.4) and the z-expansion (6.6), together with the uncorrelated χ^2 per degree of freedom of the corresponding fit. For convenience, we also provide the values for the parameters, which are entirely fixed by constraints.

lead to an underestimation of the error, and it may also induce a smaller slope at zero momentum transfer. In order to reduce this bias one may relax the constraints due to the choice of parametrization. The currently most popular and probably best suited ansatz for this task is the z-expansion described in section 6.2.2. To this end, we have performed z^{4+3} and z^{4+4} fits (and the corresponding fits that are constrained to be consistent with PCAC in the continuum limit). While the z^{4+3} fit is almost as restrictive as the dipole ansatz (27 vs. 18 parameters per form factor), expansions with a larger number of parameters (z^{4+4}, z^{4+5}, etc.) introduce less and less parametrization bias. In practice, however, the choice will always be a balancing act between reducing the parametrization bias and being able to control the systematics of all occurring parameters. Therefore, the statistical quality of the data and its coverage of lattice spacings, quark masses, and volumes are a deciding factor.

We emphasize that PCAC was not enforced when extracting the form factors from fits to the correlators. Nevertheless, due to the advances in the understanding of ex-

cited state contaminations in the correlation functions, we are now able to resolve the ground state contributions such that the resulting form factors agree with PCAC (and also PPD) reasonably well. This enables us to perform combined fits to all form factors using parametrizations that automatically obey PCAC in the continuum limit. As one can easily see in table 4, the resulting parametrizations are much more restrictive than their counterparts. For example, the dipole fit (!2P) has in total three free parameters (at the physical point in the continuum limit) for all form factors. However, in contrast to the parametrization bias discussed above, the PCAC constraints do not evoke any kind of systematic uncertainty, since they only reflect an exactly known symmetry. Unsurprisingly, we find that the continuum extrapolation is more stable when using these PCAC-consistent parametrizations. Overall, we find that both the !2P and the $!z^{4+3}$ fit yield very good descriptions of the data (χ^2/d.o.f. = 0.71 and χ^2/d.o.f. = 0.83, respectively), while still allowing for a controlled extrapolation to the physical point. Our final results are therefore based on these fits. The $!z^{4+4}$ fit also provides a very good description of our data (χ^2/d.o.f. = 0.79). However, it is less trustworthy since it relies on an excessive number of parameters, which leads to larger systematic uncertainties in the combined continuum, quark mass, and volume extrapolation.

In figures 16, 17, and 18, we show our data and how well it is described by the $!z^{4+3}$ fit. (For the !2P fit such plots look equally convincing.) The 6 rows in each figure correspond to the five available lattice spacings and to the continuum limit, while the columns correspond to the different quark mass trajectories, see the explanation in section 5.1. Along the trM and msc trajectories, some of the ensembles have close to physical masses (C101, C102, D200, D450, D451, with $m_\pi \approx 200\,\text{MeV}$ and, in particular, D150 and E250, with $m_\pi \approx 130\,\text{MeV}$). Note that the sym trajectory with exact flavor symmetry does not approach the physical point in the quark mass plane. The colored curves show the mean fit result evaluated at the masses, volume, and lattice spacing of the respective ensemble, while the yellow band corresponds to the extrapolated result at physical masses, in infinite volume, and at the lattice spacing for the particular row. The data show that the form factors exhibit an increasing slope (in Q^2) for decreasing pion masses (as one would expect) and lattice spacings. In figure 16 one can see that also the data for $g_A = G_A(0)$ is well described by the fit. However, in particular for large pion masses, the data at $Q^2 = 0$ lies significantly below the extrapolated value, which highlights the importance of the extrapolation to physical masses. In this context one should note that the z-expansion (shown here) exhibits a different mass dependence than the dipole ansatz, since the pion mass directly enters the definition of z in eq. (6.5). What is harder to see from the curves is the increase of the slope towards the smaller lattice spacings. In order to provide some way for the reader to appreciate how big this effect is, we indicate the slope of G_A at $Q^2 = 0$ in figure 16 by a dashed line. In figures 17

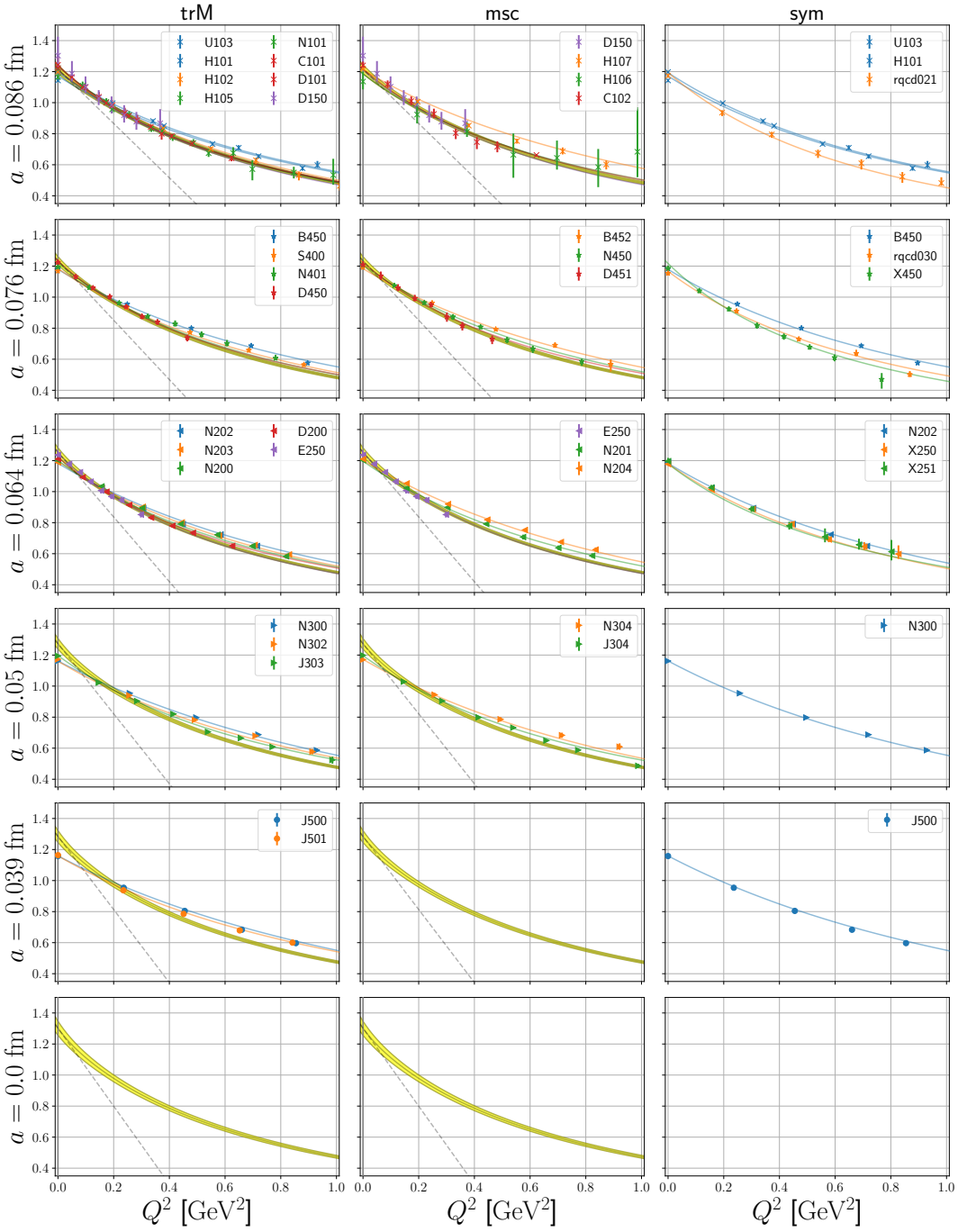

Figure 16: The axial form factor $G_A(Q^2)$ obtained using the $!z^{4+3}$ ansatz fitted to all available ensembles. This is a combined fit to all form factors with χ^2/d.o.f. = 0.83. The panels correspond to different lattice spacings and quark mass trajectories (see section 5.1), where the yellow band corresponds to the form factor obtained from the fit, evaluated at physical masses and at infinite volume, but at the lattice spacing corresponding to the particular row.

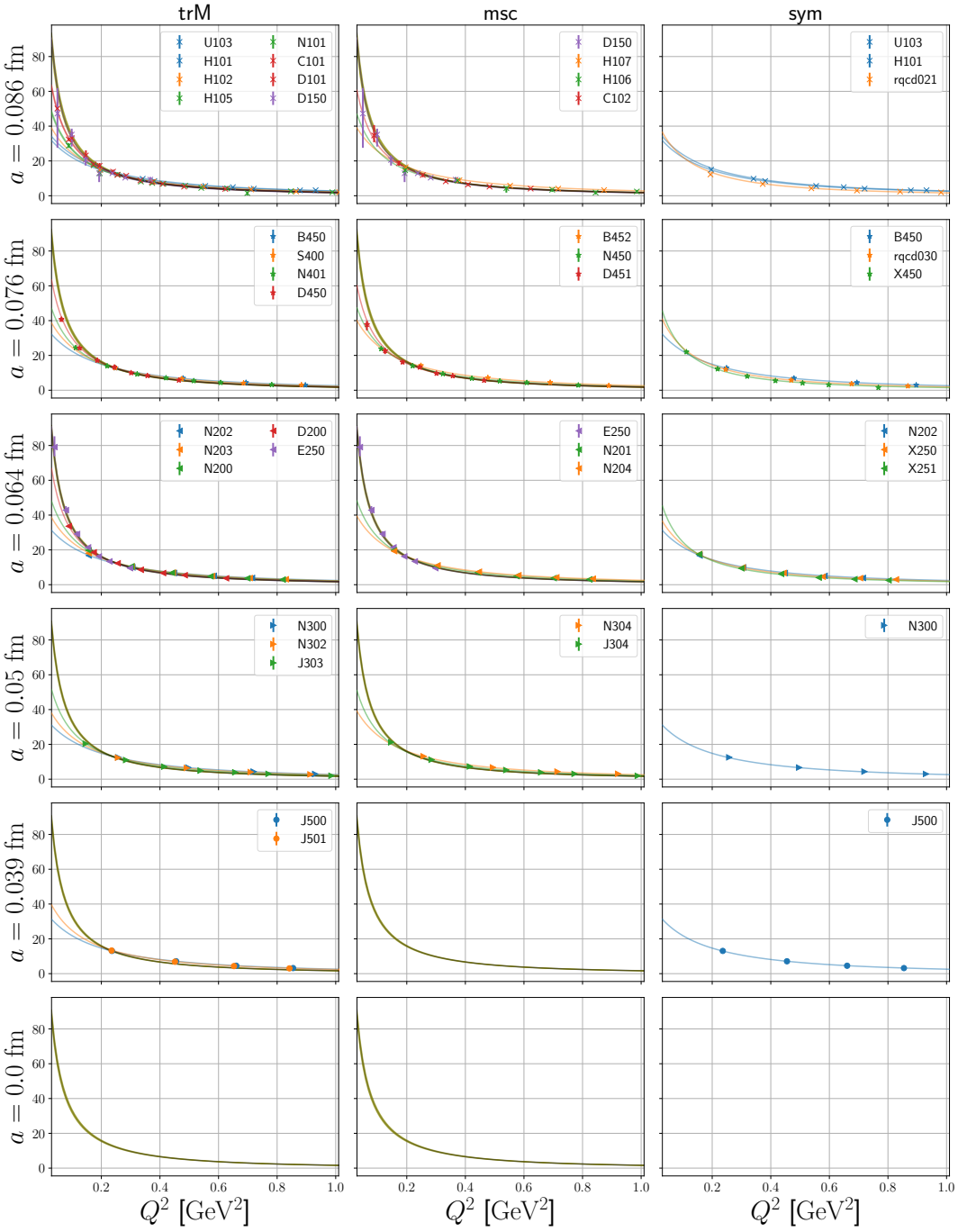

Figure 17: The induced pseudoscalar form factor $G_{\tilde{P}}(Q^2)$ obtained using the $!z^{4+3}$ ansatz fitted to all available ensembles. This is a combined fit to all form factors with χ^2/d.o.f. = 0.83. The panels correspond to different lattice spacings and quark mass trajectories (see section 5.1), where the yellow band corresponds to the form factor obtained from the fit, evaluated at physical masses and at infinite volume, but at the lattice spacing corresponding to the particular row.

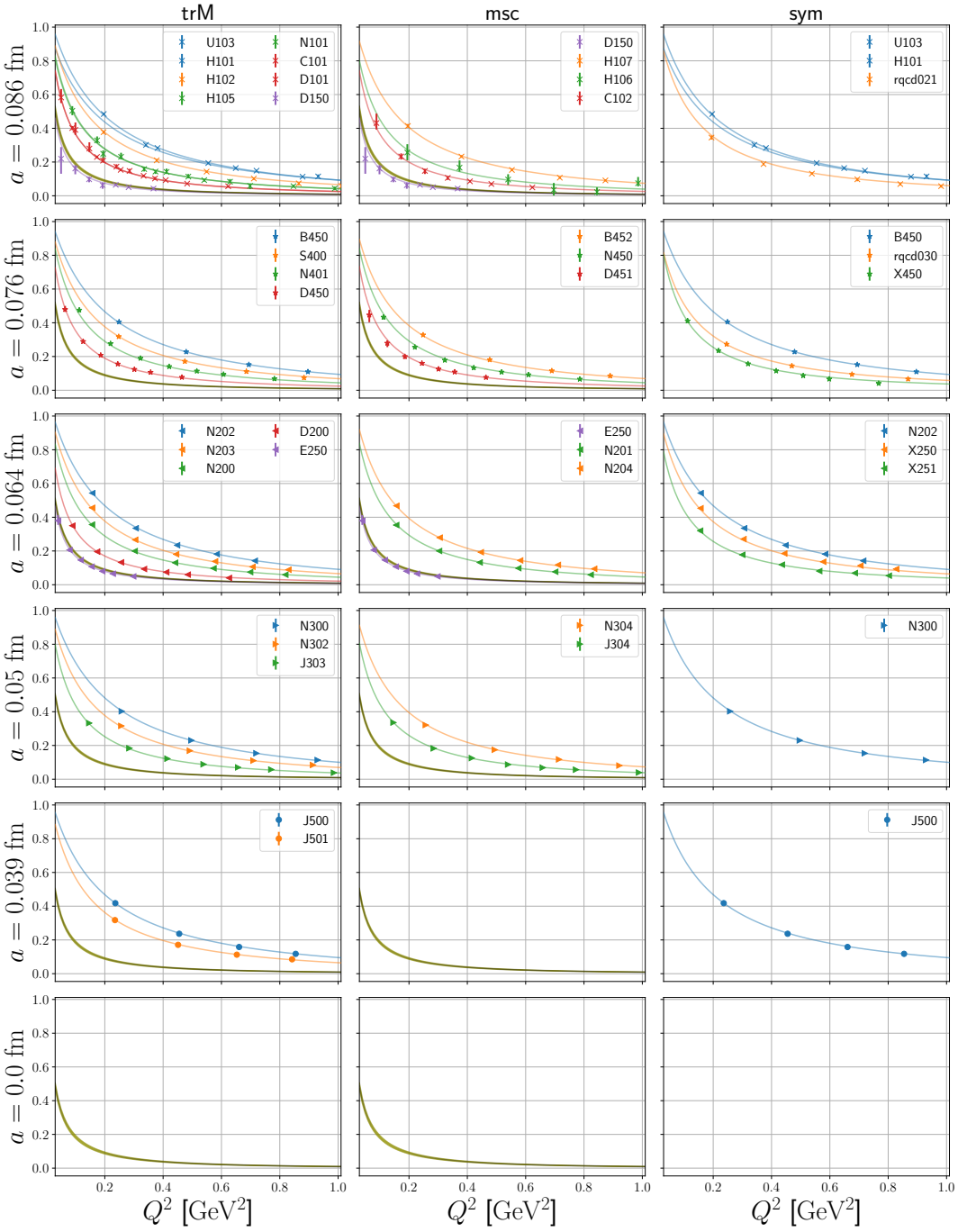

Figure 18: The pseudoscalar form factor $\frac{m_\ell}{m} G_P(Q^2)$ obtained using the $!z^{4+3}$ ansatz fitted to all available ensembles. This is a combined fit to all form factors with χ^2/d.o.f. = 0.83. The panels correspond to different lattice spacings and quark mass trajectories (see section 5.1), where the yellow band corresponds to the form factor obtained from the fit, evaluated at physical masses and at infinite volume, but at the lattice spacing corresponding to the particular row.

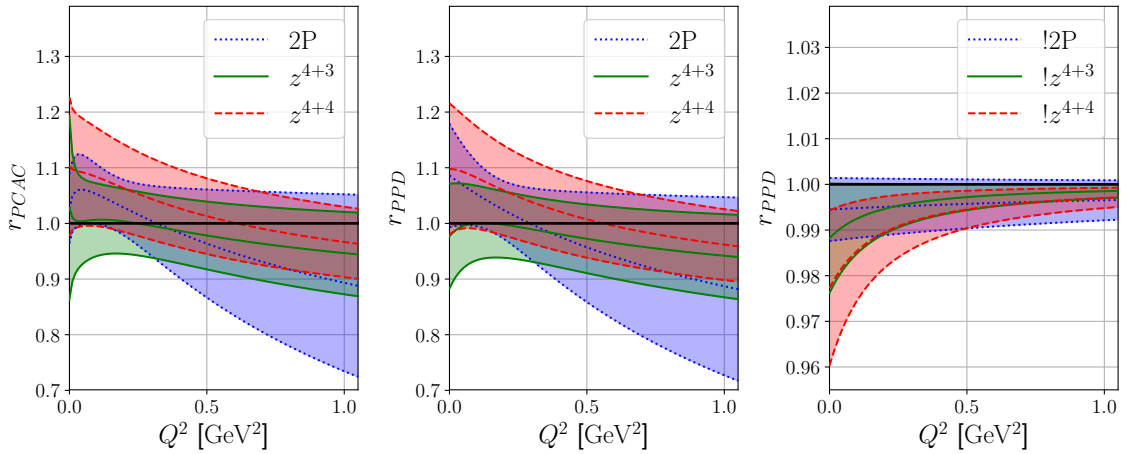

Figure 19: The r_{PCAC} (left panel) and r_{PPD} (center panel) ratios (defined in eqs. (6.1) and (6.2)) at the physical point in the continuum limit. These are obtained using a 2P (dotted, blue), z^{4+3} (solid, green) or a z^{4+4} (dashed, red) fit ansatz. In the case of r_{PPD}, we also show results of the corresponding fits that are constrained to be consistent with PCAC in the continuum limit (right panel), cf. table 4.

and 18 it is particularly encouraging that the data for our physical mass ensemble at small lattice spacing (E250) nicely reproduces the expected pion pole structure in the (induced) pseudoscalar form factor (cf. eq. (6.3)).

Above, in figure 14, we have demonstrated that the nucleon form factor data extracted from the correlation functions using the results presented in section 4.4 agree reasonably well with PCAC and PPD. In figure 19 we show the result for the ratios r_{PCAC} (left panel) and r_{PPD} (center panel) after the extrapolation, using the previously discussed form factor parametrizations that do not enforce PCAC. We find that both PCAC and PPD are fulfilled within large statistical errors. As one can see by comparing the center and the right panel (note the difference in the scale between the two plots), the dipole and z-expansion fits with enforced PCAC relation allow for a much better resolution of possible deviations from the pion pole dominance assumption for the induced pseudoscalar form factor. We find the PPD assumption to be valid at the 1%–2% level at all momentum transfers, independent of the parametrization.

The results for the form factors at zero momentum transfer and for the mean squared radii are given in table 6, where we also provide the induced pseudoscalar coupling at the muon capture point

$$g_P^\star = \frac{m_\mu}{2m} G_{\tilde{P}}(0.88 m_\mu^2), \tag{6.33}$$

id	$G_A(0)$	$r_A^2\,[\mathrm{fm}^2]$	$G_{\tilde{P}}(0)$	$r_{\tilde{P}}^2\,[\mathrm{fm}^2]$	$\frac{m_\mu}{m}G_P(0)$	$r_P^2\,[\mathrm{fm}^2]$	$g_P^\star$	$g_{\pi NN}$
2P	1.226(23)	0.272(21)	246(22)	11.98(12)	1.259(80)	11.85(7)	9.02(76)	15.55(3.00)
!2P	1.229(24)	0.272(21)	226(5)	11.91(2)	1.229(24)	11.84(8)	8.30(17)	12.93(55)
z^{4+3}	1.275(45)	0.351(58)	231(24)	11.85(22)	1.311(222)	12.04(36)	8.48(84)	13.23(3.06)
$!z^{4+3}$	1.302(45)	0.449(42)	238(9)	12.06(4)	1.302(45)	11.94(14)	8.68(30)	14.78(1.16)
z^{4+4}	1.285(58)	0.357(47)	261(30)	11.99(12)	1.416(173)	12.10(14)	9.54(1.04)	17.41(4.31)
$!z^{4+4}$	1.329(48)	0.465(24)	240(9)	12.06(3)	1.329(48)	11.83(19)	8.76(30)	15.07(1.14)

Table 6: Results for the form factors $G_X(0)$ at zero momentum transfer and for the mean squared radii $r_X^2 = -6G_X'(0)/G_X(0)$ obtained from fits using various form factor parametrizations. We also provide results for the pion-nucleon coupling $g_{\pi NN}$ and for the induced pseudoscalar coupling at the muon capture point $g_P^\star$, which can be directly compared to the experimental value $g_P^\star = 8.01(55)$ from muon capture [56, 57].

with the muon mass $m_\mu = 105.6\,\mathrm{MeV}$, and for the pion-nucleon coupling constant

$$g_{\pi NN} = \lim_{Q^2 \to -m_\pi^2} \frac{m_\pi^2 + Q^2}{4mF_\pi} G_{\tilde{P}}(Q^2) = \frac{m}{F_\pi}\tilde{P}(-m_\pi^2), \tag{6.34}$$

where we use the PDG value of $F_\pi = 92.07\,\mathrm{MeV}$ [119]. As a general trend we find that the fits which ensure that PCAC is satisfied in the continuum limit yield smaller statistical uncertainties. We find reasonable values for $g_P^\star$ that are in agreement with the approximate realization of PPD in nature. From table 6 one can actually read off that the different parametrizations yield compatible results, with the exception of the axial radius, where the dipole fits give significantly smaller values.

In our opinion, the parametrizations !2P and $!z^{4+3}$ yield the most reliable results (for the fits with more free parameters the chiral and continuum extrapolation is less stable). However, given our set of available data, we cannot decide whether the !2P or the $!z^{4+3}$ fit is better. We have therefore decided to perform an analysis of systematic uncertainties for both of these fits. In table 7 we provide, in addition to the statistical error $()_s$, estimates for the systematic uncertainties due to the quark mass extrapolation $()_m$ and the continuum extrapolation $()_a$. To this end, we have performed additional fits with cuts in the fit ranges ($\bar{m} < 450\,\mathrm{MeV}$ and $a < 0.08\,\mathrm{fm}$, respectively). We then take the difference between the results from these fits and our main result as an estimate of the corresponding systematic uncertainties. As discussed in section 5.3, our main analysis is performed using the fit ansatz with the energies of the nucleon-pion states fixed to the noninteracting value. To estimate the systematic uncertainty due to this choice, we have performed additional fits, where the energies for the nucleon-pion states are free

	!2P	$!z^{4+3}$
$G_A(0) = \frac{m_\ell}{m} G_P(0)$	$1.229(24)_s(6)_{ex}(3)_m(17)_a$	$1.302(45)_s(42)_{ex}(38)_m(46)_a$
$G_{\tilde{P}}(0)$	$226(5)_s(4)_{ex}(2)_m(2)_a$	$238(9)_s(5)_{ex}(7)_m(5)_a$
$r_A^2\,[\mathrm{fm}^2]$	$0.272(21)_s(6)_{ex}(7)_m(24)_a$	$0.449(42)_s(42)_{ex}(42)_m(49)_a$
$M_A\,[\mathrm{GeV}]$	$1.312(50)_s(15)_{ex}(16)_m(54)_a$	$1.020(50)_s(52)_{ex}(44)_m(52)_a$
$r_{\tilde{P}}^2\,[\mathrm{fm}^2]$	$11.91(2)_s(0)_{ex}(1)_m(2)_a$	$12.06(4)_s(3)_{ex}(4)_m(3)_a$
$r_P^2\,[\mathrm{fm}^2]$	$11.84(8)_s(24)_{ex}(6)_m(2)_a$	$11.94(14)_s(8)_{ex}(3)_m(12)_a$
$g_P^\star$	$8.30(17)_s(14)_{ex}(6)_m(8)_a$	$8.68(30)_s(18)_{ex}(23)_m(16)_a$
$g_{\pi NN}$	$12.93(55)_s(44)_{ex}(20)_m(32)_a$	$14.78(1.16)_s(72)_{ex}(98)_m(67)_a$
$\Delta_{\mathrm{GT}}\,[\%]$	$0.86(2.39)_s(3.71)_{ex}(1.21)_m(88)_a$	$6.53(4.26)_s(1.30)_{ex}(2.90)_m(53)_a$

Table 7: Results obtained from the !2P and the $!z^{4+3}$ fit including the statistical error $()_s$ and estimates of the systematic uncertainties due to quark mass extrapolation $()_m$, due to the continuum extrapolation $()_a$, and due to additional excited state effects $()_{ex}$. The systematics are specific to the particular fits and do not reflect differences between fitansätze. Since both fits satisfy PCAC in the continuum, $G_A(0) = \frac{m_\ell}{m} G_P(0)$ holds automatically.

fit parameters.[18] The $N\pi$ energies obtained from these fits are consistent with those presented in figure 13. The difference between our main result and the result obtained from this alternative fit is given as an estimate for the systematic uncertainty of our excited state analysis $()_{ex}$.

6.4. Discussion

Both the !2P and the $!z^{4+3}$ fit describe the data well (with similar values for the $\chi^2/d.o.f.$) and, as one can see in table 7, yield compatible results for almost all observables. For definiteness we choose to quote the values from the $!z^{4+3}$ fit as our final result in these cases, merely because it might have less parametrization bias and because the slightly larger statistical uncertainty is more conservative. In the case of the axial radius, which is directly linked to the axial dipole mass $M_A = \sqrt{12}/r_A$, however, we find that the dipole fit and the z-expansion yield significantly different results. Our main conclusion here has to be that r_A (and the small Q^2 behavior of the form factors in general, cf. figure 15) is highly parametrization dependent – a nuisance which also plagues determinations from experiment, cf. below. It is consistent that we also find a parametrization dependence of the axial coupling constant, where the value $g_A = 1.302(86)$ (z-exp) is higher than $g_A = 1.229(30)$ (dipole). In this case one can compare to the value from an analysis that

[18] In these fits, we did not allow for the contributions of additional generic excited states to the three-point functions. Keeping these, without fixing the $N\pi$ energies, turned out not to be feasible for the statistics presently available on most of our ensembles.

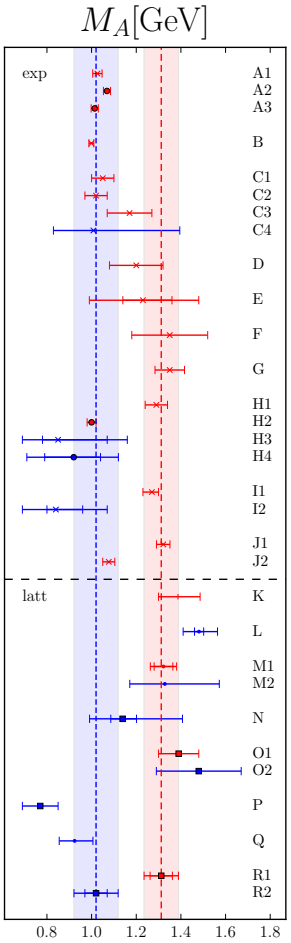

id	ref.	description
A	[62]	reanalysis of experimental data (year $\leq$ 1999)
A1		ν scattering; various targets; world avg. year $\leq$ 1990
A2		π electroproduction; world avg. year $\leq$ 1999
A3		π electroproduction; world avg. year $\leq$ 1999; HBChPT corrected
B	[120]	ν scattering; reanalysis of ANL, BNL, FNAL, CERN, and IHEP data; various targets; RFG model; dipole ansatz
C	[50]	reanalysis of ν scattering data
C1		BNL data [121]; dipole ansatz
C2		ANL data [122]; dipole ansatz
C3		FNAL data [123]; dipole ansatz
C4		combined analysis of BNL, ANL, and FNAL data; z-exp
D	[124]	ν scattering; K2K (SciFi); oxygen target; dipole ansatz
E	[125]	ν scattering; MINOS; iron target; dipole ansatz
F	[126]	ν scattering; MiniBooNE; carbon target; assuming RFG model; dipole ansatz
G	[127]	reanalysis of [126]; RFG model and spectral function model; dipole ansatz
H	[115]	reanalysis of MiniBooNE and π electroproduction data
H1		MiniBooNE data [126]; dipole ansatz
H2		π electroproduction data (from refs. [128–132]); dipole ansatz
H3		MiniBooNE data [126]; z-exp
H4		π electroproduction data (from refs. [128–132]); z-exp
I	[133]	analysis of MiniBooNE $\bar{\nu}$ scattering data [134]
I1		dipole ansatz
I2		z-exp
J	[135]	reanalysis of MiniBooNE data [126]
J1		LFG model; dipole ansatz
J2		LFG model + multi-nucleon reactions + RPA, etc., see [136]
K	[6]	$N_f = 2+1$ DWF; RBC/UKQCD; $a = 0.114$ fm
L	[26]	$N_f = 2+1$ Wilson (clover) fermions; $a = 0.114$ fm
M	[27]	$N_f = 2$ Wilson (clover) fermions; ETMC; $a = 0.0938$ fm
M1		dipole ansatz
M2		z-exp
N	[28]	$N_f = 2$ Wilson (clover) fermions; CE
O	[29]	$N_f = 2+1+1$ Wilson (clover-on-HISQ) fermions; PNDME; CE
O1		dipole ansatz
O2		z-exp
P	[34]	$N_f = 2$ Wilson (clover) fermions; RQCD; subtraction method; CE; z-exp
Q	[97]	$N_f = 2+1+1$ Wilson (clover-on-HISQ) fermions; PNDME; $a = 0.0871$ fm; takes into account $N\pi$ state; z-exp
R	[42]	**This work;** $N_f = 2+1$ Wilson (clover) fermions; RQCD; full resolution of $N\pi$ state; CE
R1		dipole ansatz
R2		z-exp

Figure 20: Compilation of results for the axial dipole mass M_A from experiment (A-J) and lattice simulations (K-R). Extractions based on a dipole ansatz are colored red, while those using any variant of the z-expansion are colored blue. The error bands show the results of our !2P (red) and our $!z^{4+3}$ (blue) fits, with all errors added in quadrature.
Symbols: crosses: ν scattering; circles: π electroproduction; tic: not continuum extrapolated; dot: single ensemble; square: continuum extrapolated.
Abbreviations: RFG: relativistic Fermi gas [137]; LFG: local Fermi gas; RPA: random phase approximation [138–140]; DWF: domain wall fermions; HISQ: highly improved staggered quarks; CE: continuum extrapolated.

only takes into account data at zero momentum transfer, which is in agreement with the result obtained from the dipole fit. Note, that this parametrization dependence of the form factors gradually disappears at increasing momentum transfer Q^2.

In figure 20 we show a compilation of experimental data and lattice data for the axial dipole mass. While the 20^{th} century world average (cf. ref. [62]) supports a value of

M_A around 1 GeV, newer experiments by K2K [124], MINOS [125], and, in particular, MiniBooNE [126, 134] yield larger values. This has fueled some discussions lately. One possible explanation is that the discrepancy is caused by nuclear effects. In ref. [135] it has been demonstrated that, using a local Fermi gas (LFG) model combined with multi-hadron interactions and the random phase approximation (RPA), one can recover smaller values for M_A from MiniBooNE data. As argued in ref. [141], larger values for M_A in MiniBooNE may also be a consequence of transverse enhancement due to meson exchange currents, cf. ref. [142].

Another line of inquiry is pursued, e.g., in refs. [50, 115, 133]. It is based on the suspicion that the dipole ansatz may be too restrictive. Using the z-expansion one finds smaller values and much larger errors for M_A. In ref. [115] it is shown that the MiniBooNE data is consistent with old π electroproduction data under these circumstances. Our analysis supports this picture. The results for the axial radii obtained from the dipole fit (!2P) and the z-expansion ($!z^{4+3}$) correspond to the axial pole masses of $M_A = 1.31(8)$ GeV (dipole) and $M_A = 1.02(10)$ GeV (z-exp). The situation we find is thus very similar to the one reported in ref. [115], where extractions using a dipole ansatz yield $M_A = 1.29(5)$ GeV (dipole, [115]), while the z-expansion yields a smaller value $M_A = (0.85^{+0.22}_{-0.07} \pm 0.09)$ GeV (z-exp, [115]), see also ref. [133]. It is notable that the z-expansion coefficients we obtain from our fits (see table 5) approximately satisfy the constraints that are imposed in ref. [115].

For the dipole ansatz our result is in good agreement with previous lattice determinations. In particular the agreement with the continuum extrapolated value from ref. [29] is encouraging. For the z-expansion the situation is not so clear, since the lattice results scatter over a wide range. In part this may be caused by the use of different variants of the z-expansion (number of parameters, use of priors, choice of t_0 in eq. (6.5), implementation of constraints, etc.).

In figure 21 we have compiled results for the induced pseudoscalar coupling at the muon capture point, $g_P^\star$, from experiment, ChPT, and lattice QCD. The ChPT predictions[19] are based on measurements of the axial radius and experimental data for $g_{\pi NN}$. They persistently call for a value slightly above 8. While older measurements of ordinary muon capture (OMC) were in agreement with this prediction (within large errors), the TRIUMF measurement [52, 53] lies significantly higher. It has to be seen as a success of BChPT that the new OMC measurement by MuCap [56, 57] is spot on with a small error. Independent of the choice of parametrization, our results are in agreement with both the ChPT prediction and the MuCap result. In particular, recent lattice results that include a chiral and a continuum extrapolation using ensembles with close to physical pion masses have yielded much smaller values. In retrospect, it is clear that these findings

[19] Heavy baryon ChPT actually reproduces the Adler–Dothan–Wolfenstein formula [144, 145], cf. ref. [62].

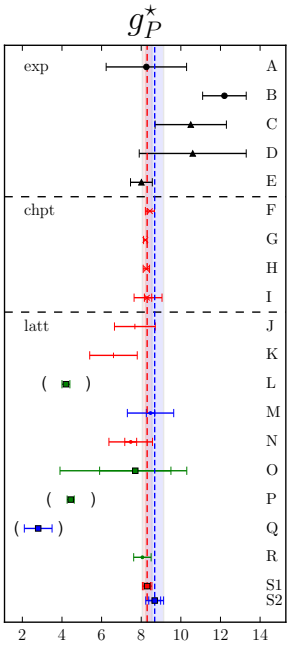

id	ref.	description
A	[51]	RMC on calcium; $g_P^\star = 6.5(1.6) g_A$; point in plot obtained by multiplying with $g_A = 1.27$
B	[52, 53]	RMC on hydrogen; TRIUMF; updated value from [54]
C	[54]	OMC world avg. (year ≤ 1981)
D	[55]	OMC in hydrogen; Saclay; updated value from [54]
E	[56, 57]	OMC in hydrogen gas; MuCap
F	[60]	HBChPT; M_A from ν scattering; assuming $g_{\pi NN} = 13.31$
G	[61]	HBChPT; M_A from π electroproduction [43, 131, 132]; assuming $g_{\pi NN} = 13.0$
H	[62]	HBChPT; M_A from ν scattering; assuming $g_{\pi NN} = 13.10$
I	[63]	covariant BChPT (EOMS); M_A from ν scattering; assuming $g_{\pi NN} = 13.21$ [143]
J	[4]	$N_f = 2$ DWF; $a = 0.116$ fm; dipole ansatz
K	[6]	$N_f = 2+1$ DWF; RBC/UKQCD; $a = 0.114$ fm; dipole ansatz
L	[14]	$N_f = 2$ Wilson (clover) fermions; RQCD; CE; EFT ansatz corrected by missing factor of 2
M	[26]	$N_f = 2+1$ Wilson (clover) fermions; $a = 0.114$ fm; z-exp
N	[27]	$N_f = 2$ Wilson (clover) fermions; ETMC; $a = 0.0938$ fm; dipole ansatz
O	[28]	$N_f = 2$ Wilson (clover) fermions; CE; EFT ansatz
P	[29]	$N_f = 2+1+1$ Wilson (clover-on-HISQ) fermions; PNDME; CE; EFT ansatz
Q	[34]	$N_f = 2$ Wilson (clover) fermions; RQCD; subtraction method; CE; z-exp
R	[97]	$N_f = 2+1+1$ Wilson (clover-on-HISQ) fermions; PNDME; $a = 0.0871$ fm; takes into account $N\pi$ state; z-exp
S	[42]	**This work;** $N_f = 2+1$ Wilson (clover) fermions; RQCD; full resolution of $N\pi$ state; CE
S1		dipole ansatz
S2		z-exp

Figure 21: Compilation of data for the pseudoscalar coupling at the muon capture point, g_P^*, from experiment (A-E), BChPT (F-I), and lattice simulations (J-S). Extractions based on a dipole ansatz are colored red, while those using any variant of the z-expansion are colored blue. Some lattice calculations use an EFT ansatz colored green (pion pole term combined with Taylor expansion). The error bands correspond to the result of our !2P (red) and our $!z^{4+3}$ (blue) fits, with all errors added in quadrature.
The lattice results in parentheses are outdated, since they are strongly affected by the pion pole enhanced excited states treated in this article, cf. also the discussion in ref. [97].
Symbols: circle: radiative muon capture; triangle: ordinary muon capture; tic: not continuum extrapolated; dot: single ensemble; square: continuum extrapolated.
Abbreviations: RMC: radiative muon capture; OMC: ordinary muon capture; HBChPT: heavy baryon ChPT; EOMS: extended on-mass-shell scheme; DWF: domain wall fermions; HISQ: highly improved staggered quarks; CE: continuum extrapolated.

were caused by the pion pole enhanced $N\pi$ excited state contribution, which was not fully under control. See also ref. [97], where the same conclusion has been drawn.

Results for the pion-nucleon coupling constant $g_{\pi NN}$ are collected in figure 22. The experimental results from πN scattering, NN scattering, and pionic atoms have reached a high precision, and ,in particular, recent determinations are in quite good agreement with each other. The discussion is now centering on the understanding of charge and

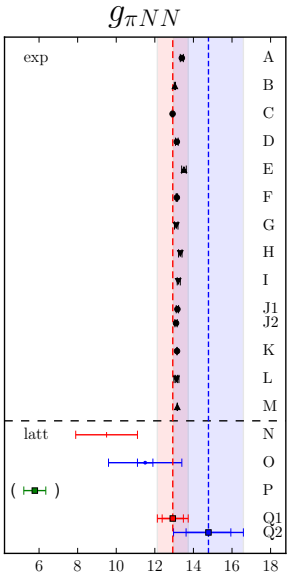

id	ref.	description
A	[146]	πN scattering; PWA
B	[147–149]	np, pp scattering; PWA
C	[150, 151]	πN scattering; PWA
D	[152]	πN scattering; PWA; GMO
E	[153]	np backward cross section
F	[154]	πN scattering; PWA; DR
G	[155]	$\pi^- p$ and $\pi^- d$ pionic atoms; GMO
H	[156]	$\pi^- p$ and $\pi^- d$ pionic atoms; GMO
I	[143]	$\pi^- p$ and $\pi^- d$ pionic atoms; GMO
J	[157]	πN scattering; DR;
J1		CERN data
J2		TRIUMF data
K	[158]	πN scattering; PWA; DR
L	[159–161]	$\pi^- p$ and $\pi^- d$ pionic atoms; GMO; including third-order ChPT corrections
M	[162]	np, pp scattering; PWA
N	[6]	$N_f = 2+1$ DWF; RBC/UKQCD; $a = 0.114$ fm; dipole ansatz
O	[26]	$N_f = 2+1$ Wilson (clover) fermions; $a = 0.114$ fm; z-exp
P	[29]	$N_f = 2+1+1$ Wilson (clover-on-HISQ) fermions; PNDME; CE; EFT ansatz
Q	[42]	**This work;** $N_f = 2+1$ Wilson (clover) fermions; RQCD; full resolution of $N\pi$ state; CE
Q1		dipole ansatz
Q2		z-exp

Figure 22: Compilation of data for the pion-nucleon coupling constant $g_{\pi NN}$ from experiment (A-M) and from lattice simulations (N-Q). We do not discriminate between charged and neutral pion-nucleon couplings here, which can be slightly different. In the lattice section we have only listed direct determinations, ignoring all results that are merely based on the Goldberger–Treiman relation [163]. Extractions based on a dipole ansatz are colored red, while those using any variant of the z-expansion are colored blue. Some lattice calculations use an EFT ansatz colored green (a pion pole term combined with a Taylor expansion). The error bands show the results of our !2P (red) and our $!z^{4+3}$ (blue) fits, with all errors added in quadrature. The lattice result in parentheses is outdated, cf. the discussion in ref. [97]. For a recent review, see ref. [164].
Symbols: circle: $N\pi$ scattering; triangle (up): NN scattering; triangle (down): pionic atoms; tic: not continuum extrapolated; dot: single ensemble; square: continuum extrapolated.
Abbreviations: PWA: partial wave analysis; GMO: Goldberger–Miyazawa–Oehme sum rule [165]; DR: dispersion relation; DWF: domain wall fermions; HISQ: highly improved staggered quarks; CE: continuum extrapolated.

isospin breaking effects (see, e.g., refs. [166, 167]) — a question that is out of reach of current lattice QCD analyses of nucleon structure, which usually ignore QED effects and use degenerate light quark masses. Also the experimental precision is not yet within reach.[20] However, a comparison of the lattice values with the experimental results and,

[20] There are a number of indirect estimates based on the Goldberger–Treiman relation, see, e.g., refs. [4, 6, 14, 27]. While such estimates can have quite small statistical errors and may serve as consistency checks, they should not be considered as independent measurements of $g_{\pi NN}$.

in particular, with the analysis of refs. [159–161], which includes higher order ChPT corrections and an estimate of systematic uncertainties, can serve as a consistency check. It is thus quite encouraging that our results for $g_{\pi NN}$ from both, the !2P and the $!z^{4+3}$ fit, are in agreement with these determinations. As one can see in table 7, a meaningful prediction of the Goldberger–Treiman discrepancy $\Delta_{\mathrm{GT}} = 1 - \frac{m g_A}{F_\pi g_{\pi NN}}$ is not possible with our current accuracy.

7. Summary and outlook

In this thesis we have presented a method that can control pion pole enhanced excited state contributions that occur in the axial and pseudoscalar channels. The technique is based on EFT considerations similar to refs. [92–96, 98, 99, 101], but simultaneously reduces the ChPT input. The EFT analysis presented in section 4 is mainly used to understand the general structure of the pole enhanced $N\pi$ contribution, which then can be taken into account explicitly in the spectral decomposition of the three-point functions, see section 4.4. The fits give amplitudes consistent with EFT expectations, however, we do not constrain these in the analysis. Our numerical analysis presented in section 5 demonstrates that, using our new technique, the ground state can be extracted reliably, even at small pion masses where the pole enhanced excited state constitutes (at currently available source-sink distances) the largest contribution in some channels.

We find that the nucleon form factors extracted at nonvanishing lattice spacings satisfy constraints from PCAC up to small deviations of roughly 5%, which can be attributed to discretization effects. We find the PPD assumption to be fulfilled to the same degree. Note, however, that the pion pole dominance assumption for the pseudoscalar form factors is only a (seemingly very good) estimate and is not expected to be satisfied exactly, even in the continuum. PCAC, however, *has* to hold exactly in the continuum. We leverage the latter information in our form factor analysis: in addition to the usual dipole ansatz and the z-expansion, we have derived (for both cases) parametrizations that are consistent with PCAC in the continuum, cf. section 6.2.3. The latter stabilize the continuum extrapolation considerably, without adding any parametrization bias.

Using a large set of CLS ensembles, we are able to take all the relevant limits (continuum limit, infinite volume limit, and extrapolation to physical quark masses) in a controlled fashion. To this end, we use generic extrapolation formulas (see section 6.2.4) for the parameters occurring in the form factor parametrization. The results at the physical point (in the continuum and for infinite volume) obtained from various form factor parametrizations are given in tables 5 and 6. Within present errors, our form factor data are well represented both by the dipole parametrization and by z-expansion fits. The final numbers, including estimates of systematic uncertainties due to the quark mass and the continuum extrapolation, can be taken from table 7. In figure 23 we show the results for the form factors. One can see that the deviations between the dipole fit and the z-expansion mainly affect the small Q^2 region, and gradually disappear at increasing momentum transfer Q^2. Files containing the data used to create this figure are included as supplementary material in the arXiv and journal version of [42].

In particular the slope of the axial form factor at zero momentum transfer, which is proportional to the axial radius (i.e., inversely proportional to the so-called axial mass),

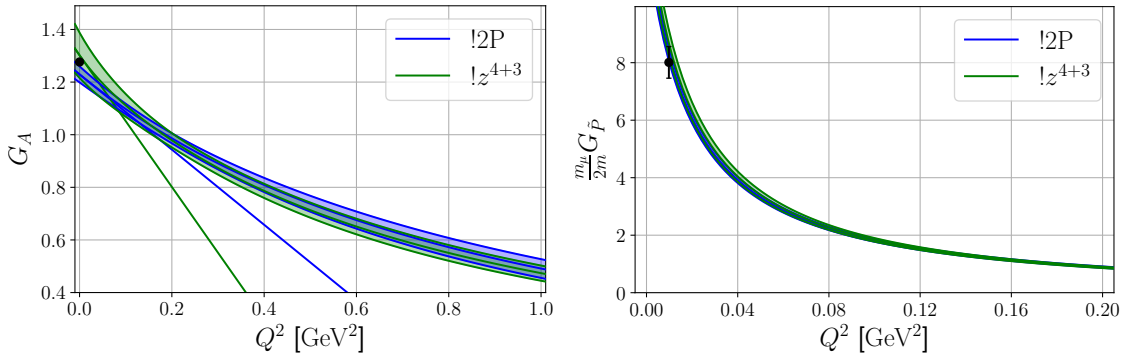

Figure 23: Results for the form factors obtained from the !2P (blue) and the $!z^{4+3}$ (green) fits. The bands show the statistical and systematic errors added in quadrature. The left panel shows the axial form factor $G_A(Q^2)$. At $Q^2 = 0$ the black circle indicates the experimental result for g_A [119] (see also refs. [38–41]), while the lines indicate the slope of the corresponding fit. On the right panel we plot the results for $\frac{m_\mu}{2m} G_{\tilde{P}}(Q^2)$, which can be compared to the experimental value for the induced pseudoscalar coupling $g_P^\star$ (cf. eq. (6.33)) from OMC [56, 57] (black circle).

exhibits a substantial parametrization dependence, as can be seen in figure 23. To reduce this ambiguity and to eventually rule out one of the parametrizations one would have to improve the resolution of the form factor in the region of small momentum transfer. This can be achieved by increasing the number of data points at very small values of Q^2 (one could also compute the derivative of the form factor at $Q^2 = 0$ [168, 169]) or by substantially reducing the errors of the data in this region.[21] Interestingly, the tendency of obtaining a larger radius from the z-expansion also applies to the analysis of experimental data, which do not cover the very low-Q^2 region well either. In fact both our z-expansion and our dipole fit results for the axial radius are in agreement with the respective findings from recent quasi-elastic (anti-)neutrino nucleon scattering data (MiniBooNE, [115, 133]), where the same parametrization bias has been reported. We emphasize that within the Q^2 regime that is of interest regarding terrestrial long baseline neutrino experiments the two parametrization of our data overlap within a fraction of a standard deviation so that both parametrizations can be used equally well for neutrino phenomenology. In contrast to most determinations from experiment (in particular the more precise ones), our method does not rely on any assumptions regarding nuclear effects. Therefore, the results can also be used to benchmark nuclear models.

In figure 19, we plot the ratios r_{PCAC} and r_{PPD} at the physical point, where deviations from unity correspond to a violation of PCAC and deviations from the PPD assumption,

[21] Certainly such data would be most helpful at small lattice spacings and at physical quark masses in order to control the necessary extrapolations.

respectively. In particular the fits with exact PCAC in the continuum (i.e., $r_{\mathrm{PCAC}} = 1$ automatically) allow us to draw conclusions with respect to the pion pole dominance ansatz for the pseudoscalar form factors. We find that our results are consistent with the PPD ansatz independent of the choice of parametrization of the form factor. The values we extract for the induced pseudoscalar coupling at the muon capture point are in good agreement with the experimental value obtained from muon capture [56, 57].

Using the frameworks we developed in this thesis we can study a variety of form factors on our ensembles in the future. For example, the isovector vector form factor may be contaminated by nucleon rho and nucleon two-pion states, which could be treated in a similar fashion as the nucleon pion states in section 4. This is especially interesting since the isovector anomalous magnetic moment $\tilde{g}_T$ of the nucleon, which requires the extrapolation of the induced tensor form factor to $Q^2 = 0$, tends to be slightly underestimated on the lattice compared to its experimental value, see ,e.g., refs. [14, 35, 109]. In this context also the electric and magnetic radii are interesting to study.

Additionally our group has developed high-performance code that is able to estimate the disconnected loops (cf. eq. (3.38)) using the techniques described in [170]. Using this code we are currently generating data for all our ensembles, cf. table 2, which will enable us to do a systematic analysis of singlet form factors similar to section 6.2.4. Since obtaining high precision for observables which include disconnected contributions is very challenging we aim for a determination of charges first, i.e., $Q^2 = 0$. In this context, interesting quantities are for example:

- The nucleon sigma terms σ_N^q for flavor q, or equivalently the quark mass fractions $f_{T_q} = \sigma_q/m$, which can be used to calculate the quark mass contributions to the nucleon mass [171]

$$m = \sum_q \sigma_q + E_{\mathrm{kin}} + E_{\mathrm{tr.a.}} \tag{7.1}$$

  where E_{kin} is the kinetic energy of quarks and gluons and $E_{\mathrm{tr.a.}}$ is the contribution that arises from the trace anomaly.

- The axial charges g_A^q for flavor q which are equivalent to the first Mellin moments of the polarized parton distribution function Δq of the nucleon. Using Ji's sum rule [172] the nucleon's total spin can be decomposed as

$$\frac{1}{2} = \sum_q \left(\frac{1}{2} \Delta q + L_q \right) + J_g, \tag{7.2}$$

  where L_q is the total orbital angular momentum of quarks with flavor q and J_g is the total angular momentum of the gluons.

For an overview of recent lattice calculations, see, e.g., the latest FLAG review [173].

A. Resampling

In order to obtain reliable error estimates for our ratios, we need to resample our bare two- and three-point functions. In this section we will briefly outline how to incorporate the reweighting into this. To this end we assume that A_i are measurements of an observable (such as $C_{2pt}(t)$) on each configuration $i \in \{0, 1, \ldots, N_{\text{conf.}} - 1\}$ where $N_{\text{conf.}}$ is the total number of configurations. The ω_i are the corresponding reweighting factors, which, for the CLS ensembles, are products of the reweighting factors that correspond to the twisted mass and the rational approximation, cf. sections 2.6.1 and 2.6.2.

The mean value is calculated as

$$\overline{A} = \frac{\sum_{i=0}^{N_{\text{conf.}}-1} \omega_i A_i}{\sum_{i=0}^{N_{\text{conf.}}-1} \omega_i}. \tag{A.1}$$

A.1. Binning

Before we address the actual resampling we will make a few comments on binning, which is used to minimize the correlations in the Monte Carlo time direction. We bin the data with a binsize of N_{bin} such that

$$N_{\text{conf.}}^{\text{binned}} = \left\lfloor \frac{N_{\text{conf.}}}{N_{\text{bin}}} \right\rfloor, \tag{A.2}$$

where $\lfloor \ldots \rfloor$ is the floor function.

The binned measurements and reweighting factors are then given as

$$A_j^{\text{binned}} = \frac{\sum_{k=jN_{\text{bin}}}^{(j+1)N_{\text{bin}}-1} \omega_k A_k}{\sum_{k=jN_{\text{bin}}}^{(j+1)N_{\text{bin}}-1} \omega_k}, \qquad \omega_j^{\text{binned}} = \sum_{k=jN_{\text{bin}}}^{(j+1)N_{\text{bin}}-1} \omega_k, \tag{A.3}$$

where $j \in \{0, 1, \ldots, N_{\text{conf.}}^{\text{binned}} - 1\}$. One can easily verify that

$$\overline{A}^{\text{binned}} \equiv \frac{\sum_{j=0}^{N_{\text{conf.}}^{\text{binned}}-1} \omega_j^{\text{binned}} A_j^{\text{binned}}}{\sum_{j=0}^{N_{\text{conf.}}^{\text{binned}}-1} \omega_j^{\text{binned}}} = \overline{A}, \tag{A.4}$$

if $N_{\text{conf.}}^{\text{binned}} \cdot N_{\text{bin}} = N_{\text{conf.}}$. Since the resampling is identical for both binned and unbinned

measurements we will drop the superscript in the following sections.

A.2. Jackknife

In jackknife resampling we create jackknife samples by dropping a single measurement each. Thus for all i the samples are given as

$$A_i^{\text{jack}} = \frac{\sum\limits_{j\neq i} \omega_j A_j}{\sum\limits_{j\neq i} \omega_j} \equiv \frac{\sum\limits_{j} \omega_j A_j - \omega_i A_i}{\sum\limits_{j} \omega_j - \omega_i}. \tag{A.5}$$

The distribution of the jackknife samples is much narrower than the original distribution and the error can be calculated via

$$\sigma_A^{\text{jack}} = \sqrt{\frac{N_{\text{conf.}} - 1}{N_{\text{conf.}}} \sum_i \left(A_i^{\text{jack}} - \overline{A}^{\text{jack}}\right)^2}. \tag{A.6}$$

With this method we can obtain reliable errors, however we would require additional tricks to combine different ensembles, since the number of jackknife samples is identical to the number of configurations and ensembles usually have different $N_{\text{conf.}}$.

A.3. Bootstrap

In bootstrap resampling we can freely choose the number of samples N_{boot}. This is advantageous since we can simply use the same number of samples on all ensembles which is straight forward to combine afterwards. For each of the sample we randomly take $N_{\text{conf.}}$ measurements, i.e.,

$$A_j^{\text{boot}} = \frac{\sum\limits_{k\in\Phi_j} \omega_k A_k}{\sum\limits_{k\in\Phi_j} \omega_k}, \tag{A.7}$$

where Φ_j is the set of configurations for the j-th sample. A rule of thumb is $N_{\text{boot}} \geq 2N_{\text{conf.}}^{(\text{binned})}$ such that the original distribution of the A_i is roughly reproduced.

Within bootstrap, the statistical error is determined via

$$\sigma_A^{\text{boot}} = \sqrt{\frac{1}{N_{\text{boot}} - 1} \sum_i \left(A_i^{\text{boot}} - \overline{A}^{\text{boot}}\right)^2}. \tag{A.8}$$

Alternatively one can derive asymmetric errors from the distribution (histogram) of the samples. The lower (upper) error is then defined by the smallest (biggest) cutoff where 15.87% of the samples are below (above). This approach is less sensitive to outlying

samples than the traditional symmetric error and was used in this thesis in figures 16, 17, and 18.

B. Traces

Note that in this section we use Minkowsky conventione in order to be consistent with chapter 4. For the ground state contributions defined in eq. (4.28) one finds

$$B^{\vec{p}',\vec{p}}_{P^i_+,\mathcal{A}^\mu} = 2G_A\big(p'^i p^\mu + p^i p'^\mu + m(p'+p)^i g^{\mu 0} - g^{i\mu}(m^2 + mE' + mE + p'\cdot p)\big) + 2G_{\tilde{P}}\frac{q^\mu}{2m}\big((m+E')p^i - (m+E)p'^i\big), \tag{B.1}$$

$$B^{\vec{p}',\vec{p}}_{P^i_+,\mathcal{P}} = 2G_P\big((m+E')p^i - (m+E)p'^i\big). \tag{B.2}$$

Evaluating these equations for the 4 particular cases depicted in the rows of figure 4, where $\vec{p}' = \vec{0}$ and $\vec{p} = -\vec{q} = (0,0,p)^T$ with $p = \frac{2\pi}{L}$, yields

$$\text{row 1:}\quad 4m(E+m)G_A, \tag{B.3}$$

$$\text{row 2:}\quad (E+m)\big(4mG_A - 2(E-m)G_{\tilde{P}}\big), \tag{B.4}$$

$$\text{row 3:}\quad p\big(4mG_A - 2(E-m)G_{\tilde{P}}\big), \tag{B.5}$$

$$\text{row 4:}\quad 4mpG_P. \tag{B.6}$$

For the remaining traces that are needed for the determination of the parametrizations given in section 4.4 one gets

$$\mathrm{Tr}\big\{P^i_+(\not{p}+m)\not{r}_+\gamma_5(\not{p}+m)\big\} = 4\big(p^i(mE_\pi + p\cdot r_+) - mr^i_+(m+E)\big), \tag{B.7}$$

$$\mathrm{Tr}\big\{P^i_+(\not{p}'+m)\not{r}_-\gamma_5(\not{p}'+m)\big\} = 4\big(p'^i(mE_\pi + p'\cdot r_-) - mr^i_-(m+E')\big), \tag{B.8}$$

$$\mathrm{Tr}\big\{P^i_+\gamma_5(\not{p}+m)\big\} = +2p^i, \tag{B.9}$$

$$\mathrm{Tr}\big\{P^i_+(\not{p}'+m)\gamma_5\big\} = -2p'^i. \tag{B.10}$$

C. Fit ansatz for the subtracted currents

For the subtracted correlation functions defined in ref. [34], instead of the usual currents one inserts

$$\mathcal{A}^\mu_\perp = \left(g^{\mu\nu} - \frac{\bar{p}^\mu\bar{p}^\nu}{\bar{p}^2}\right)\mathcal{A}_\nu, \qquad \mathcal{P}_\perp = \mathcal{P} - \frac{1}{2i\,m_\ell}\frac{\bar{p}^\mu\bar{p}^\nu}{\bar{p}^2}\partial_\mu\mathcal{A}_\nu\,, \tag{C.1}$$

where $\bar{p} = (p'+p)/2$. By construction, this does not change the ground state contribution at all. In contrast, the excited state contributions are affected very strongly. Therefore,

the fit ansatz given in eqs. (4.29) and (4.30) has to be adapted to this case. Following the same steps as discussed in detail for the standard currents in section 4.29, we find

$$\begin{aligned} C^{\vec{p}',\vec{p},\mathcal{A}^\mu_\perp}_{\text{3pt},P^i_+} &= \frac{\sqrt{Z'}\sqrt{Z}}{2E'2E} e^{-E'(t-\tau)} e^{-E\tau} \\ &\quad \times \Bigg[B^{\vec{p}',\vec{p}}_{P^i_+,\mathcal{A}^\mu} \Bigg(1 + B_{10} e^{-\Delta E'(t-\tau)} + B_{01} e^{-\Delta E\tau} + B_{11} e^{-\Delta E'(t-\tau)} e^{-\Delta E\tau} \Bigg) \\ &\qquad + e^{-\Delta E'_{N\pi}(t-\tau)} \frac{E'}{E_\pi} \Bigg(r^\mu_+ - \bar{p}^\mu \frac{\bar{p}\cdot r_+}{\bar{p}^2} \Bigg) \Bigg(c' p^i + d' q^i \Bigg) \\ &\qquad + e^{-\Delta E_{N\pi}\tau} \frac{E}{E_\pi} \Bigg(r^\mu_- - \bar{p}^\mu \frac{\bar{p}\cdot r_-}{\bar{p}^2} \Bigg) \Bigg(c p'^i + d q^i \Bigg) \Bigg], \end{aligned} \tag{C.2}$$

$$\begin{aligned} C^{\vec{p}',\vec{p},\mathcal{P}_\perp}_{\text{3pt},P^i_+} &= \frac{\sqrt{Z'}\sqrt{Z}}{2E'2E} e^{-E'(t-\tau)} e^{-E\tau} \\ &\quad \times \Bigg[B^{\vec{p}',\vec{p}}_{P^i_+,\mathcal{P}} \Bigg(1 + B_{10} e^{-\Delta E'(t-\tau)} + B_{01} e^{-\Delta E\tau} + B_{11} e^{-\Delta E'(t-\tau)} e^{-\Delta E\tau} \Bigg) \\ &\qquad + e^{-\Delta E'_{N\pi}(t-\tau)} \frac{E'}{E_\pi} \frac{1}{2m_\ell} \Bigg(m^2_\pi - \frac{(\bar{p}\cdot r_+)^2}{\bar{p}^2} \Bigg) \Bigg(c' p^i + d' q^i \Bigg) \\ &\qquad - e^{-\Delta E_{N\pi}\tau} \frac{E}{E_\pi} \frac{1}{2m_\ell} \Bigg(m^2_\pi - \frac{(\bar{p}\cdot r_-)^2}{\bar{p}^2} \Bigg) \Bigg(c p'^i + d\, q^i \Bigg) \Bigg]. \end{aligned} \tag{C.3}$$

Similar to the situation with unsubtracted correlation functions, the parametrization simplifies for the particular kinematics we are using in our numerical analysis ($\vec{p}' = \vec{0}$ such that $\vec{q} = -\vec{p}$).

Acknowledgements

First I want to express my gratitude to my supervisor A. Schäfer who always encouraged my research and made this work possible in the first place. Additionally I am grateful to G. Bali and S. Collins who provided physical and technical insights into all aspects of my analysis.

I also want to thank my office mates S. Bürger, F. Hutzler, M. Gruber, D. Jenkins, and P. Wein for the comfortable and humorous working environment they created. In particular I wish to emphasize the close collaboration with M. Gruber and P. Wein, during which they introduced me to the effective field theory and motivated my analysis. Furthermore I want to acknowledge fruitful discussions I had with M. Löffler, R. Rödl, M. Schlemmer, and S. Weishäupl. This thesis was proofread by L. Barca, M. Gruber, D. Jenkins, S. Weishäupl, and P. Wein, for which I am much obliged.

Finally I want to thank the most important person to me, my beloved girlfriend Steffi, for her never ending support in all situations during my years of research.

References

[1] ATLAS collaboration, G. Aad et al., *Observation of a new particle in the search for the Standard Model Higgs boson with the ATLAS detector at the LHC*, *Phys. Lett.* **B716** (2012) 1 [1207.7214].

[2] J. Woithe, G. J. Wiener and F. F. Van der Veken, *Let's have a coffee with the Standard Model of particle physics!*, *Phys. Educ.* **52** (2017) 034001.

[3] G. Martinelli and C. T. Sachrajda, *A lattice study of nucleon structure*, *Nucl. Phys.* **B316** (1989) 355.

[4] H.-W. Lin, T. Blum, S. Ohta, S. Sasaki and T. Yamazaki, *Nucleon structure with two flavors of dynamical domain-wall fermions*, *Phys. Rev.* **D78** (2008) 014505 [0802.0863].

[5] RBC/UKQCD collaboration, T. Yamazaki, Y. Aoki, T. Blum, H. W. Lin, M. F. Lin, S. Ohta, S. Sasaki, R. J. Tweedie and J. M. Zanotti, *Nucleon Axial Charge in (2+1)-Flavor Dynamical-Lattice QCD with Domain-Wall Fermions*, *Phys. Rev. Lett.* **100** (2008) 171602 [0801.4016].

[6] T. Yamazaki, Y. Aoki, T. Blum, H.-W. Lin, S. Ohta, S. Sasaki, R. Tweedie and J. Zanotti, *Nucleon form factors with 2+1 flavor dynamical domain-wall fermions*, *Phys. Rev.* **D79** (2009) 114505 [0904.2039].

[7] LHPC collaboration, J. D. Bratt et al., *Nucleon structure from mixed action calculations using 2+1 flavors of asqtad sea and domain wall valence fermions*, *Phys. Rev.* **D82** (2010) 094502 [1001.3620].

[8] C. Alexandrou, M. Brinet, J. Carbonell, M. Constantinou, P. A. Harraud, P. Guichon, K. Jansen, T. Korzec and M. Papinutto, *Axial nucleon form factors from lattice QCD*, *Phys. Rev.* **D83** (2011) 045010 [1012.0857].

[9] S. Capitani, M. Della Morte, G. von Hippel, B. Jäger, A. Jüttner, B. Knippschild, H. B. Meyer and H. Wittig, *Nucleon axial charge from lattice QCD with controlled errors*, *Phys. Rev.* **D86** (2012) 074502 [1205.0180].

[10] J. R. Green, M. Engelhardt, S. Krieg, J. W. Negele, A. V. Pochinsky and S. N. Syritsyn, *Nucleon structure from Lattice QCD using a nearly physical pion mass*, *Phys. Lett.* **B734** (2014) 290 [1209.1687].

[11] R. Horsley, Y. Nakamura, A. Nobile, P. E. L. Rakow, G. Schierholz and J. M. Zanotti, *Nucleon axial charge and pion decay constant from two-flavor lattice QCD*, *Phys. Lett.* **B732** (2014) 41 [1302.2233].

[12] PNDME collaboration, T. Bhattacharya, S. D. Cohen, R. Gupta, A. Joseph, H.-W. Lin and B. Yoon, *Nucleon charges and electromagnetic form factors from 2+1+1-flavor lattice QCD*, *Phys. Rev.* **D89** (2014) 094502 [1306.5435].

[13] CSSM/QCDSF/UKQCD collaboration, A. J. Chambers et al., *Feynman-Hellmann approach to the spin structure of hadrons*, *Phys. Rev.* **D90** (2014) 014510 [1405.3019].

[14] G. S. Bali, S. Collins, B. Gläßle, M. Göckeler, J. Najjar, R. H. Rödl, A. Schäfer, R. W. Schiel, W. Söldner and A. Sternbeck, *Nucleon isovector couplings from $N_f = 2$ lattice QCD*, *Phys. Rev.* **D91** (2015) 054501 [1412.7336].

[15] G. von Hippel, T. D. Rae, E. Shintani and H. Wittig, *Nucleon matrix elements from lattice QCD with all-mode-averaging and a domain-decomposed solver: An exploratory study*, *Nucl. Phys.* **B914** (2017) 138 [1605.00564].

[16] PNDME collaboration, T. Bhattacharya, V. Cirigliano, S. D. Cohen, R. Gupta, H.-W. Lin and B. Yoon, *Axial, scalar, and tensor charges of the nucleon from 2+1+1-flavor Lattice QCD*, *Phys. Rev.* **D94** (2016) 054508 [1606.07049].

[17] A. S. Meyer, R. J. Hill, A. S. Kronfeld, R. Li and J. N. Simone, *Calculation of the Nucleon Axial Form Factor Using Staggered Lattice QCD*, *PoS* **LATTICE2016** (2017) 179 [1610.04593].

[18] B. Yoon et al., *Isovector charges of the nucleon from 2+1-flavor QCD with clover fermions*, *Phys. Rev.* **D95** (2017) 074508 [1611.07452].

[19] J. Liang, Y.-B. Yang, K.-F. Liu, A. Alexandru, T. Draper and R. S. Sufian, *Lattice Calculation of Nucleon Isovector Axial Charge with Improved Currents*, *Phys. Rev.* **D96** (2017) 034519 [1612.04388].

[20] C. Bouchard, C. C. Chang, T. Kurth, K. Orginos and A. Walker-Loud, *On the Feynman-Hellmann theorem in quantum field theory and the calculation of matrix elements*, *Phys. Rev.* **D96** (2017) 014504 [1612.06963].

[21] C. Alexandrou, M. Constantinou, K. Hadjiyiannakou, K. Jansen, C. Kallidonis, G. Koutsou, K. Ottnad and A. Vaquero, *Nucleon electromagnetic and axial form factors with N_f=2 twisted mass fermions at the physical point*, *PoS* **LATTICE2016** (2017) 154 [1702.00984].

[22] E. Berkowitz et al., *An accurate calculation of the nucleon axial charge with lattice QCD*, 1704.01114.

[23] D.-L. Yao, L. Alvarez-Ruso and M. J. Vicente-Vacas, *Extraction of nucleon axial charge and radius from lattice QCD results using baryon chiral perturbation theory*, *Phys. Rev.* **D96** (2017) 116022 [1708.08776].

[24] C. C. Chang et al., *A per-cent-level determination of the nucleon axial coupling from quantum chromodynamics*, *Nature* **558** (2018) 91 [1805.12130].

[25] C. Alexandrou, M. Constantinou, K. Hadjiyiannakou, K. Jansen, C. Kallidonis, G. Koutsou and A. Vaquero Avilés-Casco, *Connected and disconnected contributions to nucleon axial form factors using $N_f = 2$ twisted mass fermions at the physical point*, *EPJ Web Conf.* **175** (2018) 06003 [1807.11203].

[26] J. Green, N. Hasan, S. Meinel, M. Engelhardt, S. Krieg, J. Laeuchli, J. Negele, K. Orginos, A. Pochinsky and S. Syritsyn, *Up, down, and strange nucleon axial form factors from lattice QCD*, *Phys. Rev.* **D95** (2017) 114502 [1703.06703].

[27] C. Alexandrou, M. Constantinou, K. Hadjiyiannakou, K. Jansen, C. Kallidonis, G. Koutsou and A. Vaquero Avilés-Casco, *Nucleon axial form factors using $N_f = 2$ twisted mass fermions with a physical value of the pion mass*, *Phys. Rev.* **D96** (2017) 054507 [1705.03399].

[28] S. Capitani, M. Della Morte, D. Djukanovic, G. M. von Hippel, J. Hua, B. Jäger, P. M. Junnarkar, H. B. Meyer, T. D. Rae and H. Wittig, *Iso-vector axial form factors of the nucleon in two-flavour lattice QCD*, *Int. J. Mod. Phys.* **A34** (2019) 1950009 [1705.06186].

[29] PNDME collaboration, R. Gupta, Y.-C. Jang, H.-W. Lin, B. Yoon and T. Bhattacharya, *Axial-vector form factors of the nucleon from lattice QCD*, *Phys. Rev.* **D96** (2017) 114503 [1705.06834].

[30] PACS collaboration, N. Tsukamoto, K.-I. Ishikawa, Y. Kuramashi, S. Sasaki and T. Yamazaki, *Nucleon structure from 2+1 flavor lattice QCD near the physical point*, *EPJ Web Conf.* **175** (2018) 06007 [1710.10782].

[31] Y.-C. Jang, T. Bhattacharya, R. Gupta, H.-W. Lin and B. Yoon, *Nucleon Axial and Electromagnetic Form Factors*, *EPJ Web Conf.* **175** (2018) 06033 [1801.01635].

[32] PACS collaboration, K.-I. Ishikawa, Y. Kuramashi, S. Sasaki, N. Tsukamoto, A. Ukawa and T. Yamazaki, *Nucleon form factors on a large volume lattice near the physical point in 2+1 flavor QCD*, *Phys. Rev.* **D98** (2018) 074510 [1807.03974].

[33] χQCD collaboration, J. Liang, Y.-B. Yang, T. Draper, M. Gong and K.-F. Liu, *Quark spins and anomalous Ward identity*, *Phys. Rev.* **D98** (2018) 074505 [1806.08366].

[34] G. S. Bali, S. Collins, M. Gruber, A. Schäfer, P. Wein and T. Wurm, *Solving the PCAC puzzle for nucleon axial and pseudoscalar form factors*, *Phys. Lett.* **B789** (2019) 666 [1810.05569].

[35] E. Shintani, K.-I. Ishikawa, Y. Kuramashi, S. Sasaki and T. Yamazaki, *Nucleon form factors and root-mean-square radii on a* $(10.8\,\mathrm{fm})^4$ *lattice at the physical point*, *Phys. Rev.* **D99** (2019) 014510 [1811.07292].

[36] PNDME collaboration, Y.-C. Jang, T. Bhattacharya, R. Gupta, H.-W. Lin and B. Yoon, *Updates on Nucleon Form Factors from Clover-on-HISQ Lattice Formulation*, *PoS* **LATTICE2018** (2019) 123 [1901.00060].

[37] J. R. Green, M. Engelhardt, N. Hasan, S. Krieg, S. Meinel, J. W. Negele, A. V. Pochinsky and S. N. Syritsyn, *Excited-state effects in nucleon structure on the lattice using hybrid interpolators*, *Phys. Rev.* **D100** (2019) 074510 [1907.11950].

[38] UCNA collaboration, M. A.-P. Brown et al., *New result for the neutron β-asymmetry parameter A_0 from UCNA*, *Phys. Rev.* **C97** (2018) 035505 [1712.00884].

[39] B. Märkisch et al., *Measurement of the Weak Axial-Vector Coupling Constant in the Decay of Free Neutrons Using a Pulsed Cold Neutron Beam*, *Phys. Rev. Lett.* **122** (2019) 242501 [1812.04666].

[40] M. González-Alonso, O. Naviliat-Cuncic and N. Severijns, *New physics searches in nuclear and neutron β decay*, *Prog. Part. Nucl. Phys.* **104** (2019) 165 [1803.08732].

[41] L. Hayen and N. Severijns, *Radiative corrections to Gamow-Teller decays*, 1906.09870.

[42] RQCD collaboration, G. S. Bali, L. Barca, S. Collins, M. Gruber, M. Löffler, A. Schäfer, W. Söldner, P. Wein, S. Weishäupl and T. Wurm, *Nucleon axial structure from lattice QCD*, *JHEP* **05** (2020) 126 [1911.13150].

[43] S. Choi et al., *Axial and Pseudoscalar Nucleon Form Factors from Low Energy Pion Electroproduction*, *Phys. Rev. Lett.* **71** (1993) 3927.

[44] V. Bernard, U.-G. Meißner and N. Kaiser, *Comment on 'Axial and Pseudoscalar Nucleon Form Factors from Low Energy Pion Electroproduction'*, *Phys. Rev. Lett.* **72** (1994) 2810.

[45] A. Liesenfeld et al., *A measurement of the axial form factor of the nucleon by the $p(e, e'\pi^+)n$ reaction at W = 1125 MeV*, *Phys. Lett.* **B468** (1999) 20 [nucl-ex/9911003].

[46] T. Fuchs and S. Scherer, *Pion electroproduction, partially conserved axial-vector current, chiral Ward identities, and the axial form factor revisited*, *Phys. Rev.* **C68** (2003) 055501 [nucl-th/0303002].

[47] L. A. Ahrens et al., *A study of the axial-vector form factor and second-class currents in antineutrino quasielastic scattering*, *Phys. Lett.* **B202** (1988) 284.

[48] T. Kitagaki et al., *Study of $\nu d \to \mu^- pp_s$ and $\nu d \to \mu^- \Delta^{++}(1232)n_s$ using the BNL 7-foot deuterium-filled bubble chamber*, *Phys. Rev.* **D42** (1990) 1331.

[49] A. Bodek, S. Avvakumov, R. Bradford and H. Budd, *Extraction of the Axial Nucleon Form Factor from Neutrino Experiments on Deuterium*, *J. Phys. Conf. Ser.* **110** (2008) 082004 [0709.3538].

[50] A. S. Meyer, M. Betancourt, R. Gran and R. J. Hill, *Deuterium target data for precision neutrino-nucleus cross sections*, *Phys. Rev.* **D93** (2016) 113015 [1603.03048].

[51] R. D. Hart, C. R. Cox, G. W. Dodson, M. Eckhause, J. R. Kane, M. S. Pandey, A. M. Rushton, R. T. Siegel and R. E. Welsh, *Radiative Muon Capture in Calcium*, *Phys. Rev. Lett.* **39** (1977) 399.

[52] G. Jonkmans et al., *Radiative Muon Capture on Hydrogen and the Induced Pseudoscalar Coupling*, *Phys. Rev. Lett.* **77** (1996) 4512 [nucl-ex/9608005].

[53] D. H. Wright et al., *Measurement of the induced pseudoscalar coupling using radiative muon capture on hydrogen*, *Phys. Rev.* **C57** (1998) 373.

[54] T. Gorringe and H. W. Fearing, *Induced pseudoscalar coupling of the proton weak interaction*, *Rev. Mod. Phys.* **76** (2004) 31 [nucl-th/0206039].

[55] G. Bardin, J. Duclos, A. Magnon, J. Martino, A. Richter, E. Zavattini, A. Bertin, M. Piccinini, A. Vitale and D. F. Measday, *A novel measurement of the muon capture rate in liquid hydrogen by the lifetime technique*, *Nucl. Phys.* **A352** (1981) 365.

[56] MuCap collaboration, V. A. Andreev et al., *Measurement of Muon Capture on the Proton to 1% Precision and Determination of the Pseudoscalar Coupling g_P*, *Phys. Rev. Lett.* **110** (2013) 012504 [1210.6545].

[57] MuCap collaboration, V. A. Andreev et al., *Measurement of the formation rate of muonic hydrogen molecules*, *Phys. Rev.* **C91** (2015) 055502 [1502.00913].

[58] P. Winter, *Muon capture on the proton*, *AIP Conf. Proc.* **1441** (2012) 537 [1110.5090].

[59] R. J. Hill, P. Kammel, W. J. Marciano and A. Sirlin, *Nucleon axial radius and muonic hydrogen — a new analysis and review*, *Rep. Prog. Phys.* **81** (2018) 096301 [1708.08462].

[60] V. Bernard, N. Kaiser and U.-G. Meissner, *QCD accurately predicts the induced pseudoscalar coupling constant*, *Phys. Rev.* **D50** (1994) 6899 [hep-ph/9403351].

[61] H. W. Fearing, R. Lewis, N. Mobed and S. Scherer, *Muon capture by a proton in heavy baryon chiral perturbation theory*, *Phys. Rev.* **D56** (1997) 1783 [hep-ph/9702394].

[62] V. Bernard, L. Elouadrhiri and U.-G. Meißner, *Axial structure of the nucleon*, *J. Phys.* **G28** (2002) R1 [hep-ph/0107088].

[63] M. R. Schindler, T. Fuchs, J. Gegelia and S. Scherer, *Axial, induced pseudoscalar, and pion-nucleon form factors in manifestly Lorentz-invariant chiral perturbation theory*, *Phys. Rev.* **C75** (2007) 025202 [nucl-th/0611083].

[64] C. Gattringer and C. B. Lang, *Quantum chromodynamics on the lattice*, vol. 788. Springer, Berlin, 2010, 10.1007/978-3-642-01850-3.

[65] J. S. S. Najjar, *Nucleon structure from stochastic estimators*, Ph.D. thesis, Universität Regensburg, 2014.

[66] K. G. Wilson, *Confinement of quarks*, *Phys. Rev.* **D10** (1974) 2445.

[67] K. Symanzik, *Continuum Limit and Improved Action in Lattice Theories. 1. Principles and ϕ^4 theory*, *Nucl. Phys.* **B226** (1983) 187.

[68] K. Symanzik, *Continuum Limit and Improved Action in Lattice Theories. 2. O(N) Non-linear sigma model in perturbation theory*, *Nucl. Phys.* **B226** (1983) 205.

[69] B. Sheikholeslami and R. Wohlert, *Improved Continuum Limit Lattice Action for QCD with Wilson Fermions*, *Nucl. Phys.* **B259** (1985) 572.

[70] J. Bulava and S. Schaefer, *Improvement of $N_f = 3$ lattice QCD with Wilson fermions and tree-level improved gauge action*, *Nucl. Phys. B* **874** (2013) 188 [1304.7093].

[71] M. Lüscher and P. Weisz, *On-Shell Improved Lattice Gauge Theories*, *Commun. Math. Phys.* **97** (1985) 59 [Erratum: *Commun. Math. Phys.* **98** (1985) 433].

[72] M. Lüscher and F. Palombi, *Fluctuations and reweighting of the quark determinant on large lattices*, *PoS* **LATTICE2008** (2008) 049 [0810.0946].

[73] M. Bruno et al., *Simulation of QCD with $N_f = 2 + 1$ flavors of non-perturbatively improved Wilson fermions*, *JHEP* **02** (2015) 043 [1411.3982].

[74] T. A. DeGrand, *A Conditioning Technique for Matrix Inversion for Wilson Fermions*, *Comput. Phys. Commun.* **52** (1988) 161.

[75] D. Mohler and S. Schaefer, *Remarks on strange-quark simulations with Wilson fermions*, *Phys. Rev.* **D102** (2020) 074506 [2003.13359].

[76] M. Lüscher and S. Schaefer, *Lattice QCD with open boundary conditions and twisted-mass reweighting*, *Comput. Phys. Commun.* **184** (2013) 519 [1206.2809].

[77] M. Lüscher and S. Schaefer, *Lattice QCD without topology barriers*, *JHEP* **07** (2011) 036 [1105.4749].

[78] M. Lüscher, *Properties and uses of the Wilson flow in lattice QCD*, *JHEP* **08** (2010) 071 [1006.4518], [Erratum: *JHEP* **03** (2014) 092].

[79] G. S. Bali et al., *Scale setting and the light hadron spectrum in $N_f = 2 + 1$ QCD with Wilson fermions*, in preparation.

[80] ALPHA collaboration, M. Bruno et al., *QCD Coupling from a Nonperturbative Determination of the Three-Flavor Λ Parameter*, *Phys. Rev. Lett.* **119** (2017) 102001 [1706.03821].

[81] S. Güsken, *A study of smearing techniques for hadron correlation functions*, *Nucl. Phys. B (Proc. Suppl.)* **17** (1990) 361.

[82] S. Güsken, U. Löw, K.-H. Mütter, R. Sommer, A. Patel and K. Schilling, *Non-singlet Axial Vector Couplings of the Baryon Octet in Lattice QCD*, *Phys. Lett.* **B227** (1989) 266.

[83] M. Falcioni, M. L. Paciello, G. Parisi and B. Taglienti, *Again on SU(3) glueball mass*, *Nucl. Phys.* **B251** (1985) 624.

[84] G. S. Bali, S. Collins and C. Ehmann, *Charmonium spectroscopy and mixing with light quark and open charm states from n_F=2 lattice QCD*, *Phys. Rev.* **D84** (2011) 094506 [1110.2381].

[85] ALPHA collaboration, J. Bulava, M. Della Morte, J. Heitger and C. Wittemeier, *Non-perturbative improvement of the axial current in $N_f = 3$ lattice QCD with Wilson fermions and tree-level improved gauge action*, *Nucl. Phys.* **B896** (2015) 555 [1502.04999].

[86] G. S. Bali, S. Collins, B. Gläßle, S. Heybrock, P. Korcyl, M. Löffler, R. Rödl and A. Schäfer, *Baryonic and mesonic 3-point functions with open spin indices*, *EPJ Web Conf.* **175** (2018) 06014 [1711.02384].

[87] G. S. Bali, S. Collins, P. Korcyl, R. Rödl, S. Weishäupl and T. Wurm, *Hyperon couplings from $N_f = 2 + 1$ lattice QCD*, *PoS* **LATTICE2019** (2019) 099 [1907.13454].

[88] M. Dalla Brida, T. Korzec, S. Sint and P. Vilaseca, *High precision renormalization of the flavour non-singlet Noether currents in lattice QCD with Wilson quarks*, *Eur. Phys. J.* **C79** (2019) 23 [1808.09236].

[89] S. Sint, *The chirally rotated Schrödinger functional with Wilson fermions and automatic O(a) improvement*, *Nucl. Phys.* **B847** (2011) 491 [1008.4857].

[90] P. Korcyl and G. S. Bali, *Nonperturbative determination of improvement coefficients using coordinate space correlators in $N_f = 2 + 1$ lattice QCD*, *Phys. Rev.* **D95** (2017) 014505 [1607.07090].

[91] G. S. Bali, K. G. Chetyrkin, P. Korcyl and J. Simeth, *Non-perturbative determination of quark mass-dependent improvement coefficients in $n_f = 2 + 1$ lattice QCD*, in preparation.

[92] O. Bär, *Nucleon-pion-state contribution to nucleon two-point correlation functions*, *Phys. Rev.* **D92** (2015) 074504 [1503.03649].

[93] B. C. Tiburzi, *Chiral corrections to nucleon two- and three-point correlation functions*, *Phys. Rev.* **D91** (2015) 094510 [1503.06329].

[94] B. C. Tiburzi, *Excited-state contamination in nucleon correlators from chiral perturbation theory*, *PoS* **CD15** (2016) 087 [1508.00163].

[95] O. Bär, *Chiral perturbation theory and nucleon-pion-state contaminations in lattice QCD*, *Int. J. Mod. Phys.* **A32** (2017) 1730011 [1705.02806].

[96] O. Bär, *Multi-hadron-state contamination in nucleon observables from chiral perturbation theory*, *EPJ Web Conf.* **175** (2018) 01007 [1708.00380].

[97] Y.-C. Jang, R. Gupta, B. Yoon and T. Bhattacharya, *Axial vector form factors from lattice QCD that satisfy the PCAC relation*, *Phys. Rev. Lett.* **124** (2020) 072002 [1905.06470].

[98] O. Bär, *$N\pi$-state contamination in lattice calculations of the nucleon axial form factors*, *Phys. Rev.* **D99** (2019) 054506 [1812.09191].

[99] O. Bär, *$N\pi$-state contamination in lattice calculations of the nucleon pseudoscalar form factor*, *Phys. Rev.* **D100** (2019) 054507 [1906.03652].

[100] O. Bär, *$N\pi$-excited state contamination in nucleon 3-point functions using ChPT*, *PoS* **LATTICE2019** (2020) 078 [1907.03284].

[101] O. Bär, *Nucleon-pion-state contamination in lattice calculations of the axial form factors of the nucleon*, *PoS* **LATTICE2018** (2019) 061 [1808.08738].

[102] H. B. Meyer, K. Ottnad and T. Schulz, *A new method for suppressing excited-state contaminations on the nucleon form factors*, *PoS* **LATTICE2018** (2019) 062 [1811.03360].

[103] M. T. Hansen and H. B. Meyer, *On the effect of excited states in lattice calculations of the nucleon axial charge*, *Nucl. Phys.* **B923** (2017) 558 [1610.03843].

[104] S. Scherer and M. R. Schindler, *A Primer for Chiral Perturbation Theory*, *Lect. Notes Phys.* **830** (2012) 1.

[105] J. A. Oller, M. Verbeni and J. Prades, *Meson-baryon effective chiral Lagrangians to $\mathcal{O}(q^3)$*, *JHEP* **09** (2006) 079 [hep-ph/0608204].

[106] P. Wein, P. C. Bruns, T. R. Hemmert and A. Schäfer, *Chiral extrapolation of nucleon wave function normalization constants*, *Eur. Phys. J.* **A47** (2011) 149 [1106.3440].

[107] Y. Nambu, *Axial vector current conservation in weak interactions*, *Phys. Rev. Lett.* **4** (1960) 380.

[108] S. L. Adler, *Consistency conditions on the strong interactions implied by a partially conserved axial-vector current. II*, *Phys. Rev.* **139** (1965) B1638.

[109] PNDME collaboration, Y.-C. Jang, R. Gupta, H.-W. Lin, B. Yoon and T. Bhattacharya, *Nucleon electromagnetic form factors in the continuum limit from* $(2+1+1)$*-flavor lattice QCD*, *Phys. Rev.* **D101** (2020) 014507 [1906.07217].

[110] Y. Nakamura and H. Stüben, *BQCD - Berlin quantum chromodynamics program*, *PoS* **Lattice 2010** (2011) 040 [1011.0199].

[111] RQCD collaboration, G. S. Bali, E. E. Scholz, J. Simeth and W. Söldner, *Lattice simulations with* $N_f = 2+1$ *improved Wilson fermions at a fixed strange quark mass*, *Phys. Rev.* **D94** (2016) 074501 [1606.09039].

[112] O. Bär, *$N\pi$-states and the projection method for the nucleon axial and pseudoscalar form factors*, *Phys. Rev.* **D101** (2020) 034515 [1912.05873].

[113] C. Alabiso and G. Schierholz, *Asymptotic behavior of form factors for two- and three-body bound states. II. Spin-$\frac{1}{2}$ constituents*, *Phys. Rev.* **D11** (1975) 1905.

[114] R. J. Hill and G. Paz, *Model-independent extraction of the proton charge radius from electron scattering*, *Phys. Rev.* **D82** (2010) 113005 [1008.4619].

[115] B. Bhattacharya, R. J. Hill and G. Paz, *Model-independent determination of the axial mass parameter in quasielastic neutrino-nucleon scattering*, *Phys. Rev.* **D84** (2011) 073006 [1108.0423].

[116] M. Gell-Mann, R. J. Oakes and B. Renner, *Behavior of Current Divergences under $SU_3 \times SU_3$*, *Phys. Rev.* **175** (1968) 2195.

[117] S. R. Beane and M. J. Savage, *Baryon axial charge in a finite volume*, *Phys. Rev.* **D70** (2004) 074029 [hep-ph/0404131].

[118] A. Ali Khan et al., *Axial coupling constant of the nucleon for two flavors of dynamical quarks in finite and infinite volume*, *Phys. Rev.* **D74** (2006) 094508 [hep-lat/0603028].

[119] Particle Data Group collaboration, M. Tanabashi et al., *Review of Particle Physics*, *Phys. Rev.* **D98** (2018) 030001.

[120] K. S. Kuzmin, V. V. Lyubushkin and V. A. Naumov, *Quasielastic axial-vector mass from experiments on neutrino-nucleus scattering*, *Eur. Phys. J.* **C54** (2008) 517 [0712.4384].

[121] N. J. Baker, A. M. Cnops, P. L. Connolly, S. A. Kahn, H. G. Kirk, M. J. Murtagh, R. B. Palmer, N. P. Samios and M. Tanaka, *Quasielastic neutrino scattering: A measurement of the weak nucleon axial-vector form factor*, *Phys. Rev.* **D23** (1981) 2499.

[122] K. L. Miller et al., *Study of the reaction $\nu_\mu d \to \mu^- pp_s$*, *Phys. Rev.* **D26** (1982) 537.

[123] T. Kitagaki et al., *High-energy quasielastic $\nu_\mu n \to \mu^- p$ scattering in deuterium*, *Phys. Rev.* **D28** (1983) 436.

[124] K2K collaboration, R. Gran et al., *Measurement of the quasielastic axial vector mass in neutrino interactions on oxygen*, *Phys. Rev.* **D74** (2006) 052002 [hep-ex/0603034].

[125] MINOS collaboration, P. Adamson et al., *Study of quasielastic scattering using charged-current ν_μ-iron interactions in the MINOS near detector*, *Phys. Rev.* **D91** (2015) 012005 [1410.8613].

[126] MiniBooNE collaboration, A. A. Aguilar-Arevalo et al., *First measurement of the muon neutrino charged current quasielastic double differential cross section*, *Phys. Rev.* **D81** (2010) 092005 [1002.2680].

[127] C. Juszczak, J. T. Sobczyk and J. Żmuda, *Extraction of the axial mass parameter from MiniBooNE neutrino quasielastic double differential cross-section data*, *Phys. Rev.* **C82** (2010) 045502 [1007.2195].

[128] E. Amaldi, M. Benevantano, B. Borgia, F. De Notaristefani, A. Frondaroli, P. Pistilli, I. Sestili and M. Severi, *Axial-vector form-factor of the nucleon from a coincidence experiment on electroproduction at threshold*, *Phys. Lett.* **41B** (1972) 216.

[129] P. Brauel et al., *π^+ electroproduction on hydrogen near threshold at four-momentum transfers of 0.2, 0.4 and 0.6* GeV^2, *Phys. Lett.* **45B** (1973) 389.

[130] A. Del Guerra, A. Giazotto, M. A. Giorgi, A. Stefanini, D. R. Botterill, D. W. Braben, D. Clarke and P. R. Norton, *Measurements of threshold π^+ electroproduction at low momentum transfer*, *Nucl. Phys.* **B99** (1975) 253.

[131] A. Del Guerra, A. Giazotto, M. A. Giorgi, A. Stefanini, D. R. Botterill, H. E. Montgomery, P. R. Norton and G. Matone, *Threshold π^+ electroproduction at high-momentum transfer: a determination of the nucleon axial vector form factor*, *Nucl. Phys.* **B107** (1976) 65.

[132] A. S. Esaulov, A. M. Pilipenko and Yu. I. Titov, *Longitudinal and transverse contributions to the threshold cross-section slope of single-pion electroproduction by a proton*, *Nucl. Phys.* **B136** (1978) 511.

[133] B. Bhattacharya, G. Paz and A. J. Tropiano, *Model-independent determination of the axial mass parameter in quasielastic antineutrino-nucleon scattering*, *Phys. Rev.* **D92** (2015) 113011 [1510.05652].

[134] MiniBooNE collaboration, A. A. Aguilar-Arevalo et al., *First measurement of the muon antineutrino double-differential charged-current quasielastic cross section*, *Phys. Rev.* **D88** (2013) 032001 [1301.7067].

[135] J. Nieves, I. Ruiz Simo and M. J. Vicente Vacas, *The nucleon axial mass and the MiniBooNE quasielastic neutrino-nucleus scattering problem*, *Phys. Lett.* **B707** (2012) 72 [1106.5374].

[136] J. Nieves, I. Ruiz Simo and M. J. Vicente Vacas, *Inclusive charged-current neutrino-nucleus reactions*, *Phys. Rev.* **C83** (2011) 045501 [1102.2777].

[137] R. A. Smith and E. J. Moniz, *Neutrino reactions on nuclear targets*, *Nucl. Phys.* **B43** (1972) 605 [Erratum: *Nucl. Phys.* **B101** (1975) 547].

[138] D. Bohm and D. Pines, *A Collective Description of Electron Interactions: 1. Magnetic Interactions*, *Phys. Rev.* **82** (1951) 625.

[139] D. Pines and D. Bohm, *A Collective Description of Electron Interactions: 2. Collective* vs *Individual Particle Aspects of the Interactions*, *Phys. Rev.* **85** (1952) 338.

[140] D. Bohm and D. Pines, *A Collective Description of Electron Interactions: 3. Coulomb Interactions in a Degenerate Electron Gas*, *Phys. Rev.* **92** (1953) 609.

[141] A. V. Butkevich and D. Perevalov, *Determination of the axial nucleon form factor from the MiniBooNE data*, *Phys. Rev.* **D89** (2014) 053014 [1311.3754].

[142] A. Bodek, H. S. Budd and M. E. Christy, *Neutrino quasielastic scattering on nuclear targets: Parametrizing transverse enhancement (meson exchange currents)*, *Eur. Phys. J.* **C71** (2011) 1726 [1106.0340].

[143] H.-Ch. Schröder et al., *The pion–nucleon scattering lengths from pionic hydrogen and deuterium*, *Eur. Phys. J.* **C21** (2001) 473.

[144] S. L. Adler and Y. Dothan, *Low-Energy Theorem for the Weak Axial-Vector Vertex*, *Phys. Rev.* **151** (1966) 1267 [Erratum: *Phys. Rev.* **164** (1967) 2062].

[145] L. Wolfenstein, *Weak interactions of pions and muons*, *Conf. Proc.* **C6909081** (1969) 661.

[146] R. Koch and E. Pietarinen, *Low-energy πN partial wave analysis*, *Nucl. Phys.* **A336** (1980) 331.

[147] R. A. M. Klomp, V. G. J. Stoks and J. J. de Swart, *Determination of the $NN\pi$ coupling constants in NN partial wave analyses*, *Phys. Rev.* **C44** (1991) R1258.

[148] V. Stoks, R. Timmermans and J. J. de Swart, *Pion-nucleon coupling constant*, *Phys. Rev.* **C47** (1993) 512 [nucl-th/9211007].

[149] J. J. de Swart, M. C. M. Rentmeester and R. G. E. Timmermans, *The status of the pion-nucleon coupling constant*, *PiN Newslett.* **13** (1997) 96 [nucl-th/9802084].

[150] R. A. Arndt, Z. Li, L. D. Roper and R. L. Workman, *Pion-nucleon coupling constant*, *Phys. Rev.* **D44** (1991) 289.

[151] R. A. Arndt, Z. Li, L. D. Roper, R. L. Workman and M. Ford, *Pion-nucleon partial-wave analysis to* 2 GeV, *Phys. Rev.* **D43** (1991) 2131.

[152] R. A. Arndt, R. L. Workman and M. M. Pavan, *Pion-nucleon partial-wave analysis with fixed-t dispersion relation constraints*, *Phys. Rev.* **C49** (1994) 2729.

[153] J. Rahm et al., *np scattering measurements at* 162 MeV *and the πNN coupling constant*, *Phys. Rev.* **C57** (1998) 1077.

[154] M. M. Pavan, R. A. Arndt, I. I. Strakovsky and R. L. Workman, *Determination of the πNN Coupling Constant in the VPI/GWU $\pi N \to \pi N$ Partial-Wave and Dispersion Relation Analysis*, *PiN Newslett.* **15** (1999) 171 [nucl-th/9910040], [*Phys. Scripta* **T87** (2000) 65].

[155] H.-Ch. Schröder et al., *Determination of the πN scattering lengths from pionic hydrogen*, *Phys. Lett.* **B469** (1999) 25.

[156] T. E. O. Ericson, B. Loiseau and A. W. Thomas, *Determination of the pion-nucleon coupling constant and scattering lengths*, *Phys. Rev.* **C66** (2002) 014005 [hep-ph/0009312].

[157] D. V. Bugg, *The pion nucleon coupling constant*, *Eur. Phys. J.* **C33** (2004) 505.

[158] R. A. Arndt, W. J. Briscoe, I. I. Strakovsky and R. L. Workman, *Extended partial-wave analysis of πN scattering data*, *Phys. Rev.* **C74** (2006) 045205 [nucl-th/0605082].

[159] V. Baru, C. Hanhart, M. Hoferichter, B. Kubis, A. Nogga and D. R. Phillips, *Precision calculation of the $\pi^- d$ scattering length and its impact on threshold πN scattering*, *Phys. Lett.* **B694** (2011) 473 [1003.4444].

[160] V. Baru, C. Hanhart, M. Hoferichter, B. Kubis, A. Nogga and D. R. Phillips, *Precision calculation of threshold $\pi^- d$ scattering, πN scattering lengths, and the GMO sum rule*, *Nucl. Phys.* **A872** (2011) 69 [1107.5509].

[161] M. Hoferichter, J. Ruiz de Elvira, B. Kubis and U.-G. Meißner, *Roy–Steiner-equation analysis of pion-nucleon scattering*, *Phys. Rept.* **625** (2016) 1 [1510.06039].

[162] R. Navarro Pérez, J. E. Amaro and E. Ruiz Arriola, *Precise determination of charge-dependent pion-nucleon-nucleon coupling constants*, *Phys. Rev.* **C95** (2017) 064001 [1606.00592].

[163] M. L. Goldberger and S. B. Treiman, *Form Factors in β Decay and μ Capture*, *Phys. Rev.* **111** (1958) 354.

[164] E. Matsinos, *A brief history of the pion-nucleon coupling constant*, 1901.01204.

[165] M. L. Goldberger, H. Miyazawa and R. Oehme, *Application of Dispersion Relations to Pion-Nucleon Scattering*, *Phys. Rev.* **99** (1955) 986.

[166] M. Hoferichter, B. Kubis and U.-G. Meißner, *Isospin breaking in the pion-nucleon scattering lengths*, *Phys. Lett.* **B678** (2009) 65 [0903.3890].

[167] M. Hoferichter, B. Kubis and U.-G. Meißner, *Isospin violation in low-energy pion-nucleon scattering revisited*, *Nucl. Phys.* **A833** (2010) 18 [0909.4390].

[168] C. Alexandrou, A. Athenodorou, M. Constantinou, K. Hadjiyiannakou, K. Jansen, G. Koutsou, K. Ottnad and M. Petschlies, *Neutron electric dipole moment using $N_f = 2 + 1 + 1$ twisted mass fermions*, *Phys. Rev.* **D93** (2016) 074503 [1510.05823].

[169] C. Alexandrou, K. Hadjiyiannakou, G. Koutsou, K. Ottnad and M. Petschlies, *Model-independent determination of the nucleon charge radius from lattice QCD*, *Phys. Rev.* **D101** (2020) 114504 [2002.06984].

[170] G. S. Bali, S. Collins and A. Schäfer, *Effective noise reduction techniques for disconnected loops in Lattice QCD*, *Comput. Phys. Commun.* **181** (2010) 1570 [0910.3970].

[171] RQCD collaboration, G. S. Bali, S. Collins, D. Richtmann, A. Schäfer, W. Söldner and A. Sternbeck, *Direct determinations of the nucleon and pion σ terms at nearly physical quark masses*, *Phys. Rev.* **D93** (2016) 094504 [1603.00827].

[172] X.-D. Ji, *Gauge-Invariant Decomposition of Nucleon Spin*, *Phys. Rev. Lett.* **78** (1997) 610 [hep-ph/9603249].

[173] Flavour Lattice Averaging Group collaboration, S. Aoki et al., *FLAG Review 2019*, *Eur. Phys. J.* **C80** (2020) 113 [1902.08191].